

BOSTON UNIVERSITY
COLLEGE OF ENGINEERING

Dissertation

**BIOMIMETIC NANOPORES FROM
ATOMICALLY THIN MEMBRANES**

by

LAUREN ELIZABETH YOUNG CANTLEY

B.A., Grinnell College, 2011
M.Sc., University of Colorado at Boulder, 2013

Submitted in partial fulfillment of the
requirements for the degree of
Doctor of Philosophy

2017

ProQuest Number:10271085

All rights reserved

INFORMATION TO ALL USERS

The quality of this reproduction is dependent upon the quality of the copy submitted.

In the unlikely event that the author did not send a complete manuscript and there are missing pages, these will be noted. Also, if material had to be removed, a note will indicate the deletion.



ProQuest 10271085

Published by ProQuest LLC (2017). Copyright of the Dissertation is held by the Author.

All rights reserved.

This work is protected against unauthorized copying under Title 17, United States Code
Microform Edition © ProQuest LLC.

ProQuest LLC.
789 East Eisenhower Parkway
P.O. Box 1346
Ann Arbor, MI 48106 – 1346

© 2017 by
Lauren Elizabeth Young Cantley
All rights reserved

Approved by

First Reader

Joseph Scott Bunch, Ph.D.
Assistant Professor of Mechanical Engineering
Assistant Professor of Materials Science and Engineering
Assistant Professor of Physics

Second Reader

Chuanhua Duan, Ph.D.
Assistant Professor of Mechanical Engineering
Assistant Professor of Materials Science and Engineering

Third Reader

Kenneth Rothschild, Ph.D.
Professor of Physics

Fourth Reader

Anna K. Swan, Ph.D.
Associate Professor of Electrical and Computer Engineering
Associate Professor of Materials Science and Engineering
Associate Professor of Physics

DEDICATION

This dissertation is dedicated to my family and friends.

ACKNOWLEDGMENTS

There are many people to thank for contributing to my success, as the work herein would not have been possible without them.

I would first like to thank my advisor, Scott Bunch, for exposing me to an exciting area of scientific research and guiding me to the completion of this thesis. He has helped me to become a better scientist; not only through words, but more importantly by example. His enthusiasm for science has been an inspiration and he has taught me the valuable lessons of perseverance when encountering failure, and using creativity to tackle difficult problems. I owe much of my success to his patient guidance over the course of the last six years.

Next, I would like to thank the entire Bunch lab, both past and present. I have learned much from past lab members Luda Wang, Xinghui Liu, and Steven Koenig, both through their theses and in person. I would also like to thank my current lab mates, David Lloyd and Kailu Song, for the useful discussions and enjoyable company while working together in the lab. David contributed a great deal to the work on MoS₂ in chapter 7, and Kailu was a valuable resource for discussing equivalent circuits and all things electrical. Additionally, I would like to acknowledge the undergraduate students who contributed to this project in various ways: Lauren Cosgriff (NNIN REU), Katlyn Conrad (NNIN REU), Isabella Haghighli (UROP), Ian Herd (UROP), and Emily Mesnick (UROP).

I would like to thank our collaborators at Lockheed Martin Space Systems Advanced Technology Center and at Oak Ridge National Laboratory whose contributions were essential to the completion of the work in chapter 5. Thanks to Steve Sinton for his

feedback and guidance throughout the project, Peter Bedworth and Scott Heisse for the growth and transfer of graphene, and Dave Cullen and Adam Rodinine for the perforation and imaging of nanopore devices. Lastly, a big thank you to Jacob Swett for his role in all aspects of the project, from discussions of experimental design, perforation and imaging of graphene nanopore devices, and being our main contact to the Lockheed Martin team. I would also like to acknowledge Kenji Wantanabe and Takashi Taniguchi for providing the h-BN utilized in chapter 5 of this work.

I would like to thank Chuanhua Duan, Kenneth Rothschild, Anna Swan, and Alice White for serving on my defense committee. Their comments and feedback have been very helpful in leading to the present document. I would also like to thank David Coker and Erik Lascaris for useful discussions and suggestions when teasing out the governing mechanism of this work.

I would like to thank the following funding organizations for financially supporting me throughout my graduate studies: National Science Foundation (NSF), grant no. 1054406 (CMMI: CAREER, Atomic Scale Defect Engineering in Graphene Membranes) and NSF, grant no. DGE-1247312 (Graduate Research Fellowship Program).

I would like to thank all the amazing friends I've met while at Boston University, and last but not least, I would like to thank my family, for their love and support throughout this journey. Inevitably, I am leaving someone deserving off this ever growing list, nonetheless, I am truly thankful to all that have contributed to my success.

BIOMIMETIC NANOPORES
FROM ATOMICALLY THIN MEMBRANES
LAUREN ELIZABETH YOUNG CANTLEY

Boston University College of Engineering, 2017

Major Professor: Joseph Scott Bunch, Assistant Professor of Mechanical Engineering, Assistant Professor of Materials Science and Engineering, Assistant Professor of Physics

ABSTRACT

Biological cells are filled with a variety of pores and channels that transport ions and molecules across the cell membrane. These passageways are vital to cell function and remarkably effective due to their high selectivity, high flux, and sensitivity to environmental stimuli. This level of control is extremely attractive for applications ranging from biotechnology to energy and the environment. In this thesis, the unique properties of two dimensional materials are utilized to create solid-state nanopores that closely mimic the function of biological ion channels.

Ionic conductance measurements were used to demonstrate that nanopores introduced into graphene membranes exhibit K^+/Na^+ selectivity and can modulate the ionic current with an applied gate voltage. These devices are shown to respond to low gate voltages (<500 mV) at biologically relevant concentrations (up to 1M). Cation-anion selectivity, concentration dependence, and pH dependence were also investigated. We propose the observed behavior is dependent on the presence of surface adsorbates that modify the surface energy of the membrane and near the pore, creating a gaseous barrier that is modulated via electro wetting. Additionally, we work toward creating light

responsive MoS₂ nanopores operating in solution, by monitoring the current through a MoS₂ nanopore while the device is exposed to a focused laser beam.

TABLE OF CONTENTS

DEDICATION	iv
ACKNOWLEDGMENTS	v
ABSTRACT	vii
TABLE OF CONTENTS	ix
LIST OF TABLES	xi
LIST OF FIGURES	xii
CHAPTER ONE: Introduction	1
CHAPTER TWO: Nanopores	7
2.1: Sensing	7
2.2: Separations	10
2.3: Perforation techniques	11
CHAPTER THREE: Two-dimensional materials	15
3.1: Graphene	16
3.2: Hexagonal boron nitride	21
3.3: Molybdenum disulfide	21
3.4: A short history of two-dimensional nanopores	25
3.5: AFM voltage pulse technique for creating graphene nanopores	32
CHAPTER FOUR: Theoretical aspects of ion transport	36

4.1: Electrostatic interactions.....	38
4.2: Electrically driven fluid transport.....	49
4.3: Hydrophobic interactions.....	55
CHAPTER FIVE: Voltage gated K^+/Na^+ selective nanopores from porous graphene.....	65
5.1: Device geometry and fabrication.....	65
5.2: Experimental design aspects.....	75
5.3: Graphene nanopore conductance: activated I-V characteristics, inter-cation selectivity and gate response.....	85
5.4: Cation-anion selectivity.....	93
5.5: Concentration and pH dependence.....	98
5.6: Understanding the mechanism for selectivity and gate response.....	102
5.7: Conclusions.....	108
CHAPTER SIX: Towards light responsive MoS_2 nanopores.....	109
6.1: Experimental design and preliminary results.....	109
6.2: Conclusions.....	114
CHAPTER SEVEN: Conclusions and future outlook.....	115
7.1: Summary.....	115
7.2: Future outlook.....	115
BIBLIOGRAPHY.....	117
CURRICULUM VITAE.....	132

LIST OF TABLES

Table 5.1: Catalog of the 14 porous graphene devices measured in this study. Pore size, perforation method and corresponding I-V behavior.....	74
Table 5.2: Measured bulk conductivities of electrolyte solutions used in this study.....	78

LIST OF FIGURES

- Figure 1.1** Illustration of protein ion channels spanning a lipid bilayer membrane. Ion channels function as selective pores, responding to specific environmental stimuli and allowing only the flow of specific ions. Taken from (Marban, 2002). 2
- Figure 1.2:** Two examples of solid-state control of ionic transport. (A) Schematic of a nanofluidic ion field effect transistor. (B) Differential ionic conductance of nanochannel transistors shown in (A) in 100 μM KCl solution and the fluorescence intensity of fluorescein-labeled 30mer single-stranded DNA molecules can both be modulated with an applied gate voltage. (C) Schematic of alumina coated nanopores with imbedded gate electrode. (D) Gate response of nanopore device in (C) in 100 μM KCl solution. Figures (A), (B) taken from (Karnik, et al., 2005) and (C), (D) from (Nam, et al., 2009). 4
- Figure 2.1:** Resistive pulse sensing technique. As a particle of diameter d approaches a pore of diameter D and length L , the current drops from its baseline value I_o (1) to a blockade value I_b (2), then returns to I_o once the particle has left the pore (3). The magnitude of the change in current, ΔI , is recorded along with the duration of the translocation event. Several hundred such events are collected in a typical scan of 10 seconds. Taken from (Davenport, et al., 2012). 9
- Figure 2.2:** Compilation of nanopores fabricated through various techniques. (A) TEM image of a nanopore in a silicon nitride membrane drilled with via focused electron beam in TEM (Smeets, et al., 2006). (B) TEM image of FIB sculpted nanopore in silicon nitride (Li, et al., 2001). (C) STEM image of an array of HIM drilled nanopores

in silicon nitride, scale bar 100 nm (Emmrich, et al., 2016). (D) Voltage-pulse pore in silicon nitride membrane. TEM image of entire silicon nitride membrane and (inset) pore (Yanagi, et al., 2014) (E) SEM image of track etched nanopores in silicon nitride membrane (Vlassiuk, et al., 2009). (F) Nanopores in monocrystalline silicon via rapid thermal annealing process. TEM image. (Streimer, et al., 2007). 14

Figure 3.1: Structure of graphene lattice. Carbon atoms are in blue. Taken from (Hedberg, n.d.). 17

Figure 3.2: Atomic structure of hexagonal boron nitride. Boron atoms are in green and nitrogen atoms are in red. Image taken from (Boldrin, et al., 2011). 20

Figure 3.3: Atomic structure of molybdenum disulfide. Adapted from (Wang, et al., 2012).. 24

Figure 3.4: (A) Side view illustration of a DNA translocation through a graphene nanopore. The baseline conductance of ionic current through the nanopore and the occurrence of blockade events upon the addition of DNA. The depth and duration of blockade events are unique to the DNA position (nonfolded, partially folded and fully folded). Taken from (Schneider, et al., 2010). (B) ALD alumina coated graphene nanopores are shown to be more robust and significantly reduced electrical noise compared to pure graphene. Taken from (Venkatesan, et al., 2012). (C) Schematic of graphene nanoribbon device, where both transmembrane ionic current and graphene nanoribbon (GNR) electrical current can be recorded. Simultaneous measurement of both currents demonstrate that both measurements are able to detect DNA translocation events. Taken from (Traversi, et al., 2013). 26

Figure 3.5: (a-d) Gas separation experiment carried out by Koenig et al. (a) A graphene sealed micro cavity is placed inside a pressure chamber and filled with H₂, (b) upon removal from the pressure chamber the membrane bulges upward. (c) a single sub-nm pore is introduced via UV/Ozone etching and H₂ leaks out of the micro cavity, however (d) air cannot leak back into the micro cavity because the pore is selective. (e) Leak rates out of graphene sealed micro cavity with selective pore. Figures (a-e) taken from (Koenig, et al., 2012). (f) Schematic of graphene sealed glass vial filled with water; porous graphene (red), Si wafer (blue), Aluminum seal (grey), Lid (black). Pores are introduced into the graphene membrane via O₂ plasma exposure and degree of perforation is measured as the ratio of graphene's D and G Raman peaks. Water is allowed to evaporate out of the graphene sealed vial and water loss is measured as a change in mass. (g) Water loss and ionic conductivity across the membrane plotted against degree of perforation (C1 and C2 are control devices). (h) Selectivity of porous graphene plotted against the degree of perforation; High selectivity results from very short O₂ plasma exposure times. Selectivity is measured as the ratio of water flux to ionic conductivity. Figures (f-h) taken from (Surwade, et al., 2015). (i) intrinsic defects and tears in CVD graphene transferred to a polymer support are sealed with ALD hafnium and interfacial polymerization. (j) Selective pores are then introduced via ion bombardment followed by chemical oxidation and are shown to separate ~1 nm molecules from monovalent ions. (i-j) taken from (O'Hern, et al., 2015). 29

Figure 3.6: (A) Photo of 1 μm thick graphene oxide film. (B) SEM image of graphene oxide film's cross section. (C) Schematic of water permeation mechanism through graphene oxide layers. Taken from (Nair, et al., 2012). 30

Figure 3.7: AFM pulse technique for introducing single pores. (a) AFM height image of suspended graphene membrane with large pore ($\sim 300\text{ nm}$) at its center. AFM height images of a pressurized graphene membrane (b) before and (c) ~ 3 minutes after etching a small pore ($\sim 1\text{ nm}$) at the center of the membrane. Adapted from (Wang, et al., 2015). 35

Figure 4.1: Schematic illustration of electric double layer (left) and electric potential profile normal to the negatively charged surface. Taken from (Daiguji, 2010). 41

Figure 4.2: Schematic illustration of the field effect control of the ionic distribution near a planer surface. Taken from (Hu, et al., 2012). 41

Figure 4.3: Schematic of effect of surface charge in micro and nano channels. (a, c, e) In a microchannel the Debye length is usually much smaller than the channel dimensions, thus the electrical potential quickly decays to the bulk value and the concentration of cations and anions within the pore is the bulk concentration. (b,d,f) In a nanochannel, the Debye length is the same order of magnitude as the channel dimensions, thus the EDL from either wall overlap. The electric potential and concentration of anions and cations at the center of the channel are affected by the charge at the surface and are not equal to bulk values. Taken from (Karnik, et al., 2005). 44

Figure 4.4: A plot of pore conductance against the bulk ionic concentration for nanopore devices from (Smeets, et al., 2006). Black symbols are experimental data points. Green curve represents a bulk conductance model (equation 4.1), Blue curve represents a conductance model incorporating a fixed surface charge while red curve represents a model with variable surface charge. Inset plots surface charge against bulk concentration. Figure taken from (Smeets, et al., 2006)..... 46

Figure 4.5: (a) Diagram of cross section of thin graphene nanopore. Path 1 (dashed line) depicts bulk transport mechanism while path 2 (solid line) depicts a surface transport mechanism. Color scale indicates the concentration of K^+ ions. (b) Concentrations and (c) current densities of K^+ (blue) and Cl^- (red) along each path illustrated in (a). Taken from (Rollings, et al., 2016)..... 48

Figure 4.6: Schematic of cylindrical pore in Cartesian coordinates, with the z axis along axis of the pore. The pore has length L and radius R . V_o and V_L are the external potentials and C_o and C_L are the concentrations at either end of the pore, respectively. 51

Figure 4.7: PNP model fit to non-linear I-V curves. Symbols represent experimentally measured I-V curves of transport through a graphene nanopore in 1M KCl (linear (a), rectified (b), and activated (c)) with fits from the transport model (lines). Model geometry for the graphene nanopore (d). Taken from (Jain, et al., 2015)..... 54

Figure 4.8: Illustration of the intermolecular forces acting on the molecules within the bulk and at the surface of a liquid. Molecules (represented here as circles) within the bulk of the liquid experience equal forces of attraction (arrows) in all directions, however

molecules at the surface experience unbalanced attractive forces. Adapted from (Shaw, 1980). 56

Figure 4.9: (A) Diagram of contact angle measurement at the three phase contact line. (B) Schematic illustration of electro-wetting phenomena on planer surface. When a voltage is applied, the surface between the water and substrate increases, decreasing the contact angle. 58

Figure 4.10: (A) Illustration of the critical distance D_C for stable vapor (left) and liquid (right) states to occupy the space between two hydrophobic planer surfaces.(B) A graphical representation of the spacing required for liquid and vapor states, plotting the fluid density, ρ_D , against the inter-surface separation, D . D_c and D_c^k denote the thermodynamic and kinetic threshold, respectively, for the spontaneous evaporation of a confined liquid, the area between the two thresholds signifies the space where a metastable liquid may exist. Image taken from (Luzar, 2004). 61

Figure 4.11: (a) Illustration of a cross section though a hydrophobic nanopore. Hydrophobic regions are shown in yellow, the membrane is shown in green. (b) Liquid-vapor oscillations occur within a hydrophobic nanopore. The stability of the wetted state depends on the pore diameter.(c) The stability of the wetted state also depends on the hydrophobicity of the atoms lining the pore walls.(d) The application of a transmembrane voltage can open the pore to a wetted state. Figure taken from (Aryal, et al., 2015). 64

Figure 5.1: (A) Schematic of measurement circuit and cross section of device. Graphene is suspended over a 5um hole in a silicon nitride window and mounted in a custom

microfluidic cell in which electrolyte solution is introduced to both sides of the graphene membrane. (B) Optical image of exfoliated graphene device, with graphene flake outlined. (C) HIM image of CVD graphene with nine 35 nm pores drilled using HIM, device CVD-6..... 66

Figure 5.2: (A) Optical image of exfoliated graphene flake on PMMA/PVP/silicon substrate. Inset is of graphene on silicon nitride substrate after transfer. Scale bars, 25 μm . (B) Raman spectra for the exfoliated flake in (A). Monolayer graphene is identified by the ratio of the G to 2D peaks (Ferrari, et al., 2006). (C) Schematic of the pick-and-place transfer of exfoliated graphene flake onto silicon nitride substrate, adapted from (Dean, et al., 2010). (D) Schematic of CVD transfer process. (1) copper substrate is etched away from graphene in APS, (2) copper etchant is exchanged with DI water solution, (3) SiN support chip is used to scoop up graphene from the surface of water bath, (4) sample is left to dry. Adapted from (Ondarcuhu, et al., 2013). 68

Figure 5.3: Composite STEM images (CVD-1 – CVD-4, CVD-10, HBN-1, HBN-2), HIM images (CVD-5 – CVD-9, CVD-11) and SEM images (EXF-1, CVD-12, CVD-13) of porous graphene and h-BN devices. Scale bar is 1 μm , unless otherwise noted. 72

Figure 5.4: Pore size and distribution for Xe^+ irradiated devices. (A) CVD-2, (B) CVD-3, and (C) CVD-10. Inset is a representative high magnification STEM image of select pores..... 73

Figure 5.5: Optical images of (A) top view and (B) side view of graphene on silicon support chip mounted in microfluidic cell. (C) schematic of microfluidic cell.

Microfluidic cell consists of microchannels patterned into PDMS block and plasma bonded to underlying glass slide (Underlying glass slide measures 1”x 3”). Graphene coated silicon nitride chip is adhered to the PDMS block using PDMS. 76

Figure 5.6: Pore conductance for device CVD-11 displaying cation selectivity at 0.1M Cl⁻ concentration. Electrolyte solutions were measured in the order listed in the legend. This order does not correlate with ion size or hydration energy and alternates back and forth between solutions. 76

Figure 5.7: Equivalent circuit diagram for graphene nanopore device mounted in the experimental set up. Due to asymmetries in the device and microfluidic cell, the solution resistance, leakage resistance and leakage capacitance are not necessarily the same on either side of the membrane, hence the subscripts 1 and 2..... 78

Figure 5.8: (A) Leakage current in device EXF-1 from gate to drain, with the source floating, for different concentrations of KCl. (B) I-V curves for device EXF-1 in 0.1M KCl with the gate swept from -500 mV to 500 mV under source voltages ranging from 0 mV to 300 mV. 80

Figure 5.9: Illustration of control devices and leakage pathways measured, corresponding to the five types of devices listed above. 83

Figure 5.10: I-V behavior from a singular abnormal control device. One type (5) control device exhibited (A) unstable pore conductance in 0.1 M KCl (arrow indicates increasing time) and (B) non-selective I-V behavior in electrolyte solutions at 0.1M Cl⁻ concentration. (C) Gating behavior in 0.1M KCl under gate voltages ranging from 0 mV to -500 mV. 84

Figure 5.11: I-V curves for (A) device EXF-1 and (B) device CVD-6. Gating behavior for (C) device EXF-1 and (D) device CVD-6. All solutions are at 0.1M Cl⁻ concentration. 86

Figure 5.12: Normalized conductance across porous graphene device EXF-1. Conductance taken at $V_s = 0$ mV. All solutions are at 0.1 M Cl⁻ concentration. 87

Figure 5.13: Selectivity ratio S_{Na} (orange), S_{Li} (purple), S_{Ca} (Cyan) and S_{Mg} (pink) for the 14 porous graphene devices measured in this study, ordered according to selectivity. The dotted line indicates a selectivity ratio of 0.5. Device CVD-1 and CVD-2 did not have appreciable conductance, thus a selectivity ratio was not measured. See table 5.1 for details on specific devices. 89

Figure 5.14: (A–C) Pore conductance for device CVD-10 in 0.1M KCl, 0.1M NaCl and 0.1M LiCl solutions, measured periodically over 19 days. (D–E) depict the pore conductance ($V_g = \text{float}$) for device CVD-10 in 0.1 M Cl⁻ concentration on (D) Day 19 and (E) after extended exposure to $V_g = -500$ mV in 0.1M NaCl on Day 67. Selective behavior remained while overall conductance and degree of selectivity increased. 90

Figure 5.15: Conductance (open circles) in 0.1 M KCl and corresponding sodium selectivity ratio (S_{Na}) for devices with HIM drilled pores. 92

Figure 5.16: (A) Schematic of reversal potential measurements. A concentration gradient and electric potential are simultaneously imposed across the nanopore and I-V behavior is measured. (B) The resulting I-V curves for several concentration gradients, indicated in the legend. 97

Figure 5.17: (A) Symmetric ion conditions for both KCl and CaCl₂ at 0.1 M Cl⁻ concentration. (B–C) Asymmetric ion conditions in 0.1 M Cl⁻ concentration, with (B) KCl on the source side of the membrane and (C) CaCl₂ on the source side of the membrane..... 97

Figure 5.18 (A) Pore conductance across device CVD-10 in KCl solutions of varying concentration. Measured on Day 19. Non-linear, activated I-V behavior remains across varying concentrations, however ‘activation voltage’ is lower as the concentration increases. (B) Measured pore conductance at $V_s = 0$ mV as a function of electrolyte concentration for device CVD-10. Measured on Day 85. Deionized water was measured to give the data points at 10^{-7} M..... 100

Figure 5.19: (A) I-V curves measured across graphene nanopore in 0.1M KCl solutions with varying pH. (B) Conductance plotted against pH conditions. The conductance is observed to monotonically increase with increasing pH, different than the pH dependence witnessed in MoS₂ nanopores displaying ionic Coulomb blockade (Feng, et al., 2016)... 101

Figure 5.20: Changes in conductance (solid circles) in response to UVO treatment for (A) device HBN-1, with an approximately 80 nm diameter pore, and (B) device HBN-2, with an approximately 30 nm diameter pore. Insets depict MAADF STEM images of respective pores prior to UVO treatment. Scale bars (A) 100 nm, (B) 20 nm. I-V curves for device HBN-2 at (C) $t = 4$ minutes and (D) $t = 13$ minutes. Selectivity ratios (solid triangles) in (B) are calculated from I-V curves in (C) and (D). Conductance is measured in 0.1M Cl⁻ solutions. 104

Figure 5.21: I-V curves in aqueous and ethanol based 0.1M LiCl solutions across graphene device containing nine approximately 25 nm pores drilled using the HIM. Measurements were carried out in the order shown in the legend, alternating between the two solutions... 107

Figure 6.1: (A) Bilayer MoS₂ flake transferred to silicon nitride substrate. The gate electrode is patterned in the same manner as for exfoliated graphene devices fabricated in chapter 5. Scale bar, 30 μm. (B) STEM image of 50 nm HIM drilled pore. (C) Optical image and (D) exploded view of microfluidic cell. The basic device is the same as that described in chapter 5. An additional O-ring and glass cover slip are added to contain the top reservoir of solution and eliminate the water meniscus which can interfere with laser path. (underlying glass slide measures 1" x 3").... 110

Figure 6.2: (A) Schematic of optical set up. (B) Changes in ionic current over time in response to ~1 μW laser exposure in 1 M KCl solution with a fixed bias voltage of 200 mV. Blue regions indicate when laser was on. When pore is exposed to laser illumination the current increases. When the laser is turned off the pore does not instantaneously return to its previous conductance state. (C) I-V curves for the MoS₂ device in 0.1M KCl solution after varying amounts of ~1 μW laser exposure. *indicates that device had laser exposure prior to t = 0 seconds, however powers were well below 1 μW..... 112

CHAPTER ONE: Introduction

Ion channels are membrane-spanning proteins that provide a pathway for small inorganic ions to cross the cell membrane (Hille, 2001) (figure 1.1). Ion channels play a vital role maintaining the normal physiological conditions of a living organism; from cell signaling, to volume regulation within single cells. They are remarkably effective due to their high selectivity, high permeability, and extreme sensitivity to a variety of external stimuli, such as a change in membrane potential, the binding of a neurotransmitter, or a mechanical deformation. For example, light-gated channelrhodopsin-2 contain a retinal chromophore covalently linked to the rest of the protein. Adsorption of light within the action spectrum induces a conformational change in the chromophore which in turn actuates the protein to open and allow flow of cations across the membrane (Nagel, et al., 2003). Voltage-gated potassium channels are known to respond to a change in membrane potential, opening to allow for selective transport of potassium over other similarly sized ions by a factor of over 1000 (MacKinnon, 2004).

Molecular separations, biosensors, therapeutics, ionic circuitry and energy conversion are just a few of the practical applications where this level of intelligent control is exceedingly desirable. However, challenges arise when working with ion channels outside their native physiological environment. Lipid bilayer membranes, the membrane in which the protein ion channel is embedded, are fragile and difficult to integrate into current fabrication technologies. Moreover, the entire biological system requires specific environmental conditions to function properly. This has motivated the development of solid-state devices that mimic the ion channel's functionality, both in liquid and gas phase

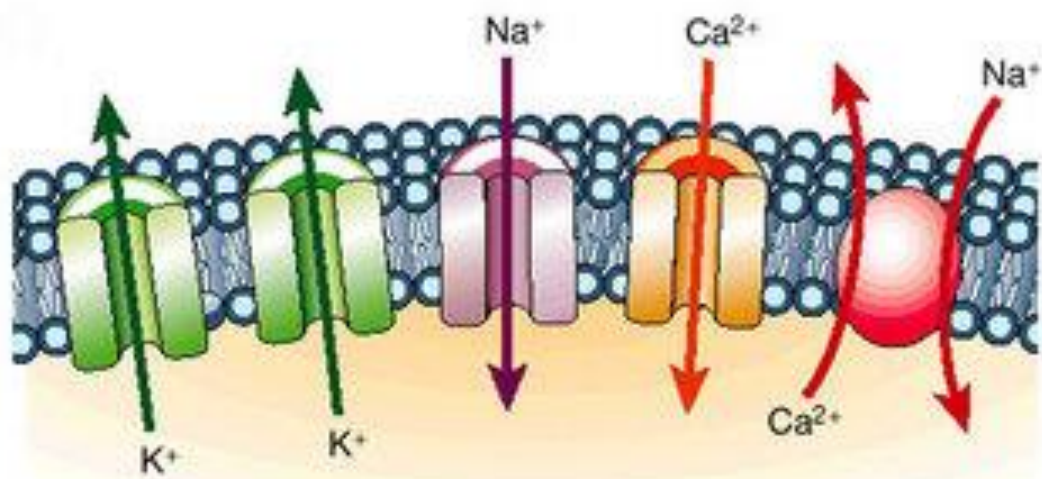


Figure 1.1 Illustration of protein ion channels spanning a lipid bilayer membrane. Ion channels function as selective pores, responding to specific environmental stimuli and allowing only the flow of specific ions. Taken from (Marban, 2002).

systems. Solid-state devices can provide the robustness and durability, as well as the thermal and mechanical stability, that biological ion channels lack. Additionally, solid state devices provide the ability to fabricate high density arrays and allow for integration with electrical and optical read out techniques (Xiao, et al., 2016).

Solid-state nanochannels and nanopores have previously been engineered to manipulate ionic transport (Guan, et al., 2014; Siwy & Howorka, 2010). Nanofluidic transistors based on metal-oxide-solution systems have demonstrated the ability to modulate the flux of both ions and molecules through the application of a gate voltage, similar to metal-oxide-semiconductor field-effect transistors (Karnik, et al., 2005). These devices, built from both silicon dioxide nanochannels and silica nanotubes, produce a 10-fold concentration enhancement when a 5 V source-drain bias and 50 V gate bias are applied (Karnik, et al., 2005). Surface functionalization of similar devices allows for ionic transistors to be tuned to either p-type or n-type field effect transistors, similar to doping in semiconductors (Fan, et al., 2005). Additionally, introducing a surface charge discontinuity can result in rectified, diode-like current behavior (Karnik, et al., 2007). More recently, work has been done to reduce the channel/pore dimensions, working towards gate-responsive functionality at biologically realistic ion concentrations (~0.1 M). Sub-10 nm channels in mesoporous silica films and sub-10 nm pores in alumina coated nanopores have both shown to modulate ionic current at concentrations up to 10^{-2} M (Fan, et al., 2008; Nam, et al., 2009). Ambipolar ionic field effect transistors (iFETs) have also been developed at the sub-10 nm scale (Lee, et al., 2015). Field effect modulated nanopore arrays (Joshi, et al., 2010), reconfigurable ionic diodes (Guan, et al., 2011), as well as iFET

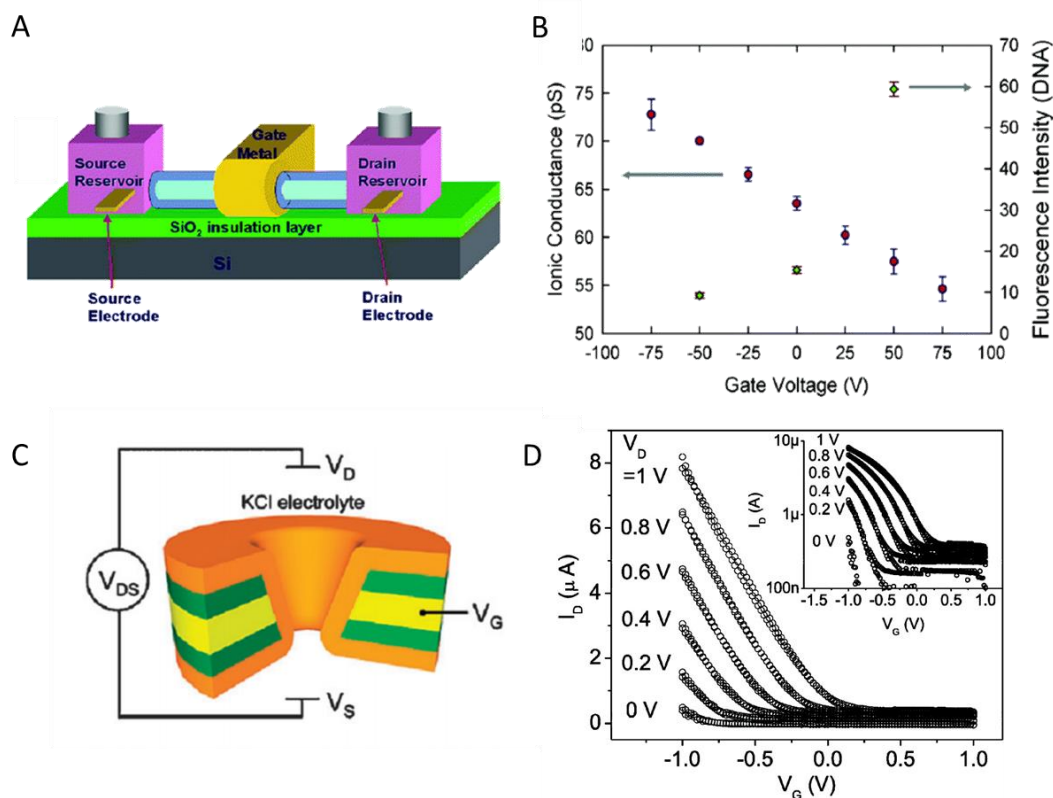


Figure 1.2: Two examples of solid-state control of ionic transport. (A) Schematic of a nanofluidic ion field effect transistor. (B) Differential ionic conductance of nanochannel transistors shown in (A) in 100 μM KCl solution and the fluorescence intensity of fluorescein-labeled 30mer single-stranded DNA molecules can both be modulated with an applied gate voltage. (C) Schematic of alumina coated nanopores with imbedded gate electrode. (D) Gate response of nanopore device in (C) in 100 μM KCl solution. Figures (A), (B) taken from (Karnik, et al., 2005) and (C), (D) from (Nam, et al., 2009).

devices for controlling molecular transport (Paik, et al., 2012; Karnik, et al., 2006) are just a few examples of the other silicon nanofluidic devices that have been developed. Apart from silicon based devices, conical gold nanotubes in PET polymer membranes have also demonstrated rectified current behavior due to excess surface charge (Siwy, 2006) and have been shown to respond to chemical stimuli, where the presence of calcium induces voltage-dependent ion current fluctuations (Siwy, et al., 2006).

While there has been much innovative progress towards developing functional solid-state ion channels, so far these devices have been limited by low electrolyte concentrations, high applied voltages, or a combination of the two (figure 1.2). Additionally, these devices are greatly limited in their ion selectivity. Thus, there is a clear and compelling need for next-generation materials that can combat the range of existing challenges in order to more closely mimic a protein ion channel's function. Two dimensional materials offer an exceptionally promising alternative. Their atomic thinness, mechanical stability, and the ability to control pore size and shape, offers the potential for both high flux and high selectivity, and increased sensitivity. Additionally, the range of optoelectronic properties offered by two dimensional materials suggests one could tune the pores to respond to a variety of environmental stimuli.

With biological ion channels as inspiration, this thesis experimentally investigates two dimensional materials for controlling ionic and molecular transport, focusing on voltage-gated K^+/Na^+ selective ion channels from porous graphene. Chapter 2 will provide an introduction to nanopores and nanopore fabrication techniques. Chapter 3 will introduce 2D materials properties and briefly review the background of 2D materials for nanopore

applications. Chapter 4 presents the prevailing theory of ionic and molecular transport through a solid-state nanopore, setting the stage for chapter 5, where ionic transport across porous graphene membranes in an aqueous environment is investigated. These devices are shown to demonstrate high inter-cation selectivity and are modulated with an applied gate voltage. Chapter 6 presents preliminary results of light responsive MoS₂ nanopores, and chapter 7 concludes with a summary and outlook for the future of this and related work.

CHAPTER TWO: Nanopores

This chapter will introduce nanopores, the prominent technologies driving their development, and the prevailing techniques used in their fabrication

2.1: Sensing

Resistive pulse sensing is the underlying technique in coulter counters, developed and commercialized in the 1950's for counting and sorting cells (DeBois & Bean, 1970). The technique has more recently had a resurgence for applications in single molecule detection due to recent advance in DNA technology and the development of fabrication techniques that can controllably introduce nanoscale pores into a material. Single molecule detection and DNA sequencing have been the driving application for developing nanopore sensing technologies. Utilizing the resistive pulse sensing technique, nanopores can provide a label free, amplification free, single molecule detection scheme that requires low reagent volumes and low cost (Venkatesan & Bashir, 2011).

Resistive pulse sensing is a technique based on measuring the ionic current flow through a pore (figure 2.1). The magnitude of the ionic current through the pore depends in part on the geometry of the pore. As a particle moves through the pore, it blocks a portion of the pore which would otherwise be carrying ionic current, resulting in a decreased ionic conductance (Miles, et al., 2013). This occurrence is called a blockade event. The magnitude of the blockade event is proportional to the translocating particle size. In this way, particles translocating through the pore can be counted and differentiated based on their blockade signature.

The first instance of DNA translocation with a nanopore device was carried out using a biological pore, α -haemolysin. This protein features a transmembrane channel only 1.4 nm in diameter at its narrowest point. The small constriction of this pore allowed for differentiation between different types of DNA as it was driven through the pore (Dekker, 2007). Since then, protein nanopores have been engineered to distinguish between individual base pairs within a strand of DNA (Clarke, et al., 2009). Already there is a commercial device on the market produced by Oxford Nanopore that utilizes this technology. Solid state devices are being developed as an alternative, with the promise of reducing fabrication costs and potentially providing increased control of pore dimensions and functionalization.

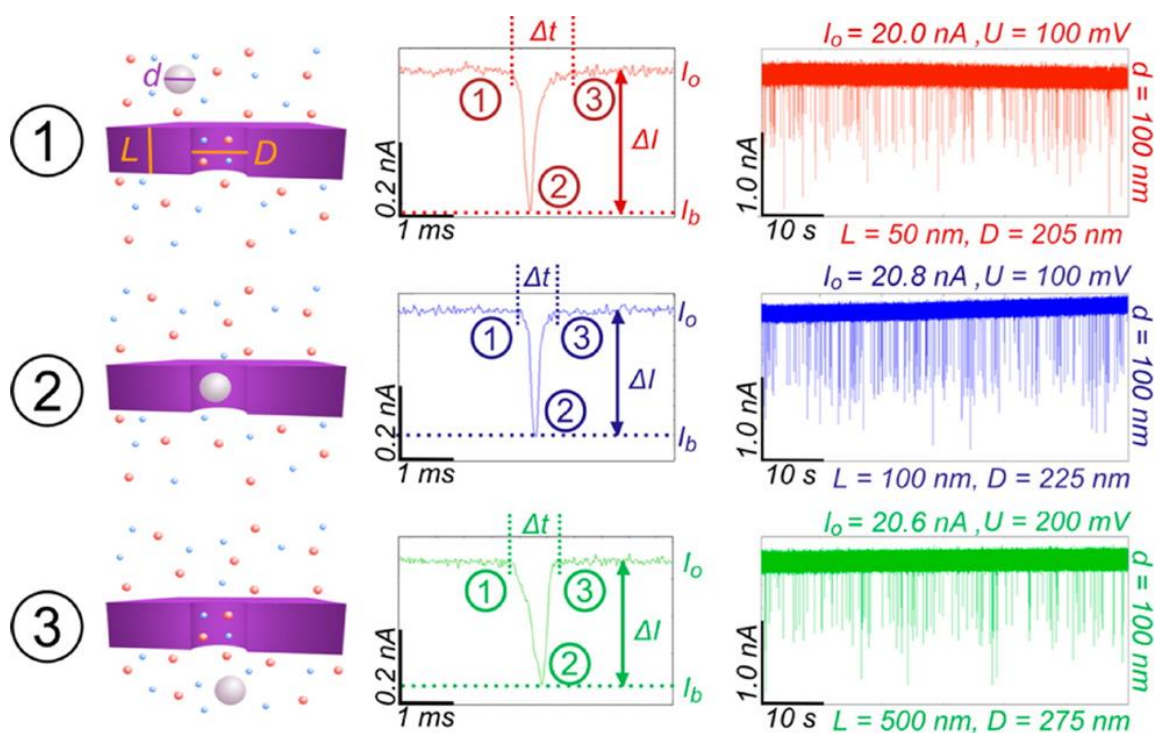


Figure 2.1: Resistive pulse sensing technique. As a particle of diameter d approaches a pore of diameter D and length L , the current drops from its baseline value I_o (1) to a blockade value I_b (2), then returns to I_o once the particle has left the pore (3). The magnitude of the change in current, ΔI , is recorded along with the duration of the translocation event. Several hundred such events are collected in a typical scan of 10 seconds. Taken from (Davenport, et al., 2012).

2.2: Separations

In addition to single nanopores for sequencing and single molecule detection, nanoporous membranes are being developed and utilized for filtration. Separation membranes are commonly classified by the size of their pores and/or the size of the particulate they intend to separate. Microfiltration commonly refers to the filtration of particles such as yeast, pollen or bacteria, where pore sizes range from ~500 nm up to 1 mm, whereas ultra and nanofiltration generally separate particles from 1nm up to 500 nm, such as proteins, endotoxins and viruses. Reverse osmosis (RO) membranes operate in the ~1nm range, purifying water by separating dissolved salts only a few angstroms in diameter.

Traditionally, ultra and nanofiltration membranes are made from polymeric materials or polymer composites with glass, metal or ceramic elements. These composite, or mixed matrix membranes, often have hollow fibers or zeolite crystals embedded into the polymer matrix to alter the transport of an intended species (Mahajan & Koros, 2002). However, these commercial ultra-filtration membranes often have broad pore size distributions, filtrate losses within the membrane, and low transport rates (Streimer, et al., 2007; Tong, et al., 2004; Kuiper, et al., 1998).

Consequently, thin solid state nanopore membranes are being developed to overcome these challenges. With a variety of large scale perforation techniques, ultrathin silicon base membranes as well as two dimensional materials can potentially increase the flux, efficiency and selectivity of ultrafiltration, nanofiltration and RO processes.

2.3: Perforation techniques

A variety of fabrication techniques have been developed and utilized to create single nanopores for sensing as well as arrays of nanopores for larger-scale separations. Silicon nitride has been a traditional material for nanopore fabrication, due to its relative chemical stability, low mechanical stress (Venkatesan & Bashir, 2011) and ease of integration with traditional microfabrication techniques.

A transmission electron microscope (TEM) technique to drill individual nanopores was developed by researchers at TU Delft and is now one of the most widespread methods by which to fabricate nanopores (Storm, et al., 2003). Free standing silicon nitride membranes are created using standard photolithography patterning and subsequent KOH etching, usually between 10–200 nm thick. A pore can then be introduced into the membrane with a localized focus electron beam in a TEM. Using the wide-field TEM illumination, material can be removed or deposited in order to fine tune the size and structure of the pore. A similar procedure, first developed at Harvard, utilizes a focused ion beam (FIB) to drill single nanopores and nanopore arrays (Li, et al., 2001). Starting with a suspended silicon nitride membrane, a focused ion beam is used to finely sculpt a nanometer sized pore. Feedback from ion detectors below the membrane indicate when to stop milling. Similar to TEM drilled devices, material can be removed or deposited depending on the ion rate and temperature. Generally, FIB instruments use a beam of gallium ions, however a helium ion microscope can also be used to mill nanopores in a similar fashion (Yang, et al., 2011; Emmrich, et al., 2016). These methods have been extended for use fabricating pores in two-dimensional materials as well. While these

methods allow for finely tuned nanopore diameters down to ~1 nm, the fabrication process is costly and fairly laborious given the need for expensive imaging equipment (TEM, FIB or HIM).

An alternative, low cost approach to introducing nanopores is through voltage-pulse techniques (Kwok, et al., 2014; Yanagi, et al., 2014). With this procedure, a membrane is mounted in a liquid cell separating two reservoirs containing an aqueous electrolyte solution. A voltage (~20 V) is applied across the membrane generating a high electric field, which leads to dielectric breakdown within the membrane. The leakage current across the membrane is monitored to determine the creation of a pore and its size. Once introduced the pore can also be enlarged by applying moderate AC electric field square pulses (Kwok, et al., 2014). This allows for sub-nm precision in sculpting pores ranging from 2 nm to 25 nm in diameter. This technique has also been utilized to create pores in two dimensional materials (Feng, et al., 2015; Kuan, et al., 2015).

So far, the perforation techniques discussed have been for fabricating individual pores. For separation applications, a large array of pores is often desired. While TEM and FIB drilling can be used to fabricate arrays of pores (Tong, et al., 2004), it is not the most efficient method. The track-etch technique can be used to form nanometer sized pores in a large area membranes, traditionally of a dense, glassy polymer. In this technique, a membrane is irradiated with heavy swift ions, which penetrate through the membrane leaving behind a trace of modified material confined to a cylinder several nanometers in diameter. A subsequent wet etch of the membrane material can be used to controllably enlarge the size of the existing ion-track pores without introducing damage to the rest of

the membrane material. Due to the fabrication method, these pores are generally conical in shape and usually range from 2 nm – 50 nm in diameter at the tip opening. In addition to polymeric membranes materials, this technique can also be used with silicon nitride membranes (Vlassiuk, et al., 2009), and a similar ion bombardment followed by chemical wet etch technique has been used on graphene as well (O'Hern, et al., 2014).

A technique to create porous nanocrystalline silicon membranes has been developed at the University of Rochester (Streimer, et al., 2007). With this technique, a thin amorphous silicon film (~ 15 nm thick) undergoes rapid annealing, wherein voids are formed spontaneously as nanocrystals nucleate and grow. These voids span the thickness of the membrane, creating nanometer sized pores. The pore size and density increase monotonically with the temperature of the anneal.

While not used in silicon nitride membranes, dry chemical etches, such as ultra violet/ozone irradiation and oxygen plasma, have been used to create pores in two dimensional materials. These process cause oxidation at defect sites within the two dimension lattice, expanding into pores. While this technique has been used to create single nanopores (Koenig, et al., 2012), increased exposure will expand existing pores in addition to introducing new pores, resulting in a wide pore size distribution.

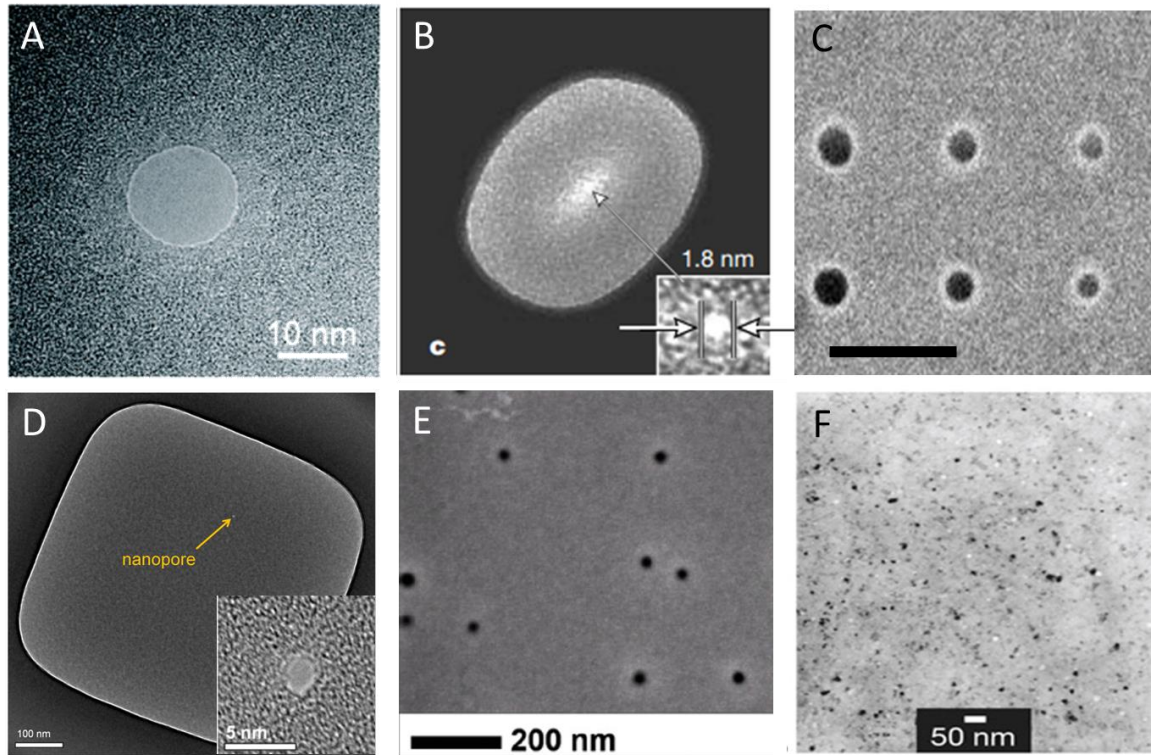


Figure 2.2: Compilation of nanopores fabricated through various techniques. (A) TEM image of a nanopore in a silicon nitride membrane drilled with via focused electron beam in TEM (Smeets, et al., 2006). (B) TEM image of FIB sculpted nanopore in silicon nitride (Li, et al., 2001). (C) STIM image of an array of HIM drilled nanopores in silicon nitride, scale bar 100 nm (Emmrich, et al., 2016). (D) Voltage-pulse pore in silicon nitride membrane. TEM image of entire silicon nitride membrane and (inset) pore (Yanagi, et al., 2014) (E) SEM image of track etched nanopores in silicon nitride membrane (Vlassiuk, et al., 2009). (F) Nanopores in nanocrystalline silicon via rapid thermal annealing process. TEM image. (Streimer, et al., 2007).

CHAPTER THREE: Two-dimensional materials

Dimensionality is a fundamental parameter of materials. The same chemical compound can have strikingly different properties depending on whether it is arranged in a 3D bulk crystalline structure or cleaved down to a 2D dimensional sheet (Novoselov, et al., 2005; Geim & Novoselov, 2007). Graphene has been the archetypal two dimensional nanostructure, known for its extraordinary properties (in terms of carrier mobility, flexibility, thermal conductivity and chemical resistivity) that are distinct from its three dimensional counterpart, graphite (Kostarelos, 2016; Park, 2016). Since graphene's first isolation, other two dimensional materials have also emerged. Some of these materials are monolayers comprising of a single element, such as phosphorene, while others feature different atoms alternating within the same layer, such as boron nitride and transition metal dichalcogenides (Anon., 2016; Novoselov, et al., 2016). Collectively, this family of two dimensional materials covers a wide range of materials properties. With this tool box of two dimensional materials, one can utilize each material's unique properties and combine them to create functionalities otherwise unattainable.

This chapter highlights the two dimensional materials utilized in this thesis: graphene, hexagonal boron nitride, and molybdenum disulfide, and discusses the unique properties that make them advantageous for nanopore applications. This is followed by a short review of the use of two dimensional materials in nanopore applications to date.

3.1: Graphene

Graphene is a single atomic layer of covalently bonded carbon atoms forming a flat hexagonal lattice (figure 3.1). When individual graphene sheets are stacked together, they form graphite. While strong sp^2 covalent bonds connect carbon atoms in-plane, weak van der Waals forces hold the individual graphene sheets together. This allows the sheets of graphene to slide with respect to each other, allowing graphite to be used as a writing tool. This phenomena led to graphene's first isolation in 2004.

Since its first isolation, graphene has been a rising star in science, continuing to excel when applied to new and novel engineering challenges. Much of graphene's success is due to its superior properties, which can be derived from its unique chemical structure. The initial surge of interest in graphene arose due to graphene's electronic properties. Most notably, graphene is a zero-band gap semiconductor, due in part to its two-dimensional nature. This unique band structure leads to graphene displaying interesting physics where the electrons behave as massless particles (Castro Neto, et al., 2009). One example of this is graphene's display of the integer quantum hall effect at room temperature (Nosovlov, et al., 2005; Zhang, et al., 2010). In addition to superior electronic properties, graphene is also nearly transparent, absorbing only 2.3% of light for a graphene monolayer (Bonaccorso, et al., 2010).

Mechanically, graphene is extremely strong. Only a single-layer of atoms thick, graphene has a Young's modulus for stretching as high as 1 TPa, and breaking strength of ~42 N/m with 25% strain (Frank, et al., 2007; Lee, et al., 2008). It was also found that graphene is impermeable to all standard gases at room temperature (Bunch, et al., 2008).

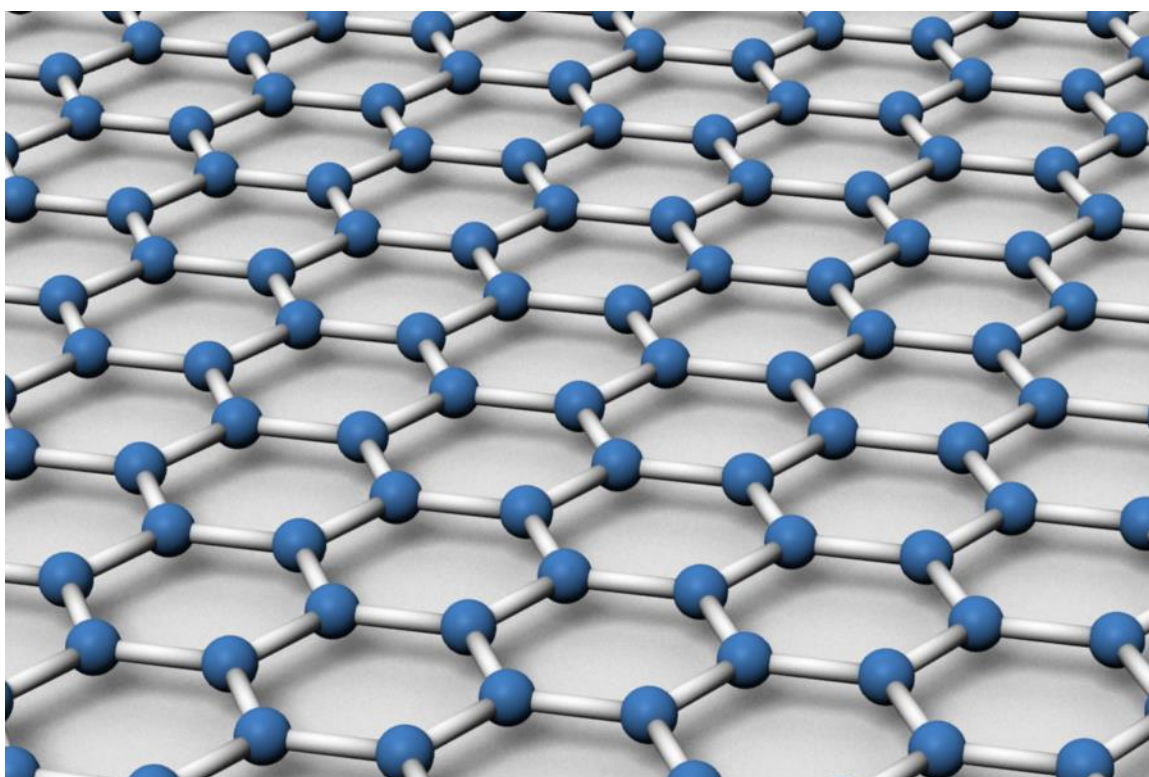


Figure 3.1: Structure of graphene lattice. Carbon atoms are in blue. Taken from (Hedberg, n.d.).

Theoretical studies attributed graphene's impermeability to its high crystal quality, low defect density and the electron density of graphene's aromatic rings being large enough to repel atoms and molecules trying to pass through (Jiang, et al., 2009). However, recently it was shown that graphene is not impermeable to proton transport, and also demonstrates selectivity between hydrogen isotopes (Hu, et al., 2014; Lozanda-Hidalgo, et al., 2016). Nevertheless, the introduction of pores and/or defects is necessary to observe transport of larger ionic species, atoms, and molecules.

The combination of superior strength, atomic thinness, and the ability to introduce controlled defects into an otherwise impermeable material gives graphene the potential to provide maximum flux with increased selectivity, surpassing even state of the art polymeric track-etched membranes. Consequently this has led to the investigation of porous graphene as a semi-permeable membrane material, which will be discussed further in section 3.4: A short history of two-dimensional nanopores.

In addition to mechanical strength and controlled pore formation, graphene's electrochemical stability in an aqueous electrolyte solution is essential for functioning as a gated nanopore in the liquid environment. Studies done to investigate graphene's potential as an electrode material for energy storage and conversion applications have found single layer graphene edge sites to be significantly more reactive than graphene's basal plane (Li, et al., 2011; Valota, et al., 2011; Yuan, et al., 2013). This has also been seen with studies carried out on carbon nanotubes; where the nanotube ends display the fastest electron transfer kinetics (Banks, et al., 2005). For edge sites on pristine graphene in an ionic solution, electrochemical current densities on the order of 10^4 A/cm² have been observed

in 1 M KCl solution (Banerjee, et al., 2013). However, carbon nanotubes coated with an amorphous carbon layer have been found to etch in 0.1M NaCl only at potentials more positive than 1.7 V, while bubbles were observed on the carbon nanotubes at potentials more negative than -0.5 V, indicating hydrogen evolution is likely the faradic process responsible at the negative potential limit (Ito, et al., 2003). No voltammetric peaks were observed in the range -0.5 V to 1.3 V.

Lastly, graphene's wettability is a point of interest. Graphite and other carbon materials historically have been accepted as hydrophobic, thus it was the common assumption that graphene was hydrophobic as well. However, recent studies have shown that graphene is intrinsically more hydrophilic than previously thought. Li et al. demonstrated that the water contact angle on freshly prepared supported graphene surfaces increased when exposed to ambient air. Airborne hydrocarbons were shown to adsorb onto graphitic surfaces within minutes of air exposure, increasing the water contact angle as much as 35 degrees in just 24 hours in ambient conditions (Li, et al., 2013; Kozbial, et al., 2014; Aria, et al., 2016). Theoretical work confirmed that absorption of only a monolayer of hydrocarbons is enough to reproduce the hydrophobic behavior previously observed on graphite (Kozbial, et al., 2014). Additionally, it has been shown both with simulations and experiment that one can tune the wettability and contact angle of water on graphene by doping the graphene sheet (Ashraf, et al., 2016; Ostrowski & Eaves, 2014).

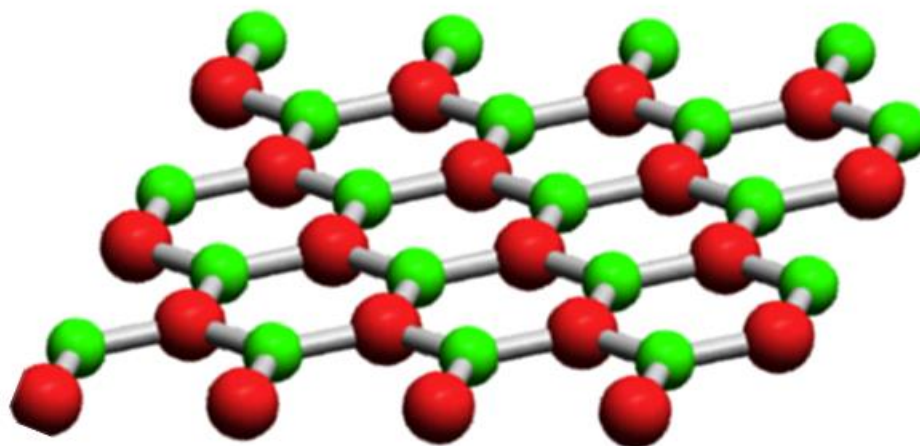


Figure 3.2: Atomic structure of hexagonal Boron Nitride. Boron atoms are in green and Nitrogen atoms are in red. Image taken from (Boldrin, et al., 2011).

3.2: Hexagonal boron nitride

Hexagonal boron nitride (h-BN), also known as ‘white graphene’, consists of hexagonal rings of alternating boron and nitrogen atoms held together by strong sp^2 covalent bonds and a lattice constant almost identical to that of graphene (Novoselov, et al., 2016) (figure 3.2). Due to the strong covalent bonds in-plane, h-BN displays high mechanical strength, thermal conductivity and chemical stability (Shi, et al., 2010; Song, et al., 2010; Lipp, et al., 1989; Ouyang, et al., 2010). With a large band gap of ~ 6 eV, h-BN is an ideal substrate for stacked 2D heterostructures, providing an atomically smooth insulating surface free of dangling bonds and charge traps (Novoselov, et al., 2016; Cassabois, et al., 2015).

h-BN’s strong oxidation resistance is attractive for nanopore applications, as surface treatments to increase hydrophilicity, such as UV/Ozone and oxygen plasma, do not damage the material (Chen, et al., 2004; Zhou, et al., 2013).

3.3: Molybdenum disulfide

Transition metal dichalcogenides (TMDC), with the formula MX_2 , have a hexagonal structure with each monolayer composed of three stacked layers (X-M-X) (Chhowalla, et al., 2013) (figure 3.3). They offer a range of electronic properties, from insulating to semi metallic, depending on the filling of the nonbonding d bands by the transition metal electrons (Novoselov, et al., 2016; Wang, et al., 2012). Of the TMDCs, molybdenum disulfide (MoS_2) has been widely studied as it is suitable for a wide range of electronic and optoelectronic applications (Subbaiah, et al., 2016).

MoS₂ has a layer dependent bandgap, crossing over from an indirect gap (1.2 eV) to a direct gap (1.8 eV) at the bulk to monolayer transition (Subbaiah, et al., 2016). This crossover can be understood by a combined effect of quantum confinement, long range Coulombic effect, and a change in hybridization between orbitals in p_z orbitals in S atoms and d orbitals in Mo atoms (Subbaiah, et al., 2016). The band structure of MoS₂ can also shift in response to strain in the material. Experiments have shown that the optical band gap reduces by ~ 50 meV/% for uniaxial strain (He, et al., 2013; Conley, et al., 2013) and ~ 100 meV/% for biaxial strain (Lloyd, et al., 2016).

The direct band gap in monolayer MoS₂ also makes it a promising material for optoelectronic applications. While the direct band gap in MoS₂ exists in the bulk structure, the photoluminescence does not exist in the bulk due to excitonic absorption. However in the monolayer regime the direct band gap dominates and direct band radiative recombination becomes the principle method for excitonic recombination (Ganatra & Zhang, 2014). Lopez-Sanchez et al. found the photoresponsivity of monolayer MoS₂ to be as high as 880 A/W at a wavelength of 561nm, with the photoresponse in the range of 400–680 nm (Lopez-Sanchez, et al., 2013).

Lastly, MoS₂ is also shown to have good mechanical strength. Its in-plane stiffness is ~ 180 N/m, corresponding to an effective Young's modulus of 270 GPa. Breaking occurs at a breaking strength of ~ 15 N/m with an effective strain between 6 – 11% when measured via nano-indentation experiments (Bertolazzi, et al., 2011; Jiang, 2015). Similar to graphene, MoS₂'s strength and atomic thinness makes it an attractive material for nanopore

applications. Its additional optoelectronic properties potentially offer alternative methods by which to control molecular transport that are not achievable with graphene.

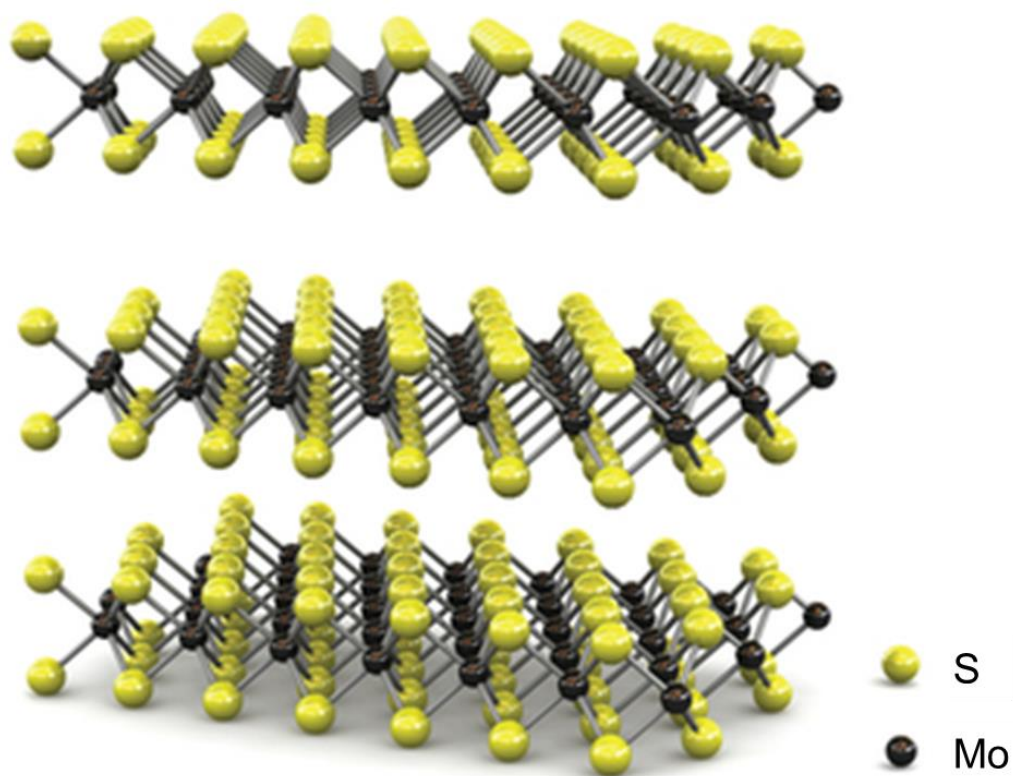


Figure 3.3: Atomic structure of molybdenum disulfide. Adapted from (Wang, et al., 2012).

3.4: A short history of two-dimensional nanopores

DNA sequencing has been one of the dominant applications driving graphene nanopore development. Graphene's thinness has been attractive for this application as it may offer the resolution necessary for single base pair detection using the resistive pulse sensing technique. With graphene's thickness on the order of angstroms, one could theoretically carry out DNA sequencing, characterizing each base pair as it translocates through the pore via the current blockade signature (Heerema & Dekker, 2016).

In 2010, several different research groups across the globe were able to demonstrate DNA translocation through a graphene nanopore. Single vs double stranded DNA, as well as folded vs single file DNA strands were differentiated (Garaj, et al., 2010; Merchant, et al., 2010; Schneider, et al., 2010). This proof of concept sparked much further research in the field. In subsequent years, efforts were focused on obtaining single-base-pair resolution. Working towards this goal, graphene nanopores were made with a reduced pore size to enhance the signal (Garaj, et al., 2012) and surface treatments were employed to tailor the graphene's hydrophobicity (Schneider, et al., 2013). Other sensing geometries were also explored, such as creating a stacked graphene-ALD-Alumina pore structure (Venkatesan, et al., 2012), and measuring the modulation of a transverse current across a graphene nanoribbon spanning the nanopore (Traversi, et al., 2013). Many efforts have been made towards developing DNA sequencing techniques that utilize graphene's unique properties, however challenges still remain in slowing DNA translocation speeds, lowering noise levels, and reducing conformational fluctuations of bases residing in the pore (Heerema & Dekker, 2016).

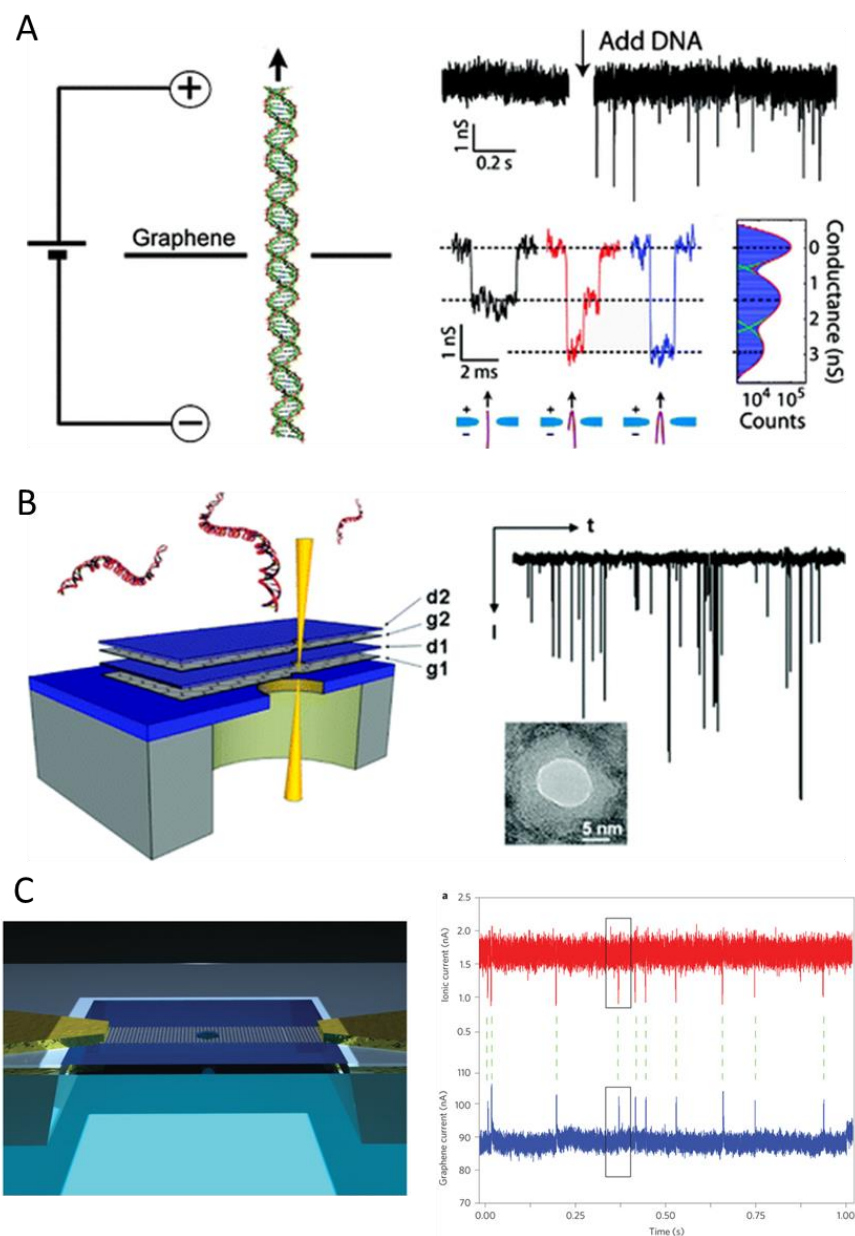


Figure 3.4: (A) Side view illustration of a DNA translocation through a graphene nanopore. The baseline conductance of ionic current through the nanopore and the occurrence of blockade events upon the addition of DNA. The depth and duration of blockade events are unique to the DNA position (nonfolded, partially folded and fully folded). Taken from (Schneider, et al., 2010). (B) ALD alumina coated graphene nanopores are shown to be more robust and significantly reduced electrical noise compared to pure graphene. Taken from (Venkatesan, et al., 2012). (C) Schematic of graphene nanoribbon device, where both transmembrane ionic current and graphene nanoribbon (GNR) electrical current can be recorded. Simultaneous measurement of both currents demonstrate that both measurements are able to detect DNA translocation events. Taken from (Traversi, et al., 2013).

In addition to DNA sequencing, 2D materials have also been attractive for gas separation and liquid filtration. When using a membrane to separate materials, the efficiency of the separation is restricted by how quickly a fluid can move through the membrane and how selective the membrane is. Graphene offers the combination of fast flow rates along with high selectivity, if pores can be controllably introduced into the material.

In 2008, Bunch et al. demonstrated that pristine exfoliated graphene is impermeable to all gases at room temperature (Bunch, et al., 2008). With this atomically thin barrier, one can imagine the potential for graphene to perform as a highly efficient gas separation membrane with the controlled introduction of pores. In 2009, Jiang et al. demonstrated just that using MD simulations. Graphene membranes were shown to have superior selectivity and permeability compared to traditional polymer and silica membranes (Jiang, et al., 2009). This high permeability and selectivity of porous graphene membranes was then demonstrated experimentally in 2012 by Koenig et al. By introducing angstrom-sized defects into a monolayer graphene membrane they were able to separate hydrogen from methane (Koenig, et al., 2012). Since these initial gas separation studies on micron-sized graphene membranes, work has been done to study how graphene membranes would function on a larger scale. Celebi et al. have demonstrated that mm-sized membranes with controlled pore sizes also display highly efficient mass transfer (Celebi, et al., 2014).

Along with gas separation, graphene membranes for liquid filtration have also been studied extensively within recent years. While graphene may be useful for a variety of liquid separation applications, desalination has driven much of the work on graphene

membranes operating in solution. MD simulations have demonstrated graphene to be superior to current state of the art reverse osmosis membranes by providing rapid water transport and high salt rejection (Cohen-Tanugi & Grossman, 2012). Experimental work done by Surwade et al. confirmed these computational studies by demonstrating that pores introduced via O₂ plasma etching can produce comparable water fluxes (Surwade, et al., 2015). Additionally, O'Hern et al. has demonstrated nanofiltration of nm sized particles with pores introduced into graphene via ion bombardment and subsequent oxidative etching (O'Hern, et al., 2014). Experimental studies have typically focused on CVD graphene, where challenges can arise from intrinsic defects in the grown film. Thus, O'Hern et al. have also put efforts towards sealing the intrinsic defects in graphene before introducing selective pores (O'Hern, et al., 2015).

Other 2D materials are now being explored for nanopore applications as well. Due to h-BN's oxidation resistance, h-BN nanopores can be exposed to treatments to increase wettability without damaging the pore (Zhou, et al., 2013). MoS₂ nanopores have also been shown to be a promising material for DNA sequencing due to their stability for extended time periods without the need for additional functionalization and their increased sensitivity through controlled pore formation (Feng, et al., 2015; Feng, et al., 2015; Farimani, et al., 2014; Liu, et al., 2014). In 2015, MoS₂ nanopores were shown to have single nucleotide resolution when DNA transport through the pore was slowed using an ionic liquid as the solvent (Feng, et al., 2015). Additionally, MoS₂ nanopores were recently shown to exhibit ion selectivity in a demonstration as nanopower generators (Feng, et al., 2016).

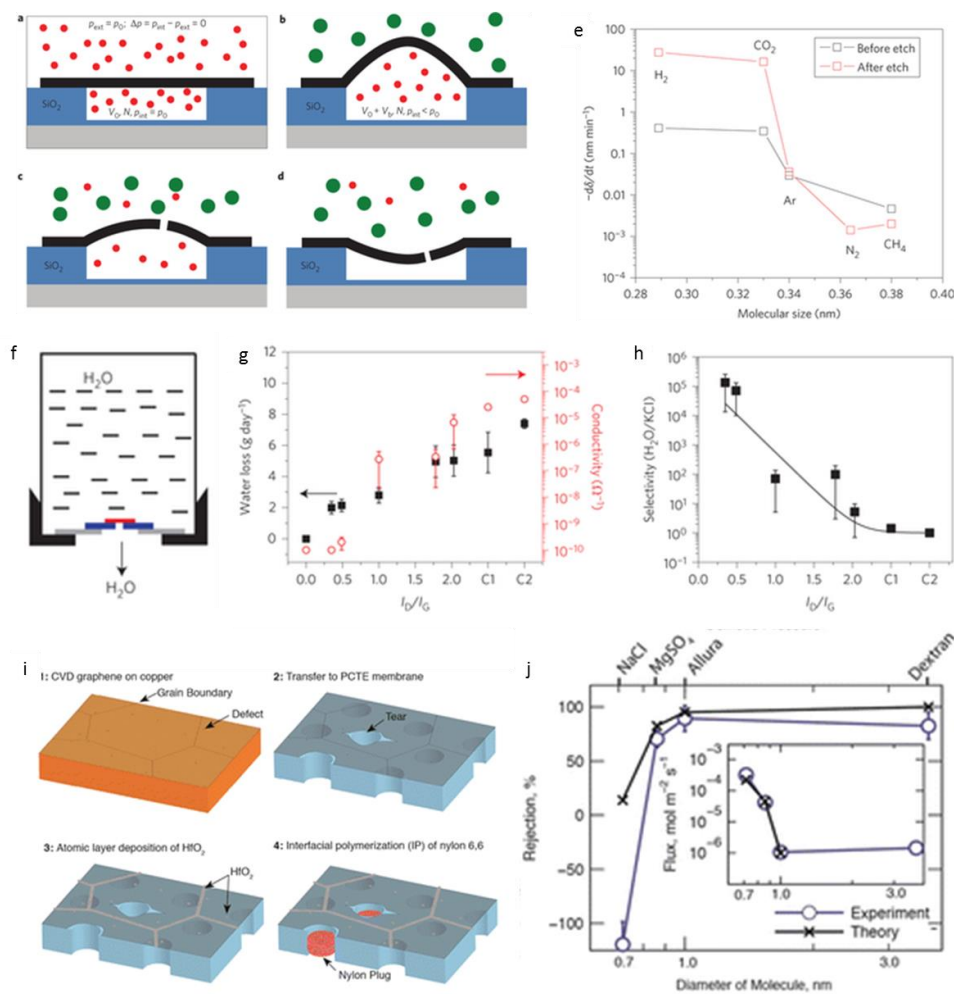


Figure 3.5: (a-d) Gas separation experiment carried out by Koenig et al. (a) A graphene sealed micro cavity is placed inside a pressure chamber and filled with H_2 , (b) upon removal from the pressure chamber the membrane bulges upward. (c) a single sub-nm pore is introduced via UV/Ozone etching and H_2 leaks out of the micro cavity, however (d) air cannot leak back into the micro cavity because the pore is selective. (e) Leak rates out of graphene sealed micro cavity with selective pore. Figures (a-e) taken from (Koenig, et al., 2012). (f) Schematic of graphene sealed glass vial filled with water; porous graphene (red), Si wafer (blue), Aluminum seal (grey), Lid (black). Pores are introduced into the graphene membrane via O_2 plasma exposure and degree of perforation is measured as the ratio of graphene's D and G Raman peaks. Water is allowed to evaporate out of the graphene sealed vial and water loss is measured as a change in mass. (g) Water loss and ionic conductivity across the membrane plotted against degree of perforation (C1 and C2 are control devices). (h) Selectivity of porous graphene plotted against the degree of perforation; High selectivity results from very short O_2 plasma exposure times. Selectivity is measured as the ratio of water flux to ionic conductivity. Figures (f-h) taken from (Surwade, et al., 2015). (i) intrinsic defects and tears in CVD graphene transferred to a polymer support are sealed with ALD hafnium and interfacial polymerization. (j) Selective pores are then introduced via ion bombardment followed by chemical oxidation and are shown to separate ~ 1 nm molecules from monovalent ions. (i-j) taken from (O'Hern, et al., 2015).

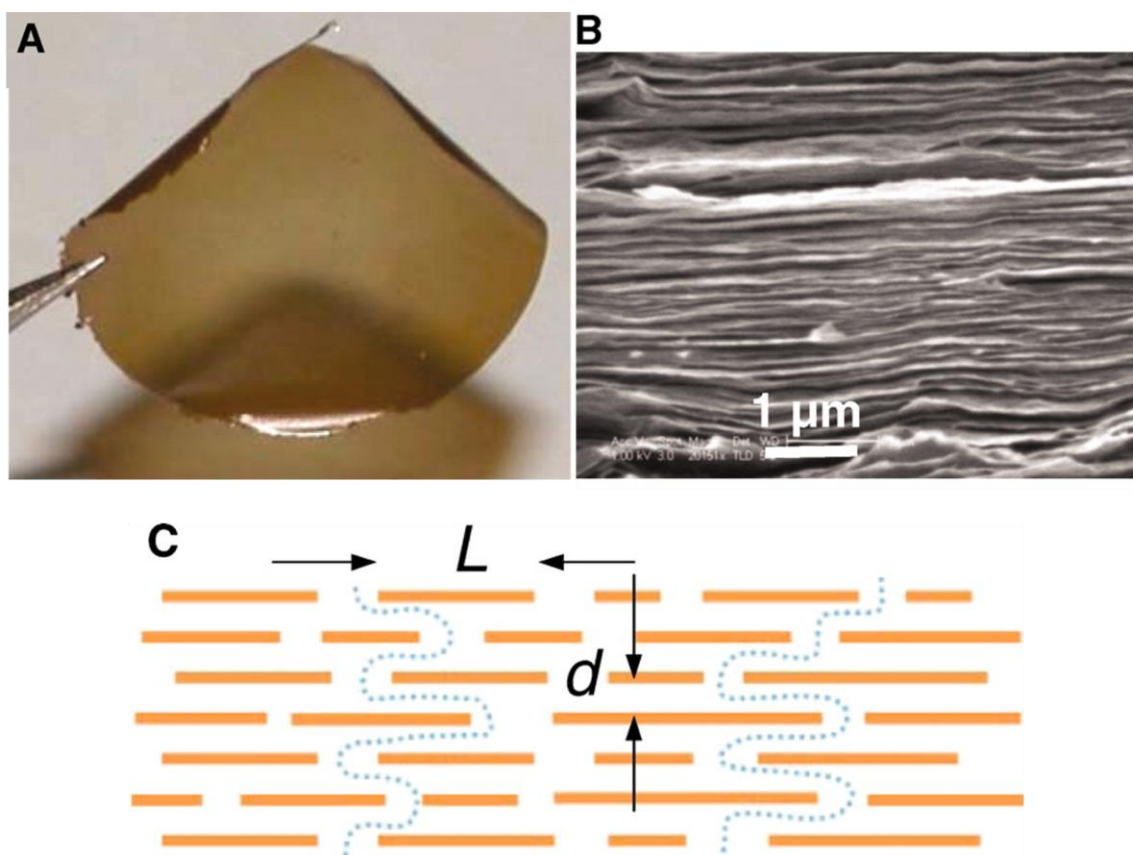


Figure 3.6: (A) Photo of 1 μm thick graphene oxide film. (B) SEM image of graphene oxide film's cross section. (C) Schematic of water permeation mechanism through graphene oxide layers. Taken from (Nair, et al., 2012).

While not strictly a 2D material, graphene oxide, the oxidized derivative of pristine graphene, has also been explored for separation applications. In 2012, Nair et al. demonstrated graphene oxide's ability for unimpeded water permeation while still maintaining a leak tight barrier to other liquids, vapors and gases, including helium. This behavior is attributed to the low-friction flow of water through nanoscale capillaries between the graphene oxide layers, while blocking the permeation of other molecules by clogging the narrow channels with water (Nair, et al., 2012) (figure 3.6). Since this early study, work has focused on tailoring the interlayer spacing of graphene oxide for selective separation of ions (Hong, et al., 2016; Cheng, et al., 2016).

With the interest in creating ion selective nanopores, research has proceeded to investigate smaller and smaller nanopore geometries, utilizing graphene and other two-dimensional materials to explore nanopores with diameters on the order of the translocating ions (<2 nm) and with atomic-sized channel lengths (0.34 nm thick graphene).

Since 2008, computational studies have explored the selectivity and transport physics of water and ions translocating through nm and sub-nm pores in 2D materials (Suk & Aluru, 2010; Suk & Aluru, 2014; Sint, et al., 2008; Hu, et al., 2012; Ying-Hua, et al., 2015). Molecular dynamics simulations by Sint et al. demonstrated graphene's ability for selective ion transport based on the pore functionality (Sint, et al., 2008). Computational and theoretical work done by Suk & Aluru have proposed how to augment current nanopore theory to account for the behavior of graphene nanopores acting in the semi-continuum and sub-continuum regimes (Suk & Aluru, 2014).

Experimental work done by Jain et al. proposed a transport model that accounts for dehydration effects in addition to pore charge and pore geometry, which would explain their observed non-linear, activated and rectified I-V behavior across sub-nm pores in graphene (Jain, et al., 2015). Experimental work on MoS₂ nanopores done by Feng et al. has proposed an ionic coulomb-blockade mechanism, similar to that of a quantum dot, to account for non-linear, activated I-V behavior observed in their devices (Feng, et al., 2016). Additionally, recent studies by Rollings et al. have proposed an alternate mechanism for selective ion transport, where surface conduction plays a dominate role as opposed to steric exclusion (Rollings, et al., 2016).

If nothing else, the above review demonstrates that ionic transport across nanoporous two-dimensional materials is of increasing interest to the scientific community, with much still to be learned about the diversity of fundamental transport mechanisms taking place, and much still to be developed before two dimensional nanopore devices appear in daily technologies.

3.5: AFM voltage pulse technique for creating graphene nanopores

The experiments reviewed in section 3.4 have generally utilized the perforation methods originally developed for silicon nitride membranes, discussed in section 2.3. Here, we have developed an alternative voltage pulse technique for introducing nanometer sized pores into thin two dimensional membranes while in air (Wang, et al., 2015). This method is advantageous for creating gas separation membranes. With this method suspended graphene membranes are fabricated and pressurized closely following the protocol described in references (Bunch, et al., 2008; Koenig, et al., 2012; Koenig, et al., 2011;

Wang, et al., 2012). Suspended monolayer graphene devices were fabricated via mechanical exfoliation onto predefined wells in a silicon dioxide (SiO_2) substrate, forming a graphene-sealed micro chamber that contains a μm^3 volume of gas inside the micro cavity. To pressurize the inside of the graphene-sealed micro-cavity, the sample was placed inside a high pressure chamber and gas was introduced to the chamber at a prescribed pressure. Because graphene is impermeable, gas diffuses into the graphene-sealed micro-cavity through the surrounding SiO_2 substrate.

While the membrane is still bulged upward, a pore is introduced into the membrane by applying a voltage pulse to the surface of the graphene membrane using a metallized AFM tip (Park, et al., 2002; Puddy, et al., 2011). This is carried out in the force-curve mode of the AFM (Asylum MFP-3D), where the location, duration and applied force of the AFM tip can be controlled. Figure 6.3a shows a ~ 300 nm diameter pore in the center of a suspended graphene membrane created by applying a voltage pulse of -5V for 100 ms. We found that the voltage and time needed to introduce a pore varied depending on the AFM tip used and the cleanliness of the tip, thus the difference in pore size between figure 6.3a and figure 6.3c. Consequently, to ensure a sub-nm sized pore, the voltage and duration of the pulse was iteratively increased until a single sub-nm pore was formed in the membrane. Immediately after pore formation, the deflection of the membrane drops and the graphene is flat aside from a few wrinkles introduced by the process. In this way we could tell when a pore was formed. Figure 6.3b shows a bulged membrane prior to pore formation and figure 6.3c depicts the same membrane, deflated, resulting from the introduction of a pore using a voltage pulse of -9V for 2 seconds. We could not detect the pore from the AFM

image post perforation, indicating that the pore is smaller than the resolution of the AFM. The pore size can be measured by monitoring and comparing the leak rate of different sized gas molecules (Koenig, et al., 2012).

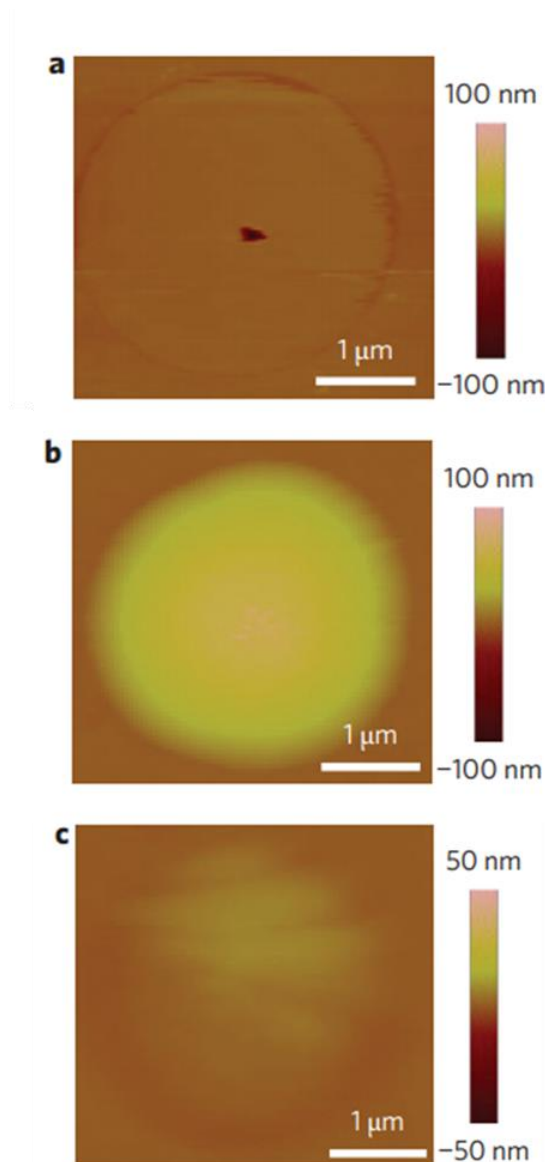


Figure 3.7: AFM pulse technique for introducing single pores. (a) AFM height image of suspended graphene membrane with large pore (~ 300 nm) at its center. AFM height images of a pressurized graphene membrane (b) before and (c) ~ 3 minutes after etching a small pore (~ 1 nm) at the center of the membrane. Adapted from (Wang, et al., 2015).

CHAPTER FOUR: Theoretical aspects of ion transport

Understanding the transport properties of nanopores is useful for the development of biomimetic solid-state devices. As suggested in chapter 3, the fundamental fluid physics witnessed at the nanoscale can vary drastically from its macroscale counterpart. However, nanopores offer the unique opportunity to investigate ionic and molecular transport on such a small scale. In this chapter, several concepts regarding fluid transport through a nanopore will be introduced, which will prove useful in understanding the studies carried out in chapters 5 and 6.

Let us begin with a simple model for the resistance of a cylindrical nanopore filled with an ionic solution. In this scenario, the resistance through the nanopore is modeled as the series combination of the resistance from the geometry of the pore itself, R_p , and the access resistance R_a (Davenport, et al., 2012). Since we are modeling the pore as a cylinder, the pore resistance can be written as

$$R_p = \frac{4l}{\pi\sigma d^2} \quad (4.1)$$

Where l is the length of the pore, d is the pore diameter and σ is the bulk conductivity of the ionic solution. The access resistance is a consequence of ions converging onto as small aperture from a semi-infinite reservoir. The model by Hall derives this resistance as the resistance between a flat disk electrode, representing the pore, and a hemispherical electrode far away (Hall, 1975). In this derivation, Hall exploits the relation between the resistance between two electrodes in conducting media and the capacitance between these electrodes in insulating media:

$$R = \frac{\epsilon_r \epsilon_o}{\sigma C} \quad (4.2)$$

where ϵ_r is the relative permittivity of the medium where the capacitance is measured, ϵ_o is the permittivity of free space, and C is the capacitance. The capacitance between a conducting disk and a hemispherical electrode far away can be written as $C = 4\epsilon_r \epsilon_o d$. The capacitance of a conducting disk on one side is only half this total capacitance, thus the access resistance of one side of the pore is

$$R = \frac{\epsilon_r \epsilon_o}{\sigma C} = \frac{\epsilon_r \epsilon_o}{2\sigma \epsilon_r \epsilon_o d} = \frac{1}{2\sigma d} \quad (4.3)$$

Since convergence effects take place at both the entrance and exit of the pore, the total access resistance is twice as large:

$$R_a = \frac{1}{\sigma d} \quad (4.4)$$

Taking both the access and pore resistance together, the total resistance can be written as

$$R = R_p + R_a = \frac{4l + \pi d}{\pi \sigma d^2} \quad (4.5)$$

More commonly, this is written as a pore conductance (Smeets, et al., 2006; Kowalczyk, et al., 2011; Davenport, et al., 2012)

$$G = \sigma \left[\frac{4l}{\pi d^2} + \frac{1}{d} \right]^{-1} \quad (4.6)$$

For large nanopores, often one can neglect the access resistance because the length of the pore is much greater than the pore's diameter. However, for low aspect ratio pores, where $d \gg l$, the access resistance dominates the nanopore conductance. Thus, for an

atomically thin graphene membrane, the above expression can be simplified to (Garaj, et al., 2010; Tsutsui, et al., 2012):

$$G = \sigma d \quad (4.7)$$

This simplified model is appropriate for estimating the conductance through a pore. However, this model assumes a fully wetted, cylindrical pore, which may not always be the case. It does not account for charge on the pore or membrane surface, nor does it consider other interactions that may take place at the pore mouth, such as dehydration. These considerations will be discussed in the following sections. Divided into three parts, the discussion will address electrostatic interactions of a charged nanopore, electrically driven fluid transport, and hydrophobic nanopores. In presenting these concepts, several mechanisms for ion selective transport will be discussed, including steric exclusion, surface charge, and hydrophobic gating, as well as mechanisms for gate responsive behavior, including direct electrostatic gating and electro-wetting phenomena.

4.1: Electrostatic interactions

To begin our discussion of charged nanopores, we will first examine a charged planar surface in solution to see how the surface charge influence both the electric potential as well as the ionic concentrations near the surface. Solids in solution bear a surface charge due to the dissociation of surface groups or the absorption of ionic species from the liquid (Hunter, 1989). Due to that surface charge, counter ions from the solution accumulate near the surface under the influence of electrostatic attraction. The screening layer created by the attracted counter ions is called the electric double layer (EDL). Some of the counter ions in the EDL are bound to the charged surface, in what is called the Stern layer, while

others remain mobile, in what is called the Debye layer (figure 4.1). At equilibrium, the electric potential governing the EDL is given by the Poisson equation:

$$\nabla^2 \phi = -\frac{\rho}{\varepsilon_r \varepsilon_0} \quad (4.8)$$

where ϕ is the electric potential, ρ is the charge density, ε_r is the relative permittivity of water, and ε_0 is the permittivity of free space. For ions in solution, the charge density can be represented as a summation of the ion concentration multiplied by the charge on each ion, $\rho = e \sum c_i Z_i$, where e is the elementary charge, Z_i is the valence on the ion and c_i is the local ion number density (concentration). The ions can be assumed to follow a Boltzmann distribution, thus equation 4.8 becomes:

$$\nabla^2 \phi = -\frac{e}{\varepsilon_r \varepsilon_0} \sum_i c_i^0 Z_i \exp\left(-\frac{Z_i e \phi}{k_B T}\right) \quad (4.9)$$

where c_i^0 is the bulk ion number density, k_B is the Boltzmann constant and T is the temperature. This is known as the Poisson-Boltzmann equation. If the electric potential is in one dimension depending only on the distance from the charged surface, x , and if the electric potential is small (i.e. $\frac{Z_i e \phi}{k_B T} \ll 1$), then equation 4.9 has a simple analytical solution:

$$\phi(x) = \phi_0 e^{-\kappa x} \quad (4.10)$$

where ϕ_0 is the potential at the surface, and κ is given by

$$\kappa = \left(\frac{e^2 \sum_i c_i^0 Z_i^2}{\varepsilon_r \varepsilon_0 k_B T} \right)^{1/2} \quad (4.11)$$

For a symmetric monovalent electrolyte solution, this expression is simplified to:

$$\kappa = \left(\frac{2e^2 c_o}{\epsilon_r \epsilon_o k_B T} \right)^{1/2} \quad (4.12)$$

The inverse of κ is known as the Debye length ($\lambda = \kappa^{-1}$), and is the characteristic distance from the charged surface over which the potential decays exponentially to $1/e$. Thus, it is often considered as a charge carrier's net electrostatic effect in solution. In the case of our charged surface, it is the distance to which the electrostatic effects from the charge surface persist in the adjacent ionic solution. For a 100 mM KCl solution, $\lambda = \sim 1$ nm. While ions in the Stern layer remain immobile, the counter ions contributing to the Debye layer are mobile and can contribute to the ionic current when an external electric field is applied.

The Poisson-Boltzmann equation also describes the distribution of cations and anions within the solution. For a negatively charged surface, the concentration of cations will be large very close to the charged surface and will decay exponentially, eventually reaching the bulk concentration. At the same negatively charged surface, the concentration of anions will be low at the surface and increase to the bulk concentration away from the surface.

We now have an understanding of how charge on the surface of a nanopore can influence the concentrations of cations and anions near a surface. Often the surface charge is tuned by chemical modifications, however an alternative approach is to actively control the cation and anion populations near a surface by utilizing the field effect, similar to how a MOSFET can regulate the electron and hole population within a conductive channel (Guan, et al., 2014).

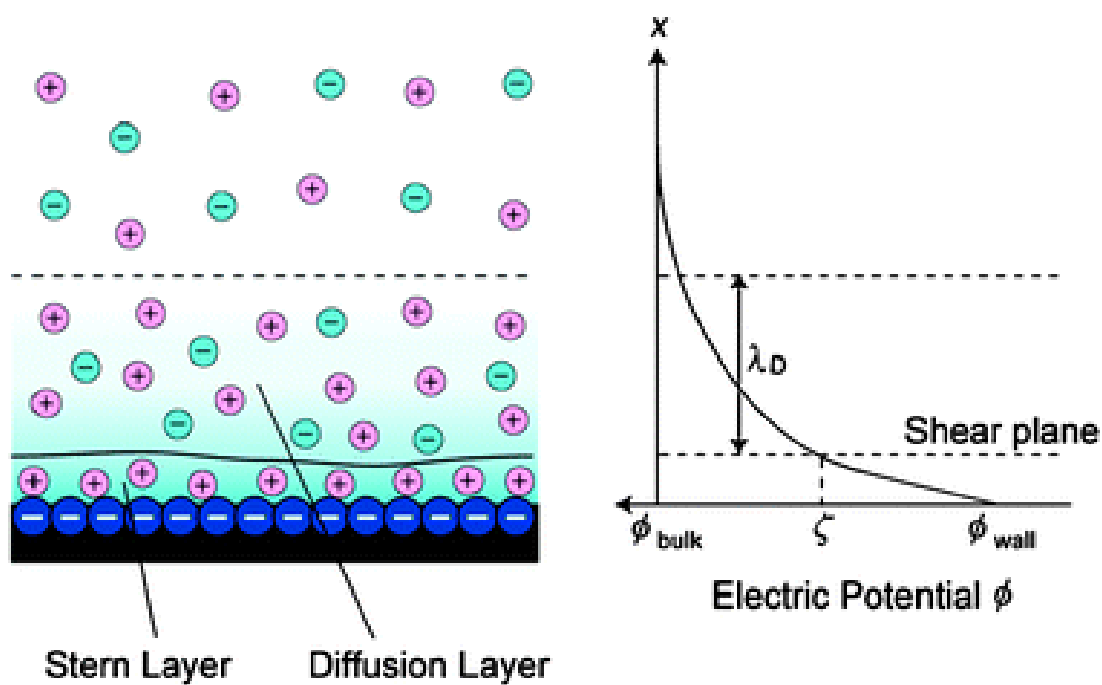


Figure 4.1: Schematic illustration of electric double layer (left) and electric potential profile normal to the negatively charged surface. Taken from (Daiguji, 2010).

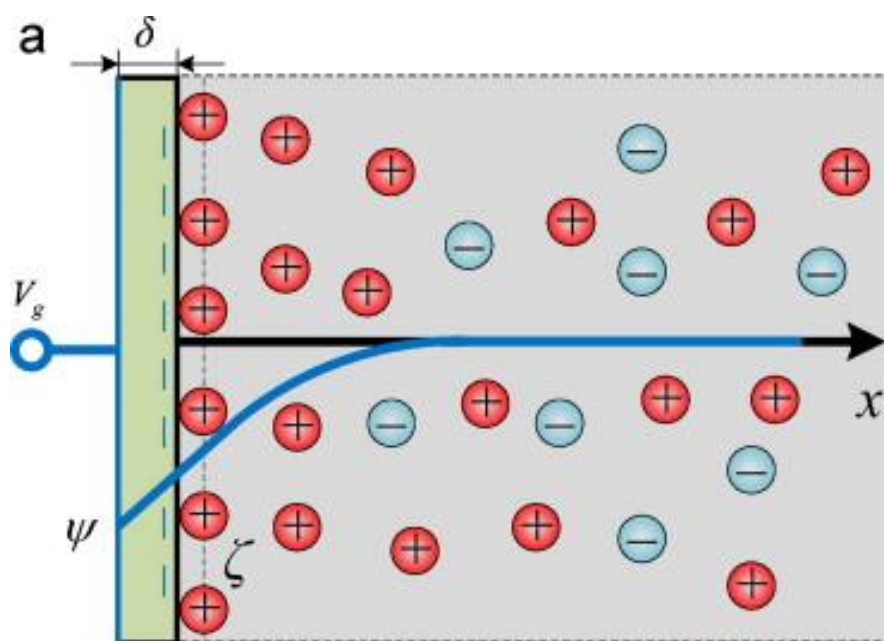


Figure 4.2: Schematic illustration of the field effect control of the ionic distribution near a planer surface. Taken from (Hu, et al., 2012).

We will continue with the model of a charged planar surface where the potential in the adjacent solution is described by the Poisson-Boltzmann equation. As is often the case when creating a gate electrode, we can coat the surface with a thin layer of dielectric material, with thickness δ , to prevent electrolysis when a voltage, V_g , is applied to the surface (figure 4.2). Due to the absence of charge within the dielectric layer, the potential inside the dielectric material is governed by Laplace's equation, $\nabla^2\psi = 0$. Following the derivation of (Hu, et al., 2012), the boundary conditions associated with the electric potential at the interface between the dielectric material and the solution are as follows:

$$\phi = \psi = \zeta \quad \text{at } x = 0 \quad (4.13)$$

$$\epsilon_o \epsilon_r \frac{\partial \phi}{\partial x} - \epsilon_o \epsilon_d \frac{\partial \psi}{\partial x} = -\sigma_s \quad \text{at } x = 0 \quad (4.14)$$

Where ζ is the zeta potential at the planar surface, ϵ_d is the relative permittivity of the dielectric material, and σ_s is the surface charge density. The variable x is the distance from the surface, where $x = 0$ is at the interface between the dielectric and the ionic solution. Boundary condition (4.13) states that the potential is continuous across the interface. Boundary condition (4.14) states that the potential satisfies Gauss's law, where the electric field is not continuous at the interface due to the discontinuity of the electric permittivities at the interface.

The boundary condition between the gate electrode and the dielectric layer is that $\psi = V_g$ at $x = -\delta$. Thus,

$$\frac{\partial \psi}{\partial x} = \frac{V_g - \zeta}{\delta} \quad (4.15)$$

Substituting equation 4.10 and equation 4.15 into equation 4.14 and evaluating at $x = 0$, the zeta potential becomes

$$\zeta = \frac{\sigma_s \delta + \epsilon_o \epsilon_d V_g}{\epsilon_o \epsilon_r \kappa \delta + \epsilon_o \epsilon_d} \quad (4.16)$$

From this expression, we can see that the zeta potential at the surface of the fluid is linearly proportional to the externally applied gate voltage. The strength of the potential is also dependent on the properties of the dielectric layer as well as the Debye length of the solution. For a 500 mV gate voltage applied across a thin 2 nm layer of dielectric material ($\epsilon_r = 4$) with a surface charge of 200 mC/m², adjacent to a 100 mM KCl solution, $\zeta = 300$ mV. While this expression is for a simplified case, it illustrates that an embedded gate electrode can be used to actively control the potential within the fluid.

We can now extend these concepts to the surface of a pore. In a micron sized pore, the Debye length is usually much smaller than the dimensions of the pore, thus the solution inside the pore is mostly neutral (figure 4.3a). The electric potential decays rapidly to its bulk value on the order of the Debye length, and the concentration of cations and anions within the pore is equal to the bulk concentration (figure 4.3c,e). However, if we consider a nanopore with a radius less than the Debye length ($R < \lambda$), the EDL of the pore walls can overlap and the electric potential even at the center of the pore is still effected by the surface charge (figure 4.3d). The concentration of ions within the pore is not equal to the bulk value and will be dominated by cations, in the case of a negatively charged pore (figure 4.3b,d,f). This leads to a cation selective pore.

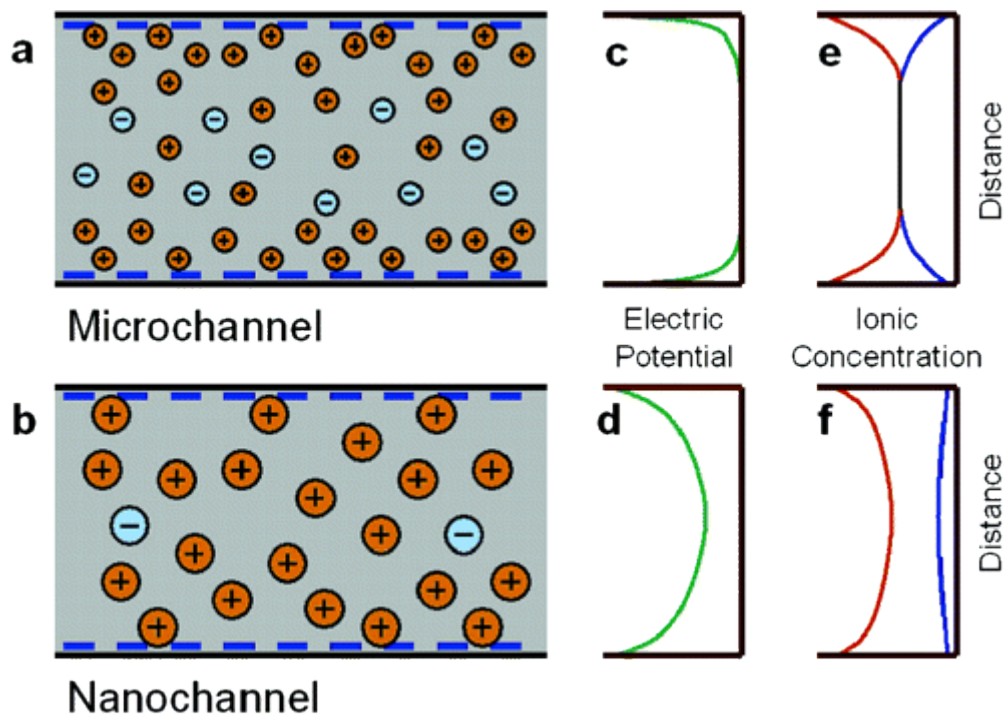


Figure 4.3: Schematic of effect of surface charge in micro and nano channels. (a, c, e) In a microchannel the Debye length is usually much smaller than the channel dimensions, thus the electrical potential quickly decays to the bulk value and the concentration of cations and anions within the pore is the bulk concentration. (b,d,f) In a nanochannel, the Debye length is the same order of magnitude as the channel dimensions, thus the EDL from either wall overlap. The electric potential and concentration of anions and cations at the center of the channel are affected by the charge at the surface and are not equal to bulk values. Taken from (Karnik, et al., 2005).

Apart from tailoring the pore dimensions to create EDL overlap, the concentration of the ionic solution also plays a role in determining if EDL overlap will occur. At high concentrations the Debye length is much smaller than the pore radius R , and bulk behavior will dominate inside the pore (figure 4.3a). If the concentration of the solution is decreased, then the Debye length can be larger than the pore radius and create an overlap of the EDL from the pore walls (figure 4.3d). One can plot the conductance of a given pore against the solution concentration to observe where the transition from bulk to surface governed behavior takes place (figure 4.4). The green curve represents the bulk conductance model, equation 4.6. An additional term can be added to the bulk model to account for surface charge governed effects, where the conductance due to surface charge on a negatively charged pore can be expressed as (Smeets, et al., 2006)

$$G_s = \mu_+ \frac{|\sigma_s| \pi d}{l} \quad (4.17)$$

This corresponds to a fixed surface charge and is represented by the blue curve in figure 4.4. The conductance plateaus at low bulk concentrations because in this regime the Debye length is large enough such that the concentration of ions within the pore is determined by the fixed surface charge and not the bulk concentration. The red curve, which fits Smeets et al.'s experimental data most closely, is a model incorporating a variable surface charge. The inclusion of a surface governed conductance term was initially proposed for long pores and channels, such as that shown in figure 4.4, but has been demonstrated to be less effective for describing thin membranes (Venkatesan, et al., 2012; Shan, et al., 2013).

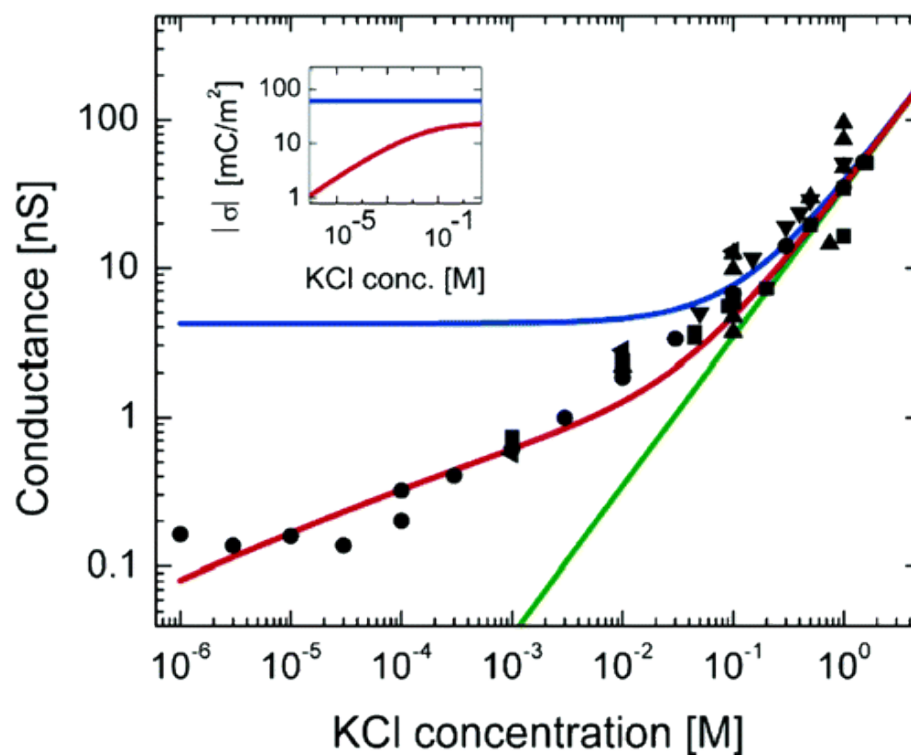


Figure 4.4: A plot of pore conductance against the bulk ionic concentration for nanopore devices from (Smeets, et al., 2006). Black symbols are experimental data points. Green curve represents a bulk conductance model (equation 4.1), Blue curve represents a conductance model incorporating a fixed surface charge while red curve represents a model with variable surface charge. Inset plots surface charge against bulk concentration. Figure taken from (Smeets, et al., 2006).

While the Debye length is good measure of the extent of a charge carrier's effect in solution, recently it has been shown a charged surface's effect in solution can exceed beyond the Debye length of the solution (Vlassiouk, et al., 2008). For the case of a thin pore where the membrane surface has the same charge as that on the pore wall, ion concentrations along the membrane surface become significant in contributing to the pore selectivity (Vlassiouk, et al., 2008). In a separate study, it was observed by Rollings et al. that thin graphene membranes with nanopores up to 20 nm in diameter show cation selectivity over anions in solutions where the Debye length is less than 1 nm. This was attributed to a surface-conduction mechanism, where mobile cations drawn to the negatively charged surface of the graphene are at an increased concentration in comparison to anions. This contributes to a large cation-selective current near the surface, thus causing the total ionic current to be cation-selective (Rollings, et al., 2016).

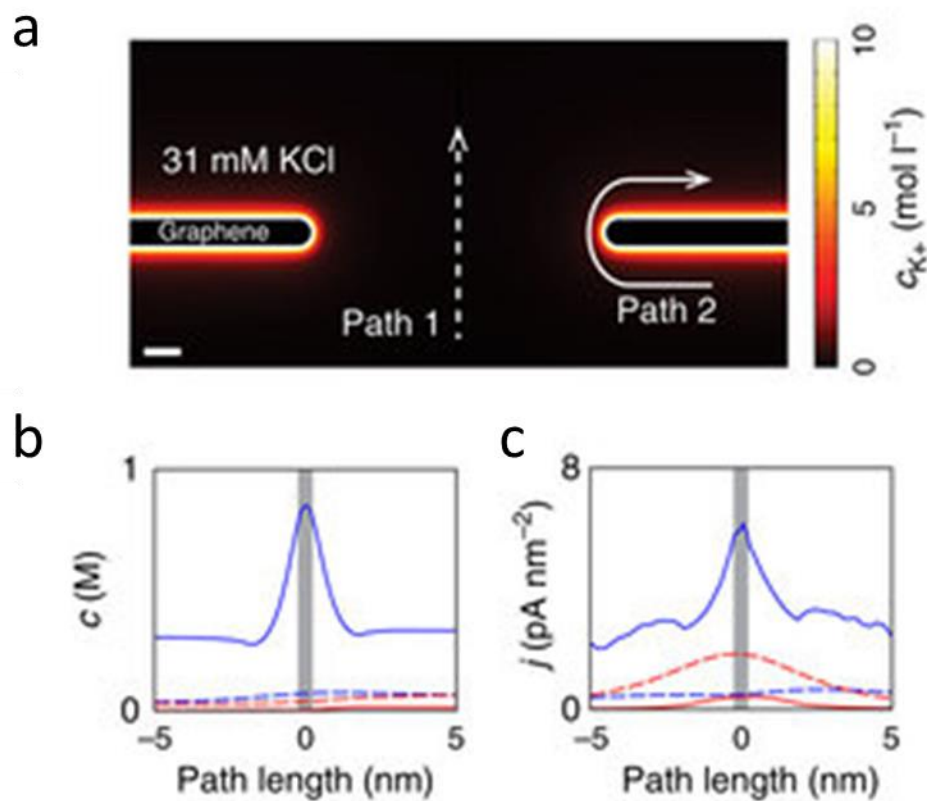


Figure 4.5: (a) Diagram of cross section of thin graphene nanopore. Path 1 (dashed line) depicts bulk transport mechanism while path 2 (solid line) depicts a surface transport mechanism. Color scale indicates the concentration of K^+ ions. (b) Concentrations and (c) current densities of K^+ (blue) and Cl^- (red) along each path illustrated in (a). Taken from (Rollings, et al., 2016).

4.2: Electrically driven fluid transport

Ions can be moved by electrical, concentration, thermal and pressure gradients. The system of interest to us is that of an electrical current flowing through a pore held at room temperature in atmospheric conditions, thus thermal and pressure gradients can be neglected. To describe the ionic flux under the influence of both an ionic concentration gradient and electric field, we use the Nernst-Planck equation, which represents Fick's law of diffusion while accounting for the electrostatic interactions on the diffusion of the ions: As described in section 4.1, the Poisson equation describes the electric potential acting on the diffusing particles. These two equations can be solved simultaneously to determine the internal electric field and concentration profile within a pore. This is known as the Poisson-Nernst-Planck (PNP) model and has been the starting point for many significant calculations describing protein ion channels and solid-state devices (Hille, 2001; Kuyucak, et al., 2001). Because this is a continuum approach, the model is not concerned with individual particles. It uses average concentrations and assumes ions move in averaged electric fields. While these simplifications have proven useful in looking at the behavior of macroscopic media, such as a large collective of ion channels in a nerve fiber, or the porous network of polymer membranes, they have become less applicable to the nanoscale dimensions of single nanopores and single biological ion channels, where the interactions between individual particles becomes more significant.

An alternative model to describe electro diffusion is Brownian dynamics, where the individual trajectories of each ion are calculated in time, so one can witness the path of each ion as it is driven by both Brownian motion and electrostatic forces as the ion

encounters external fields, local fixed charges and other local ions (Hille, 2001). However, one can also arrive at the continuum PNP equation from Brownian dynamics, using reasonable approximations (Fluinski, et al., 2005; Kosinska, 2006; Jain, et al., 2015).

Let us consider a cylindrical pore of length L and radius R , with the central axis of the pore along the z -axis (figure 4.6). There is a distribution of charge along the length of the pore in addition to a voltage bias across the pore, which both contribute to the potential, $\phi(z)$. The external component of the potential is the linear voltage drop across the length of the pore, $\phi_{ext}(z) = V_o - Uz/L$, where $U = V_o - V_L$. The function describing the internal component of the potential depends on how the fixed charges are distributed within the pore. The Smoluchowski equation describes the distribution of the positions of Brownian particles under the influence of forces, such as an external field (Dhont, 1996). Following the derivations of (Kosinska, 2006; Fluinski, et al., 2005), the 1-D form of the Smoluchowski equation that contains the electrostatic field can be written as,

$$\frac{\partial}{\partial t} c(z, t) = -\frac{\partial}{\partial z} j(z, t) = \frac{\partial}{\partial z} D e^{-\frac{z_i e \phi(z)}{k_B T}} \frac{\partial}{\partial z} e^{\frac{z_i e \phi(z)}{k_B T}} c(z, t) \quad (4.19)$$

Where $j(z, t)$ is the probability density current describing the flux produced by the diffusion of ions, D is the diffusion coefficient, and $\phi(z)$ is the potential function that describes the electrostatic field. $c(z, t)$ describes the local ion concentration, k_B is the Boltzmann constant, T is the temperature, z_i is the ion valence, and e is the elementary charge.

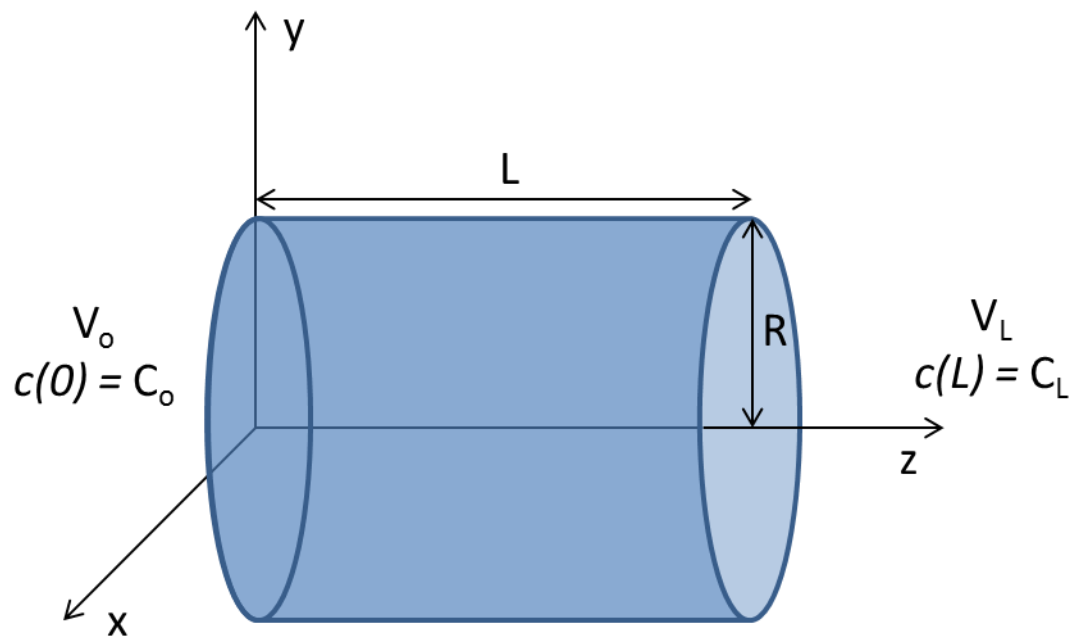


Figure 4.6: Schematic of cylindrical pore in Cartesian coordinates, with the z axis along axis of the pore. The pore has length L and radius R . V_o and V_L are the external potentials and C_o and C_L are the concentrations at either end of the pore, respectively.

In one dimension, the stationary overall current is simply the current density multiplied by the pore's cross section area. For the case of a cylindrical pore, $J_i = \pi R^2 j(z)$.

The stationary effective Smoluchowski equation then reads as

$$\frac{\partial}{\partial z} e^{\frac{z_i e \phi(z)}{k_b T}} c(z) = -\frac{J_i}{\pi R^2 D} e^{\frac{z_i e \phi(z)}{k_b T}} \quad (4.20)$$

Evaluating across the length of the pore from 0 to L, the electrical current resulting from the mass current is then

$$I = FJ = F \pi R^2 \frac{D}{L} \frac{c_o e^{\frac{z_i e \bar{\phi}(0)}{k_b T}} - c_L e^{\frac{z_i e \bar{\phi}(L)}{k_b T}}}{\int_0^L dz e^{\frac{z_i e \bar{\phi}(z)}{k_b T}}} \quad (4.21)$$

where C_o and C_L are the concentrations $c(o)$ and $c(L)$ respectively, and $\bar{\phi}(z)$ is the radially averaged potential. It has been demonstrated that equation 4.21 can describe non-linear I-V characteristics observed in ionic transport across nanopores, linking rectification and voltage-activated I-V behaviors in biological and synthetic channels to the shape of the underlying potential within the pore, $\phi(z)$, as shown in figure 4.7 (Jain, et al., 2015; Kosinska, 2006; Fluinski, et al., 2005; Radenovic, et al., 2008). While this derivation is for a cylindrical pore, the model has been generalized to describe a pore with varying cross section (Fluinski, et al., 2005).

Furthermore, the model has been extended to describe ion selective behavior by incorporating ion hydration (Jain, et al., 2015). Ions in solution are surrounded by a shell of water molecules, due to the attraction between an ion and the surrounding polar solvent. Different ions hold onto their hydration shells more or less tightly than one another, depending on the size and charge of the ion. An ion's hydration energy describes how

tightly it holds surrounding water molecules in its hydration shell. When an ion attempts to move through a pore smaller than its hydrated diameter, the ion is forced to shed or partially shed its hydration shell. Thus, by incorporating into the potential function $\phi(z)$ the energy penalty associated with shedding a hydration shell, one can reasonably account for inter-cation selectivity within the PNP model.

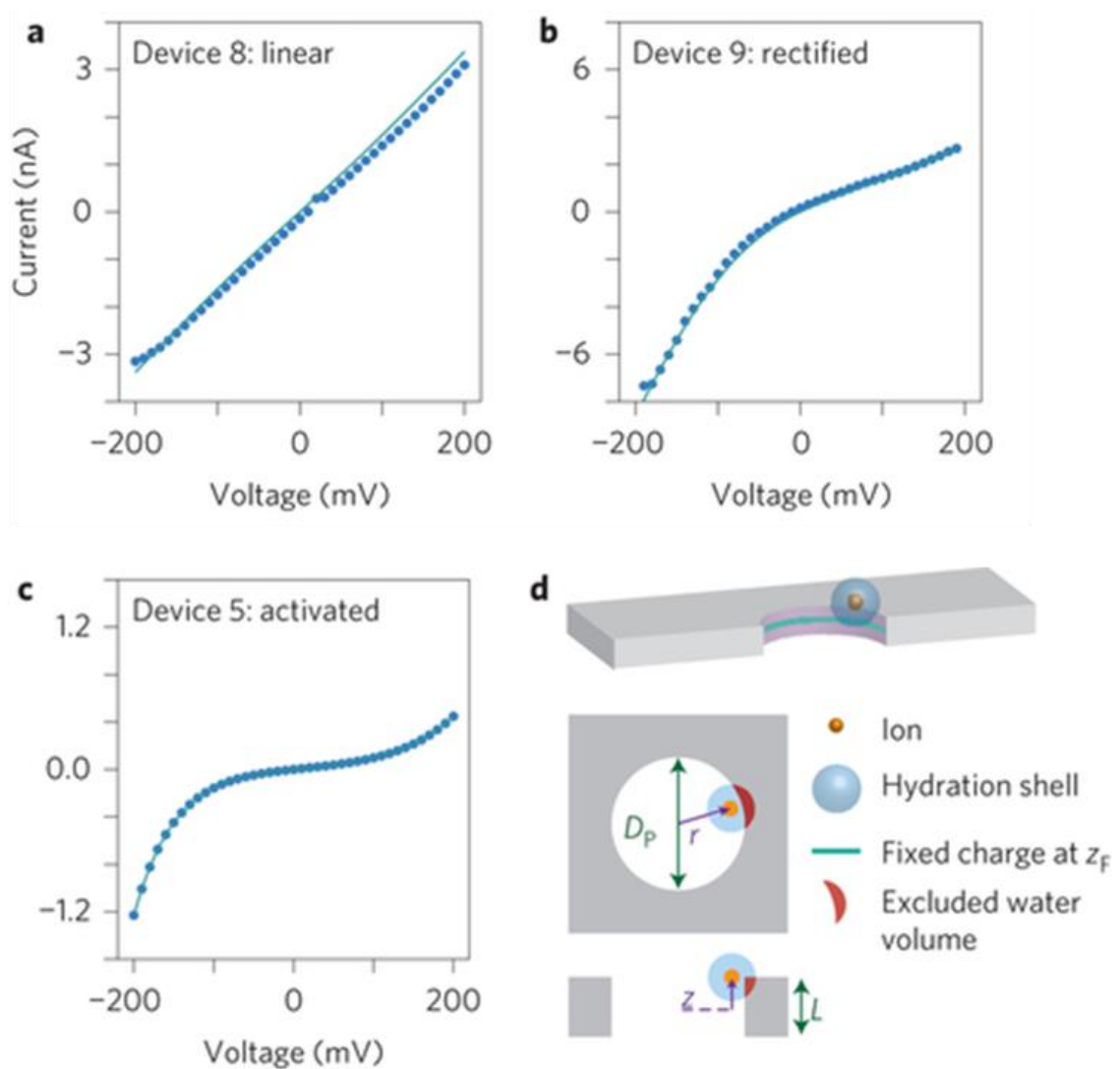


Figure 4.7: PNP model fit to non-linear I-V curves. Symbols represent experimentally measured I-V curves of transport through a graphene nanopore in 1M KCl (linear (a), rectified (b), and activated (c)) with fits from the transport model (lines). Model geometry for the graphene nanopore (d). Taken from (Jain, et al., 2015).

4.3: Hydrophobic interactions

Another mechanism by which to control fluid transport through a pore is hydrophobic interactions. In contrast to electrostatic interactions, hydrophobic interactions control the transport of water and all species within it. However before discussing hydrophobic gating within nanopores, the concepts of surface energy, hydrophobicity and electro wetting will be introduced.

Short-range forces of attraction existing between molecules are responsible for the liquid state, where molecules located within the bulk of a liquid are on average subjected to equal forces of attraction in all directions (Shaw, 1980). However molecules located at a liquid-air interface experience unbalanced attractive forces resulting in a net pull inward toward the bulk (figure 4.8). This makes it energetically favorable for a liquid molecule to be in the interior rather than to be located at the surface and for this reason droplets of liquid tend to contract into a spherical shape. The surface energy quantifies the disruption in the balance of intermolecular forces when a surface is created, and can be defined as the work required to increase the area of a surface isothermally and reversibly by a unit amount (Shaw, 1980). The short range intermolecular forces that are responsible for surface energy include van der Waals forces, hydrogen bonding, for example in water, and metal bonding, for example in mercury. Due to hydrogen bonding, the cohesive forces in water are quite strong which results in a relatively high value for the surface energy.

Wetting describes the displacement from a surface of one fluid by another, therefore it involves three phases, at least two of which must be fluids (Shaw, 1980). In the case where a droplet of water is in contact with a solid surface, gas is displaced by a liquid at

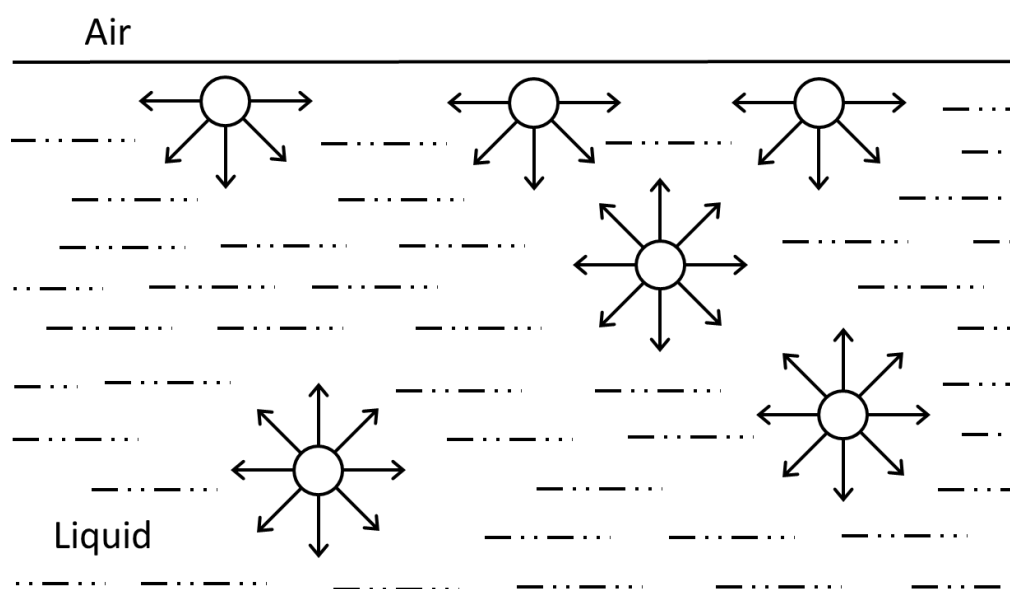


Figure 4.8: Illustration of the intermolecular forces acting on the molecules within the bulk and at the surface of a liquid. Molecules (represented here as circles) within the bulk of the liquid experience equal forces of attraction (arrows) in all directions, however molecules at the surface experience unbalanced attractive forces (Shaw, 1980).

the surface of the solid. A macroscopic measure of the wettability of a material is the contact angle. The equilibrium contact angle of a liquid on a solid surface is such that the total surface free energy is minimized. This is determined through an equilibrium balance at the three phase contact line, relating the surface energies between the water droplet, solid substrate, and surrounding air (figure 4.9A). The expression for the contact angle is given by Young's equation,

$$\cos\theta = \frac{\gamma_{sg} - \gamma_{sl}}{\gamma_{lg}} \quad (4.22)$$

where θ is the contact angle, and $\gamma_{sg}, \gamma_{sl}, \gamma_{lg}$ are the surface energies (J/m^2) at the solid-gas, solid-liquid and liquid-air interfaces, respectively. Contact angles greater than 90° are considered to be hydrophobic, while contact angles less than 90° are considered to be hydrophilic.

As quantified by the low contact angle, water easily spreads out and wets a hydrophilic surface. Thus, hydrophilic surfaces are considered to be high-energy surfaces because they can provide the work required to overcome the strong cohesive forces within water and create a surface between the water and the solid substrate. Conversely, hydrophobic surfaces are considered low-energy surfaces because the energy at the interface is not enough to overcome the cohesive forces within water and promote wetting.

To controllably change the wettability of a surface, the phenomenon of electro-wetting can be employed. In a typical electro-wetting set up, a droplet of water is placed on top of a dielectric surface and a voltage is applied between the dielectric and the water droplet (figure 4.9B). The effect of the applied voltage can be understood through thermodynamics, where the surface energy at the interface is considered to be a function of

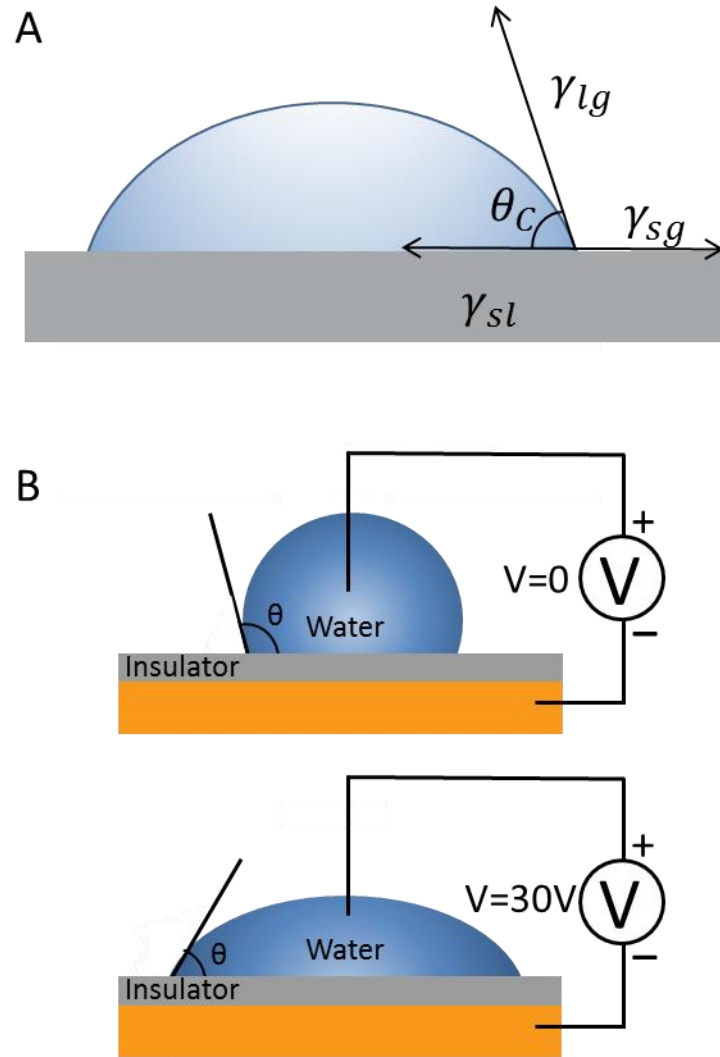


Figure 4.9: (A) diagram of contact angle measurement at the three phase contact line. (B) Schematic illustration of electro-wetting phenomena on planer surface. When a voltage is applied, the surface between the water and substrate increases, decreasing the contact angle.

of both chemical and electrical components. Applying a voltage across the interface increases the surface energy due to additional charge on the capacitor formed between the droplet and the dielectric, thus the contact angle will decrease.

With the additional energy stored in the system from the capacitor formed between the droplet and the dielectric, Young's equation is now expressed as

$$\cos \theta_V = \frac{\gamma_{sg} - \gamma_{sl} + \frac{\epsilon_o \epsilon_d V^2}{2d}}{\gamma_{lg}} = \cos \theta + \frac{\epsilon_o \epsilon_d V^2}{2d \gamma_{lg}} \quad (4.23)$$

Where $\cos \theta$ is the original contact angle without the application of an additional voltage, and $\cos \theta_V$ is the contact angle with the application of voltage V . Through molecular dynamic simulations, it has been shown that for water residing on a graphene surface, large changes in contact angle can be achieved from modest voltages applied to the graphene sheet (Ostrowski & Eaves, 2014).

With an understanding of what it means to be hydrophobic, we can now turn our attention to a hydrophobic nanopore. When hydrophobic surfaces form a confined geometry such as a nanopore, it is possible for water within the constrained volume to evaporate, creating a vapor gap (Luzar, 2004; Jones, et al., 2015). Spontaneous evaporation is controlled by a competition between bulk energetics (favoring the liquid phase) and surface energetics (favoring the vapor phase) (Luzar, 2004). For a volume of water confined between two approaching planer hydrophobic surfaces of finite size, Luzar proposed that the critical distance at which the confined water will transition to vapor can be estimated by equating the grand potential of the confined liquid and the confined vapor (Luzar, 2004),

$$\Omega_l \approx -PV + 2A_s\gamma_{sl} = \Omega_g \approx -P_gV + 2A_s\gamma_{sg} + A\gamma_{lg} \quad (4.24)$$

where P is the bulk pressure and P_g is the coexisting vapor pressure, $V = A_sD$ is the volume of the confined region, $A_s \propto L^2$ is the area of the planar surfaces, and $A\gamma_{lg}$ is the area of the liquid-vapor interface. For a liquid, one can approximate the difference in pressures as $\rho\Delta\mu$, where ρ is the number density of the liquid, $\Delta\mu$ is the difference in chemical potential of bulk liquid and the value at liquid-gas coexistence. Using Young's equation, where $\gamma_{sl} - \gamma_{sg} = -\gamma_{lg}\cos\theta$, the critical distance can be expressed as

$$D_C \cong \frac{-\gamma_{lg}\cos\theta}{\rho\Delta\mu + \frac{b\gamma_{lg}}{L}} \quad (4.23)$$

where b is a geometry dependent constant on the order of unity. For water confined between two planer hydrocarbon surfaces, characterized by a contact angle of $\sim 110^\circ$, and at ambient conditions, the transition from water to vapor is predicted to occur at a critical distance on the order of 100 nm (Luzar, 2004). While here the critical distance for transition is predicted by thermodynamic equilibrium, it can also be predicted via kinetic theory, by investigating capillary evaporation within a confined geometry using atomistic simulations (Leung, et al., 2003). From kinetic theory, the critical threshold distance, D_C^k , is shown to be much smaller, on the order of a nanometer. Liquid water in the regime between D_C^k and D_C is considered to be in a metastable state (Debenedetti, 1996; Luzar, 2004) (figure 4.10).

Through molecular dynamic simulations, this type of hydrophobic barrier has been proposed and validated as a mechanism for gating in biological ion channels (Aryal, et al., 2015; Beckstein & Sansom, 2004; Beckstein, et al., 2001; Beckstein & Sansom, 2003; Trick, et al., 2014; Hummer, et al., 2001). The concept of hydrophobic gating was first

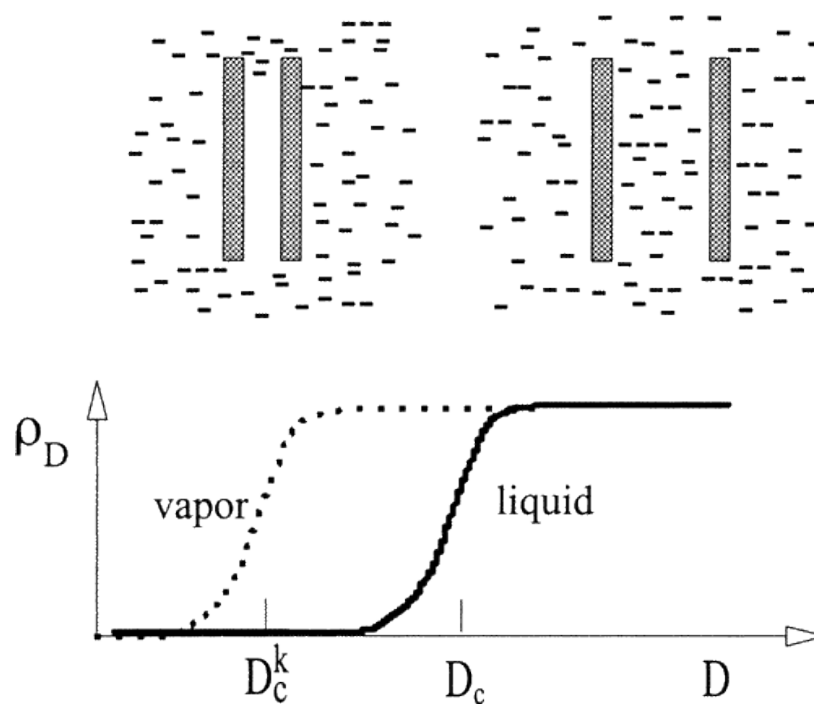


Figure 4.10: (A) Illustration of the critical distance D_C for stable vapor (left) and liquid (right) states to occupy the space between two hydrophobic planer surfaces.(B) a graphical representation of the spacing required for liquid and vapor states, plotting the fluid density, ρ_D , against the inter-surface separation, D . D_c and D_c^k denote the thermodynamic and kinetic threshold, respectively, for the spontaneous evaporation of a confined liquid, the area between the two thresholds signifies the space where a metastable liquid may exist. Image taken from (Luzar, 2004).

carried out on simple model nanopores, where the pore was not physically occluded but could be shown to form a hydrophobic barrier as water molecules exhibited stochastic liquid-vapor transitions within the pore (figure 4.11). It has since been demonstrated that a narrow hydrophobic pore provides a significant energy barrier to ions in addition to water (Beckstein, et al., 2004). Thus, a hydrophobic pore with nanometer dimensions can appear impermeable to an ion even though the pore radius is much larger than that of the ion itself (Beckstein, et al., 2004).

Through MD simulations, it has been shown that electro-wetting is at the core of hydrophobic gating in biological ion channels. The presence of a transmembrane potential can reversibly open a functionally closed pore (dewetted) to the wetted state by modifying the surface energy of the pore walls (Dzubiella, et al., 2004; Vanzo, et al., 2014; Trick, et al., 2017). For the case of a biological ion channel, once ions have translocated across the membrane there is no longer a concentration imbalance, thus the transmembrane potential is reduced and the pore returns to its closed, dewetted state. Additionally, it has been shown that hydrophobic nanopores can have an intrinsic ion selectivity resulting from the differing dehydration energies of ions (Song & Correy, 2009).

The phenomena of hydrophobic gating has recently been demonstrated experimentally in solid state nanopore devices (Powell, et al., 2011; Smirnov, et al., 2011; Xiao, et al., 2016). In both studies, pores were treated with a hydrophobic coating and were shown to exhibit reversible switching between dry and wet states when a bias voltage was applied across the length of the pore with the resulting I-V curves shown to mimic that of biological voltage-gated channels (Smirnov, et al., 2011). While the hydrophobic gating

mechanism is rooted in the meta-stable state of water near hydrophobic surfaces, it has been suggested that the presence of residual trapped gas can also promote the process of dewetting (Innes, et al., 2015; Smirnov, et al., 2010). Gaseous nanobubbles residing in silicon nitride nanopores are not uncommon and have been detected by (Smeets, et al., 2006).

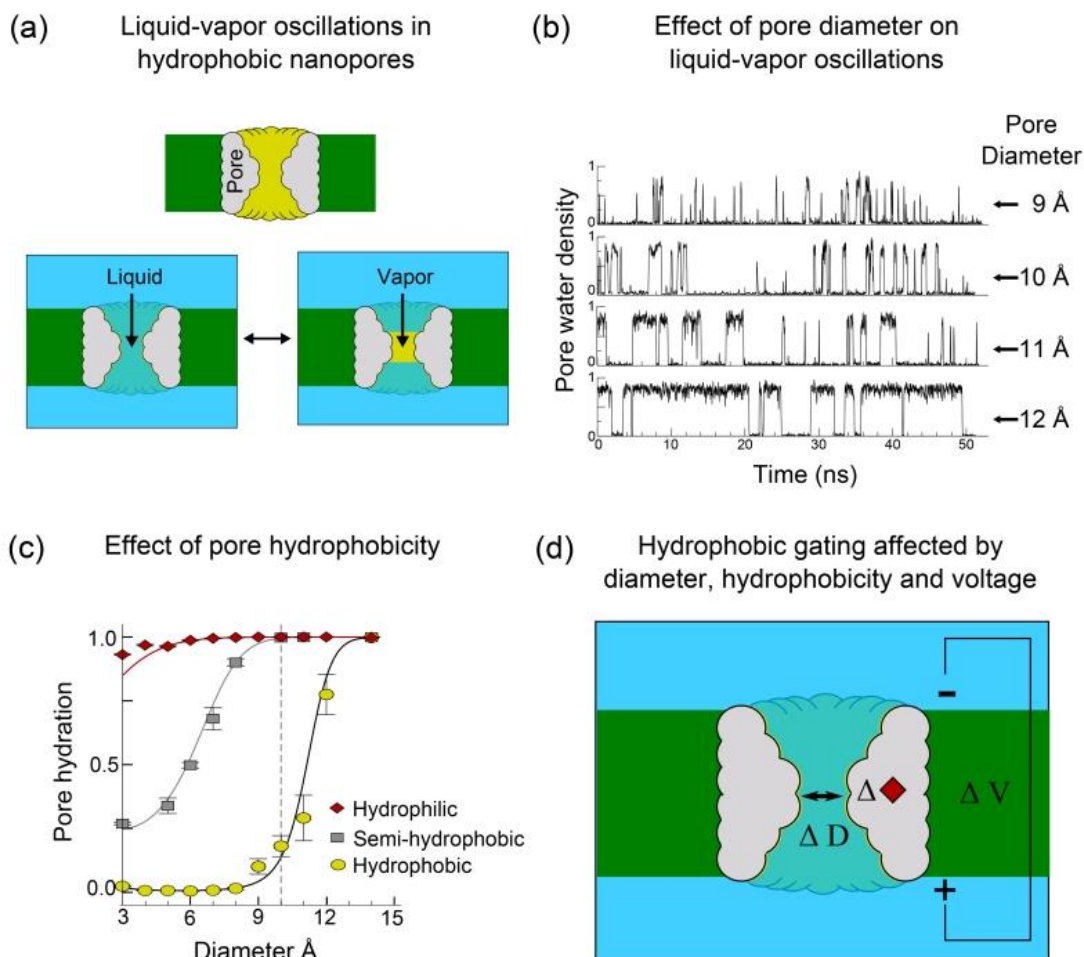


Figure 4.11: (a) illustration of a cross section through a hydrophobic nanopore. Hydrophobic regions are shown in yellow, the membrane is shown in green. (b) liquid-vapor oscillations occur within a hydrophobic nanopore. The stability of the wetted state depends on the pore diameter. (c) the stability of the wetted state also depends on the hydrophobicity of the atoms lining the pore walls. (d) The application of a transmembrane voltage can open the pore to a wetted state. Figure taken from (Aryal, et al., 2015).

CHAPTER FIVE: Voltage gated K^+/Na^+ selective nanopores from porous graphene

This chapter experimentally investigates ionic transport through graphene nanopores. Devices with pores ranging from sub-nm up to 350 nm were studied, with a subset of the devices exhibiting K^+/Na^+ selectivity and responsiveness to an applied gate voltage. The mechanisms by which to control ionic transport through a nanopore introduced in chapter 4 will prove useful in isolating the mechanism governing the behavior of the pores studied here. This chapter borrows heavily from our submitted publication, ‘Solid State Voltage Gated K^+/Na^+ Selective Ion Channels from Porous Graphene’, currently under review.

5.1: Device geometry and fabrication

The experimental device geometry consist of a monolayer graphene membrane suspended over a through hole in a silicon/silicon nitride support chip (figure 5.1). The silicon nitride support windows are defined using standard photolithography followed by a KOH etch of the underlying silicon. A 3–5 μm diameter through hole is then patterned in the center of the silicon nitride window and etched via reactive ion etching (RIE). Twenty nanometers of ALD Al_2O_3 is then deposited, conformally coating the entire support chip. This insulating layer of alumina is intended to reduce the likelihood of electrical shorting across the silicon support chip.

Monolayer graphene was obtained by both mechanical exfoliation and CVD growth. For exfoliated devices, graphene was exfoliated via the Scotch tape method onto a silicon wafer coated with 90 nm of PVP followed by 200 nm of PMMA. The thickness of

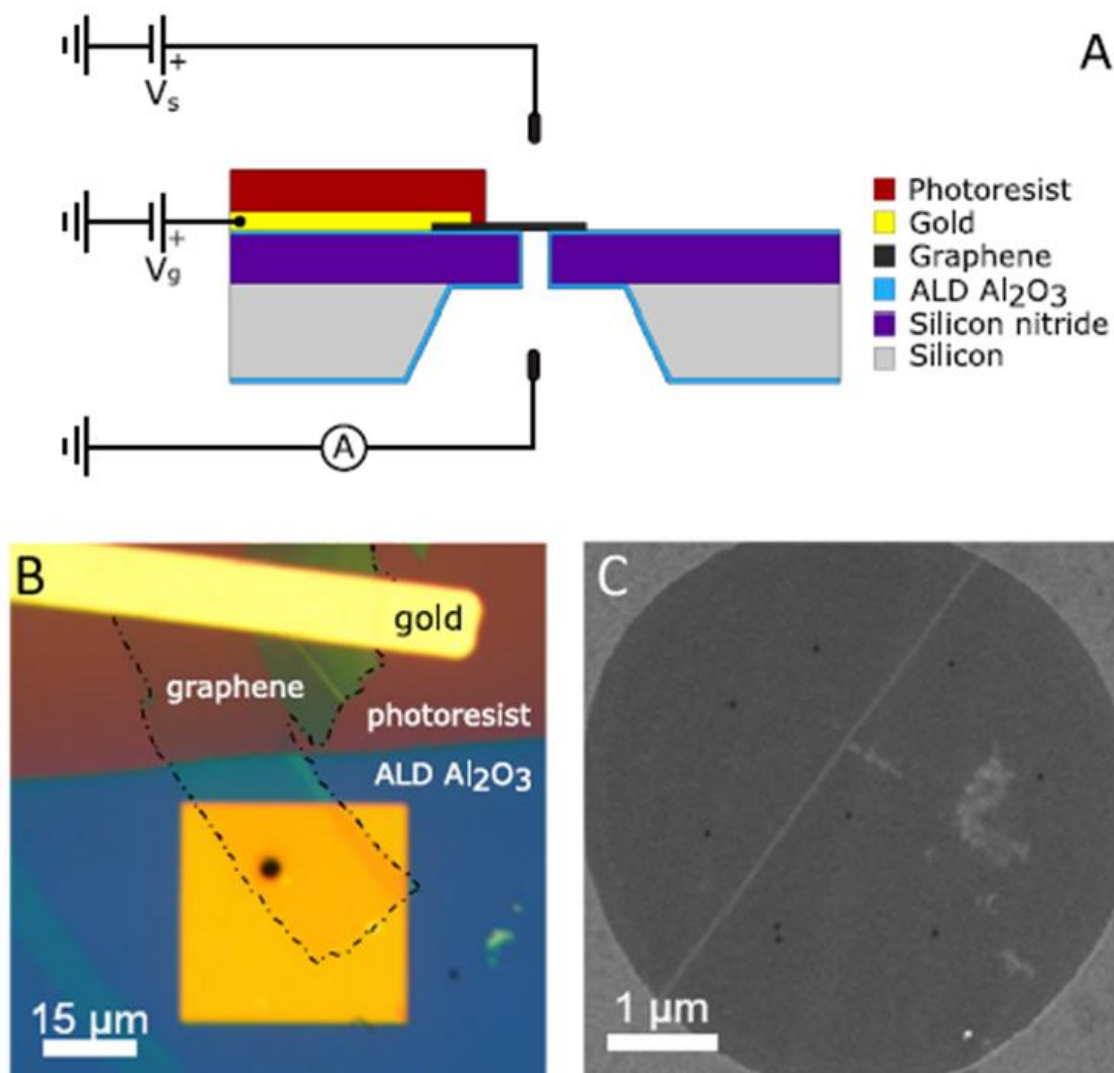


Figure 5.1: (A) Schematic of measurement circuit and cross section of device. Graphene is suspended over a 5 μm hole in a silicon nitride window and mounted in a custom microfluidic cell in which electrolyte solution is introduced to both sides of the graphene membrane. (B) Optical image of exfoliated graphene device, with graphene flake outlined. (C) HIM image of CVD graphene with nine 35 nm pores drilled using HIM, device CVD-6.

the stacked polymer substrate allows for graphene to be identified using an optical microscope, based on the optical contrast of the flake (Blake, et al., 2007). Once an exfoliated graphene flake is located using an optical microscope, the flake's thickness is confirmed using Raman spectroscopy (figure 5.2B). It is then transferred onto the silicon nitride support chip following a 'pick and place' transfer process based on the method described by Dean et al (Dean, et al., 2010). The graphene, PMMA, PVP, silicon stack is attached to a plastic support frame and floated atop a bath of deionized water (Figure 5.2C). PVP is a water soluble polymer, consequently the PVP dissolves and the silicon wafer is released from the graphene/PMMA/support frame structure and drops to the bottom of the water bath. The graphene/PMMA/support frame is then mounted in a custom built micro positioner that is used to align the flake over the 5 μm through hole in the silicon nitride support chip while viewing through an optical microscope. Using the micro positioner, the graphene/PMMA film is then brought into contact with the support chip, adhering the graphene flake to the new substrate via van der Waals forces. This transfer method allows for precise placement of an exfoliated graphene flake, which would otherwise be randomly located on the substrate on which it was exfoliated. After transfer, devices were annealed at 340 $^{\circ}\text{C}$ under 200 sccm Ar/100 sccm H_2 to remove PMMA residue.

CVD synthesized graphene was grown by collaborators at Lockheed Martin Advanced Technology Center. After a pre-synthesis anneal of the Cu foil substrate, CVD graphene was grown via low-pressure CVD. Following synthesis, the graphene, while still on the Cu foil substrate, was irradiated with 500 eV Xe^+ ions for a total fluence of $3.7 \times 10^{13} \text{Xe}^+/\text{cm}^2$. This process, which has been confirmed via STEM imaging not to introduce

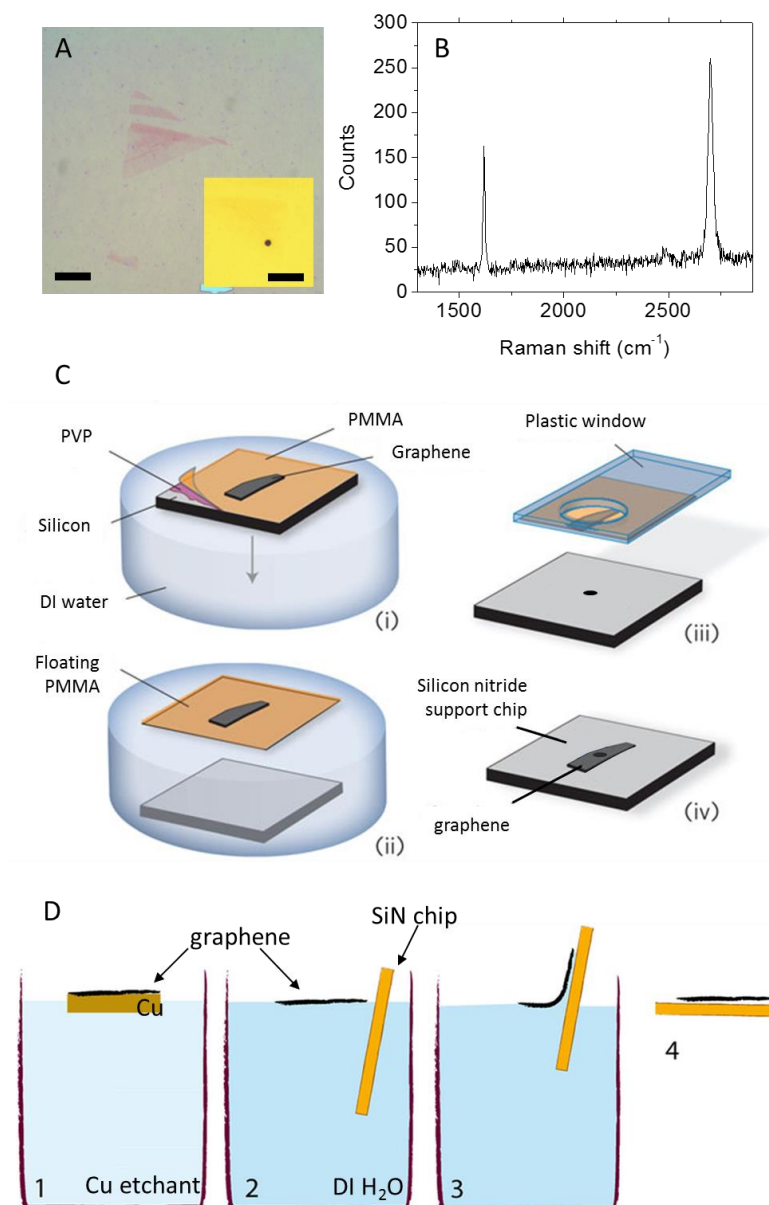


Figure 5.2: (A) Optical image of exfoliated graphene flake on PMMA/PVP/silicon substrate. Inset is of graphene on silicon nitride substrate after transfer. Scale bars, 25 μm . (B) Raman spectra for the exfoliated flake in (A). Monolayer graphene is identified by the ratio of the G to 2D peaks (Ferrari, et al., 2006). (C) Schematic of the pick-and-place transfer of exfoliated graphene flake onto silicon nitride substrate, adapted from (Dean, et al., 2010). (D) Schematic of CVD transfer process. (1) copper substrate is etched away from graphene in APS, (2) copper etchant is exchanged with DI water solution, (3) SiN support chip is used to scoop up graphene from the surface of water bath, (4) sample is left to dry. Adapted from (Ondarcuhu, et al., 2013).

defects into graphene, is done so that the graphene may be reliably transferred without use of a sacrificial polymer layer. The Cu foil substrate was then etched away with ammonium persulfate and the CVD graphene was transferred, without a sacrificial carrier layer, over the 5 μm through hole in the silicon nitride window. Once transferred, the graphene was exposed to 180 seconds of UVO to reduce hydrocarbon surface contamination. Through STEM imaging, this was confirmed not to introduce defects into the single-layer graphene itself.

In both exfoliated and CVD synthesized graphene devices, the gold gate electrode was patterned in contact with the graphene using standard photolithography. For CVD graphene devices, the entire silicon nitride chip is covered with a layer of CVD graphene, thus a shadow mask can be used to pattern the gate electrode at the edge of the support chip, away from the suspended graphene area. This is advantageous as it preserves the cleanliness of the suspended CVD graphene by not introducing additional polymers that could potentially leave residues on the graphene membrane. Because exfoliated graphene flakes are only 10–50 μm in size, the gate electrode must be patterned close to the suspended area and thus requires the use of photoresist to define the gate electrode. Five nanometers of chromium followed by 60 nm of gold are then deposited via thermal evaporation. In the case of exfoliated devices, an additional layer of photoresist (Shipley S1818) was patterned and hard baked (180 °C) over the gold electrode to electrically isolate the gold from the electrolyte solution.

Pores were introduced into graphene devices by several methods. To introduce pores into exfoliated graphene, devices were exposed to temperatures up to 200° C while

in air during the fabrication process. This likely introduced defects in the graphene via oxidation that enlarged into pores after exposure to 0.1M HCl (Yamada, et al., 2014; Coleman, et al., 2008; Bouleghlimat, et al., 2013).

CVD graphene samples were perforated by four different methods:

(1) Hyperthermal Xe⁺ irradiation with low-pressure atmospheric background:

Samples were baked overnight at an elevated temperature under vacuum. Xe⁺ irradiation with a fluence on the order of 10^{13} Xe⁺/cm² was performed using a custom-built ion chamber incorporating a Kaufman ion source, at an elevated temperature with an initial background pressure of 10^{-4} Torr of air before starting the source.

(2) Hyperthermal Xe⁺ irradiation in vacuum: Samples were irradiated with the

same chamber as described above, however with fluences on the order 10^{14} Xe⁺/cm² and performed with an initial background pressure of 10^{-6} Torr prior to starting the source.

(3) Site specific focused helium ion drilling: For HIM drilling, pores were drilled

using a Zeiss ORION NanoFab scanning HIM equipped with a gas field ion source (GFIS) using He⁺ ions at 25 kV. Small pores were drilled with a stationary beam in defined locations with a beam current of 0.5–2.0 pA, and a dwell time of 52 ms per pore. Larger pores were drilled by defining a pattern and dwelling the beam with a 1 nm pixel spacing over that region with a dose on the order of 1 nC/μm².

- (4) Broad (defocused) helium ion irradiation: Samples were again irradiated with the HIM using He^+ ions at 25 mV with a broadened 2 μm diameter beam for a total fluence of $8 \times 10^{16} \text{ He}^+/\text{cm}^2$. This was followed by 300 seconds of UVO.

Figure 5.3 depicts SEM and/or STEM images of pores in suspended graphene devices, while figure 5.4 shows pore size and distribution data for the CVD graphene devices perforated via Xe^+ irradiation. The variety of perforation methods were utilized in order to explore a large range of pore sizes, which would be otherwise unattainable using a single perforation method. Scanning transmission electron microscopy (STEM) imaging of the perforated CVD graphene membranes confirmed devices were made via Xe^+ irradiation with pores ranging from $\leq 1 \text{ nm}$, $\sim 1\text{--}5 \text{ nm}$, or $\sim 1\text{--}20 \text{ nm}$. HIM drilling produced single pores ranging from $\sim 25 \text{ nm}$ to $\sim 250 \text{ nm}$ in diameter. Additionally, the graphene on two devices tore to produce a single $\sim 240 \text{ nm}$ diameter pore and $\sim 350 \text{ nm}$ diameter pore, respectively. Table 5.1 summarizes the pore size and perforation methods for each device

Lastly, we should note the variety of perforation methods also results in variation in the molecular species terminating the pore sites, charge on the membrane, as well as the surface energy of the graphene. Devices that were exposed to oxygen during perforation (method 1) as well as those exposed to UVO (method 4) likely had a higher surface energy than devices perforated in vacuum. These considerations likely contribute to the variation in observed behavior, which we will discuss in more detail later in the chapter.

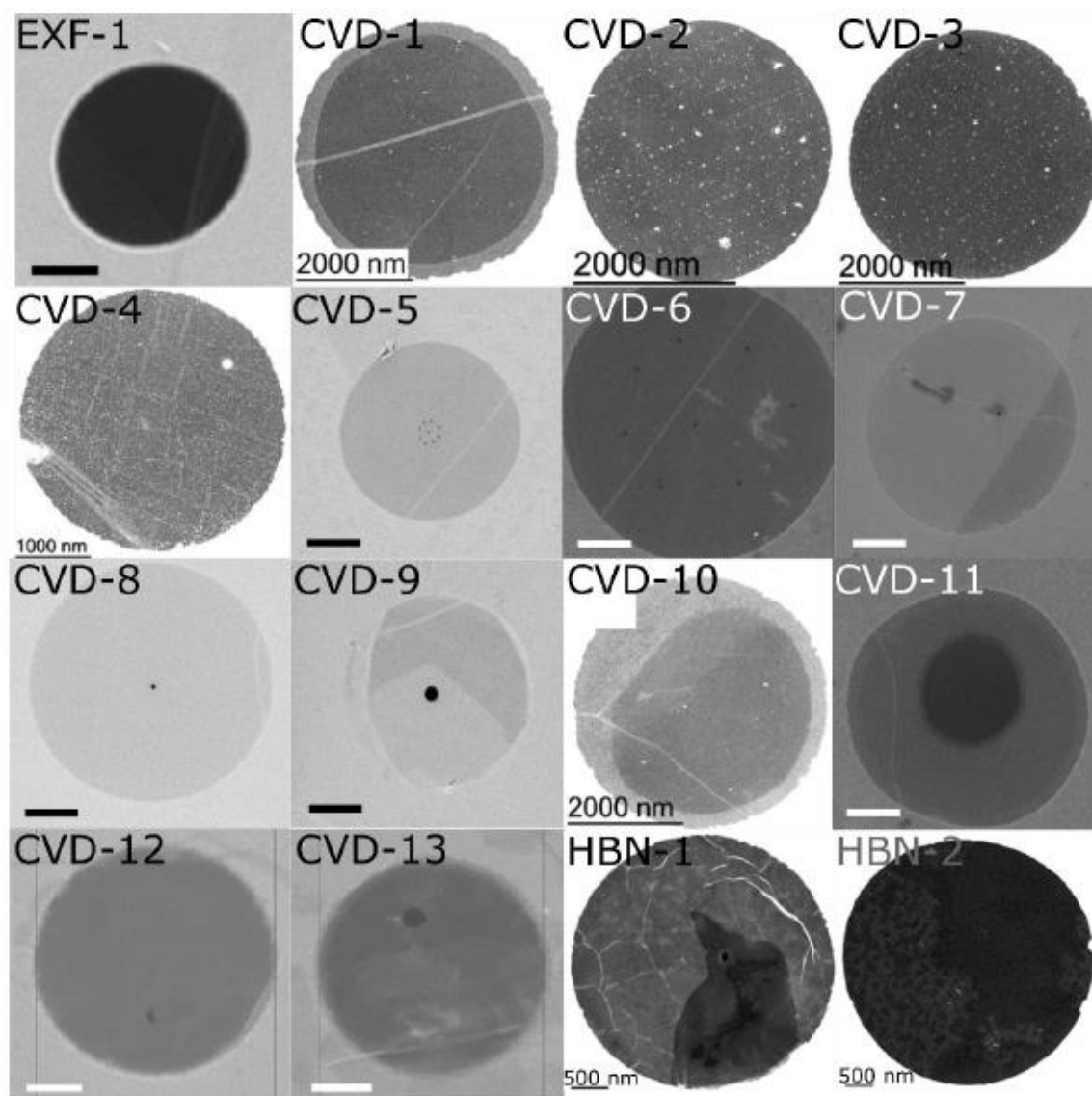


Figure 5.3: Composite STEM images (CVD-1 – CVD-4, CVD-10, HBN-1, HBN-2), HIM images (CVD-5 – CVD-9, CVD-11) and SEM images (EXF-1, CVD-12, CVD-13) of porous graphene and h-BN devices. Scale bar is 1 μm , unless otherwise noted.

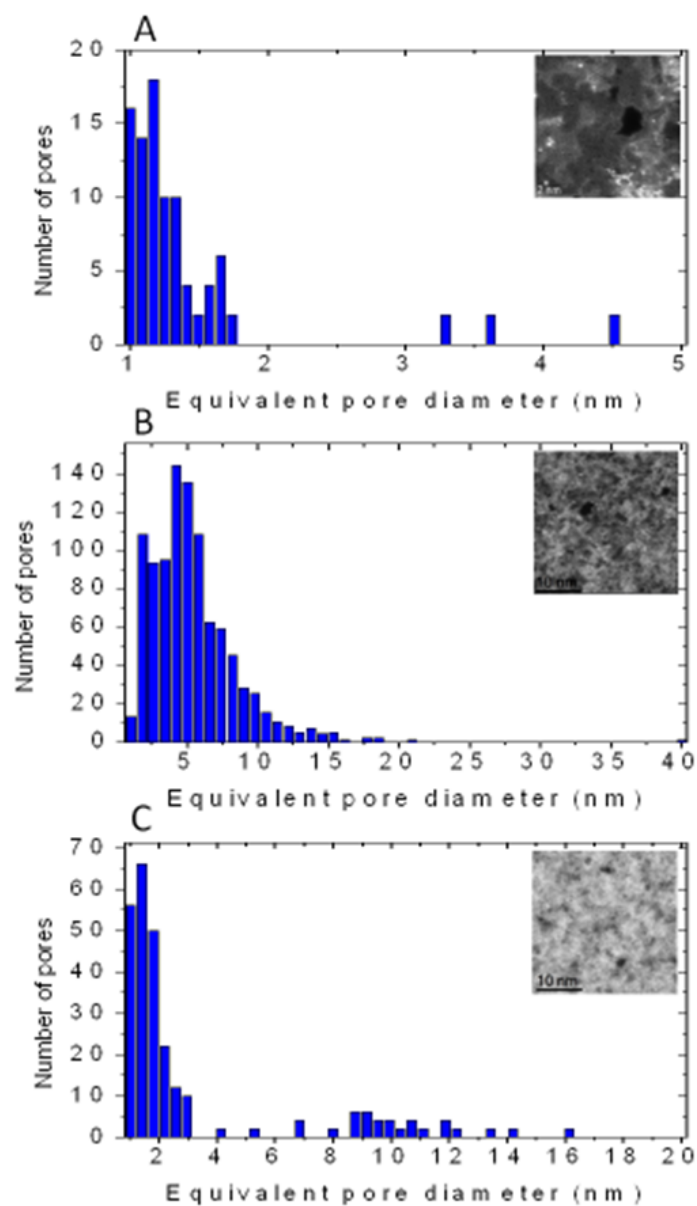


Figure 5.4: Pore size and distribution for Xe⁺ irradiated devices. (A) CVD-2, (B) CVD-3, and (C) CVD-10. Inset is a representative high magnification STEM image of select pores.

Device	Largest Imaged Pore Diameter	Number of pores	Perforation Method	IV Behavior	Gate Response
EXF-1	Not imaged	Not imaged	Oxidation/HCl	Non-linear	Yes
CVD-1	1.3 nm	Distribution	Ion bombardment (vacuum)	No ion conductance	No
CVD-2	4.5 nm	Distribution	Ion bombardment (vacuum)	No ion conductance	No
CVD-3	40 nm	Distribution	Ion bombardment (vacuum)	No ion conductance	No
CVD-4	23 nm	1	HIM drilling	Non-linear	Yes
CVD-5	28 nm	9	HIM drilling	Non-linear	Yes
CVD-6	35 nm	9	HIM drilling	Non-linear	Yes
CVD-7	48 nm	1	HIM drilling	Non-linear	Yes
CVD-8	76 nm	1	HIM drilling	Non-linear	Yes
CVD-9	245 nm	1	HIM drilling	Linear	No
CVD-10	16 nm	Distribution	Ion bombardment (LP-AB)	Non-linear	Yes
CVD-11	Not imaged	Not imaged	HIM broad beam, UVO treatment	Non-linear	Yes
CVD-12	240 nm	1	n/a	Linear	n/a
CVD-13	350 nm	1	n/a	Linear	n/a

Table 5.1: Catalog of the 14 porous graphene devices measured. Pore size, perforation method and corresponding I-V behavior.

5.2: Experimental design aspects

After perforation, the graphene on silicon nitride devices were mounted in a custom-made microfluidic cell, allowing for the introduction of electrolyte solution to both sides of the graphene membrane. The custom built microfluidic cell consists of a PDMS microchannel with three access ports, and was designed to allow for electrical and optical access to the top side of the graphene membrane (figure 5.5). Two microchannels, 50 μm tall and 2000 μm wide, were patterned into PDMS and bonded to a glass slide. Inlet ports are punched into the PDMS, with the graphene on silicon nitride chip mounted over the center ports that connect the two underlying microchannels. The silicon nitride support chip is mounted on the center port and adhered with PDMS, creating a seal to separate the reservoirs on either side of the graphene. Solution is then gently introduced to the microchannel and subsequently the bottom side of the membrane using a syringe pump. A drop of solution is placed on the top side of the device to create the opposing reservoir of solution.

Graphene membranes were first rinsed with ethanol for 2 minutes followed by deionized water to facilitate wetting of the nitride membrane. Once graphene devices were introduced to fluid, at least one side of the membrane remained in solution for the duration of the experiments. Devices were exposed to electrolyte solution for 5–10 minutes before conductance measurements were carried out, to allow the system to equilibrate. Solutions were left unbuffered to avoid any potential interactions between the graphene and solutes. For the duration of the experiments, solution pHs were within the range of 5.91 – 6.38. The slight acidity is due to the unbuffered solutions equilibrating with dissolved carbon dioxide

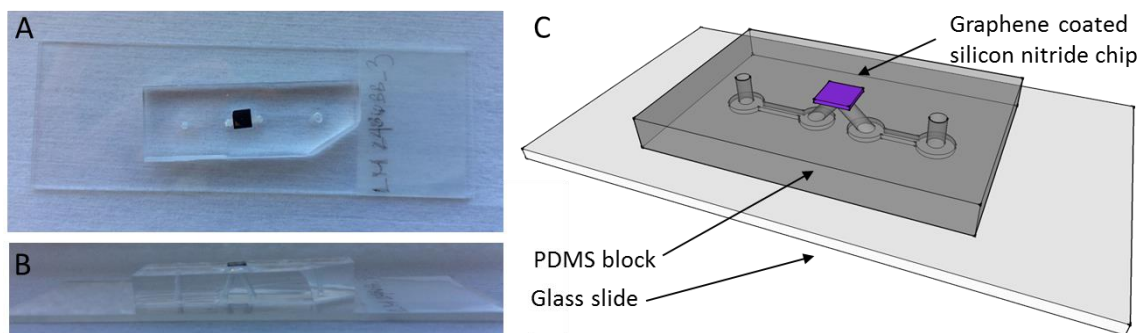


Figure 5.5: Optical images of (A) top view and (B) side view of graphene on silicon support chip mounted in microfluidic cell. (C) schematic of microfluidic cell. Microfluidic cell consists of microchannels patterned into PDMS block and plasma bonded to underlying glass slide (Underlying glass slide measures 1" x 3"). Graphene coated silicon nitride chip is adhered to the PDMS block using PDMS.

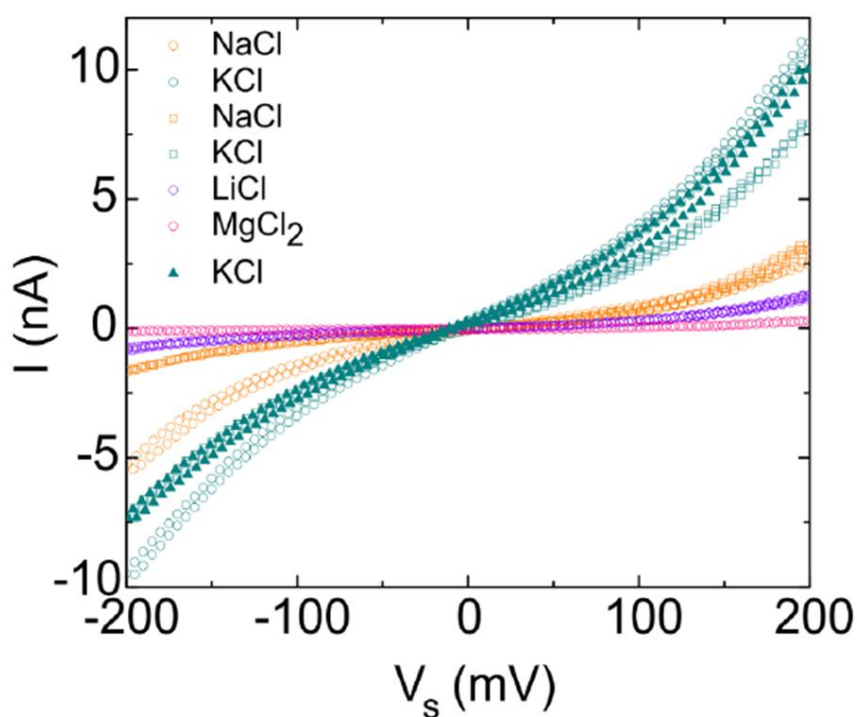


Figure 5.6: Pore conductance for device CVD-11 displaying cation selectivity at 0.1M Cl^- concentration. Electrolyte solutions were measured in the order listed in the legend. This order does not correlate with ion size or hydration energy and alternates back and forth between solutions.

from the air. To change the electrolyte solution, the microfluidic cell was first flushed with deionized water for 8 minutes, and then the new electrolyte was introduced. To ensure the observed selectivity was not an artifact of switching between solutions, the order in which different salt solutions were measured was varied, and we repeatedly alternated back and forth between salt solutions to confirm the differences in conductance were stable. An example of this is shown in Figure 5.6. For extended storage, devices were stored in either deionized water or 0.1M KCl at 4° C.

Measurement of conductance across the graphene membrane was carried out by applying a bias voltage across the device and measuring the resulting current (figure 5.1 A). From 0 mV, the voltage was ramped up to 500 mV, down to -500 mV and back to 0 mV. I-V characteristics were measured with a DL Instruments model 1211 current preamplifier with silver/silver chloride electrodes at a sampling speed ranging from 1 – 10 mV/s. A schematic diagram of the equivalent sensing circuit is shown in Figure 5.7. Conductance values were calculated by taking a linear fit of the I-V curve for +/- 50 mV around $V_s = 0$ mV.

Conductance measurements were carried out in five different electrolyte solutions (KCl, NaCl, LiCl, CaCl₂, MgCl₂) and at different concentrations ranging from 1 M down to 10⁻⁷ M. In order to measure selectivity, the concentrations used to measure conductance were chosen to maintain a consistent Cl⁻ ion concentration across experiments comparing both monovalent and divalent ions; for example 100 mM concentration for monovalent ions and 50 mM concentration for divalent ions. This ensured that differences in conductance were due to differences in ion mobility and not from differences in bulk

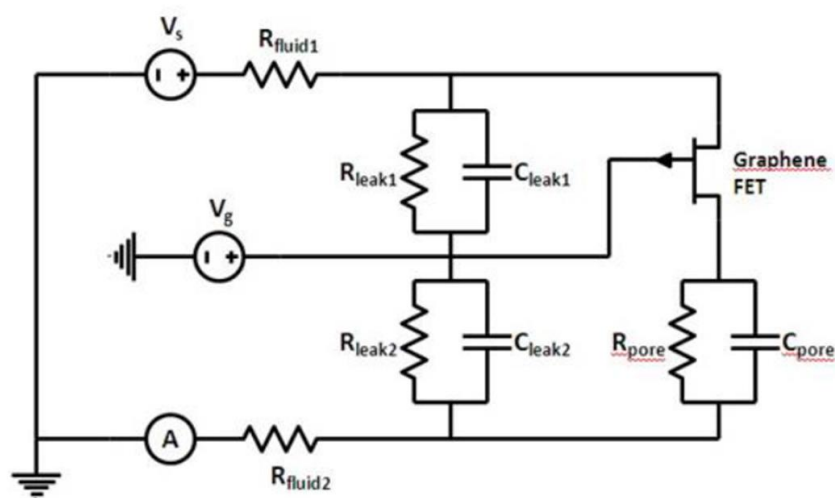


Figure 5.7: Equivalent circuit diagram for graphene nanopore device mounted in the experimental set up. Due to asymmetries in the device and microfluidic cell, the solution resistance, leakage resistance and leakage capacitance are not necessarily the same on either side of the membrane, hence the subscripts 1 and 2.

Concentration	KCl (mS/cm)	NaCl (mS/cm)	LiCl (mS/cm)	CaCl ₂ (mS/cm)	MgCl ₂ (mS/cm)	Di H ₂ O (μ S/cm)
1 M	116.9	95.1	75.8	-	-	-
500 mM	-	-	-	85.1	-	-
100 mM	14.83	11.75	10.66	-	-	-
50 mM	-	-	-	11.36	10.41	-
10 mM	1.686	1.212	1.053	-	-	-
5 mM	-	-	-	1.285	-	-
1 mM	0.203	0.1193	0.1327	-	-	-
500 μ M	-	-	-	0.1328	-	-
100 μ M	0.01123	0.01539	0.01502	-	-	-
50 μ M	-	-	-	0.01611	-	-
10 ⁻⁷ M	-	-	-	-	-	4.40

Table 5.2: Measured bulk conductivities of electrolyte solutions used in this study.

conductivity. The bulk conductivities of the solutions used in this study were confirmed using Mettler Toledo S230 SevenCompact™ conductivity meter with InLab® 731 ISM probe for concentrations $\geq 10^{-2}$ M and InLab® 741 ISM probe for concentrations $< 10^{-2}$ M. Values for bulk conductivity are shown in table 5.2.

The application of a gate voltage could also be applied to the graphene while sweeping the bias voltage across the device. As mentioned in chapter 3, while applying a gate voltage to the graphene membrane it is possible for electrochemical processes to take place where graphene is exposed to solution. Literature has demonstrated the graphene basal plane to be quite stable in monovalent and divalent salt solutions at low voltages, while graphene edge sites are shown to be significantly more reactive than the basal plane (Banerjee, et al., 2013; Li, et al., 2011; Yuan, et al., 2013; Valota, et al., 2011). While electrochemical effects are a consideration, leakage current between the source/drain and the gate were measured with various concentrations of KCl solution to ensure the leakage current was well below the measured pore conductance. This is shown in figure 5.8 for device EXF-1. Gating behavior was measured when sweeping the bias voltage and holding the gate voltage constant, as well as when sweeping the gate voltage and holding the bias voltage constant.

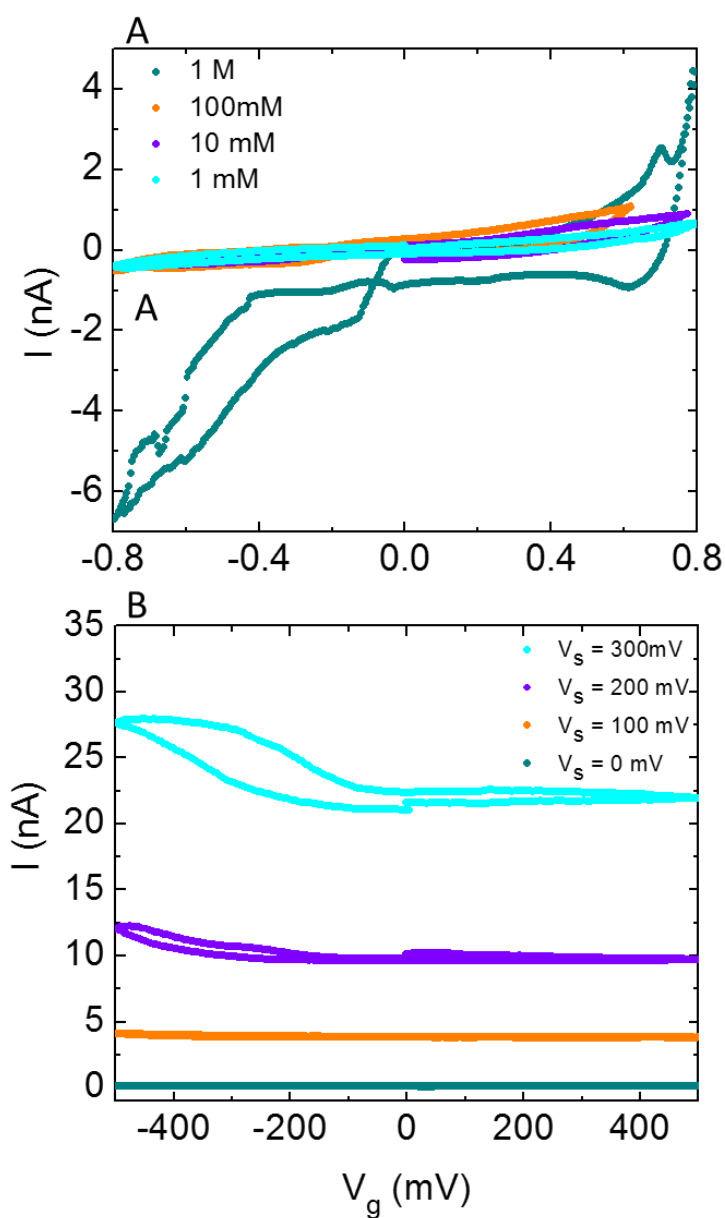


Figure 5.8: (A) Leakage current in device EXF-1 from gate to drain, with the source floating, for different concentrations of KCl. (B) I-V curves for device EXF-1 in 0.1M KCl with the gate swept from -500 mV to 500 mV under source voltages ranging from 0 mV to 300 mV.

Several control experiments were carried out to verify that the measured current was passing through the graphene pore(s) and not leaking through the graphene/silicon nitride interface or elsewhere (figure 5.9). The following control devices were measured:

- (1) ALD alumina coated silicon nitride membrane with no through-hole, no graphene. Isolate transport through silicon nitride membrane and through the PDMS sealing device within microfluidic cell.
- (2) ALD alumina coated silicon nitride membrane with 5 μm through-hole, no graphene. Determine limiting conductance for nitride through-hole.
- (3) ALD alumina coated silicon nitride membrane with 5 μm through-hole, suspended unperforated CVD graphene.
- (4) ALD alumina coated silicon nitride membranes with 5 μm through-hole, suspended single layer exfoliated graphene not exposed to oxidation. Isolate transport through graphene/silicon nitride interface.
- (5) ALD alumina coated silicon nitride membrane with 5 μm through-hole, thick suspended exfoliated graphene (10+ layers) exposed to oxidation. Thick devices ensure that defects introduced do not produce any pores spanning across the graphene membrane. Isolate transport through graphene/silicon nitride interface and determine if oxidation process changes transport through graphene/silicon nitride interface.

Leakage conductance was measured to be less than 55 pS in 0.1 M KCl and less than 140 pS in 1.0 M KCl for type (1) control devices. The limiting conductance through type (2) control devices was measured to be on the order of μS for 0.1 M KCl. For type (3) and type

(4) control devices, conductance was less than 60 pS in 0.1 M KCl and less than 280 pS in 1.0 M KCl. Four type (5) control devices were tested. Three of the four type (5) devices displayed leakage current less than 150 pS in both 0.1M KCl and 1.0M KCl. One type (5) device displayed appreciable leakage current, however this device exhibited behavior significantly different from the porous graphene devices that will be described in section 5.3. This device showed highly rectified behavior, current was unstable, and the device did not exhibit the selectivity nor the gating response observed in the porous graphene devices (figure 5.10). The likelihood of leakage through the graphene/silicon nitride interface in oxidized graphene devices varies from one device to the next and is dependent on the adhesion of the graphene to the silicon nitride surface. While we cannot rule out leakage current through the graphene/silicon nitride interface contributing to the overall conductance, from these controls we can conclude that the stable, selective, gating behavior observed below in section 5.3 is not a result of transport through the interface.

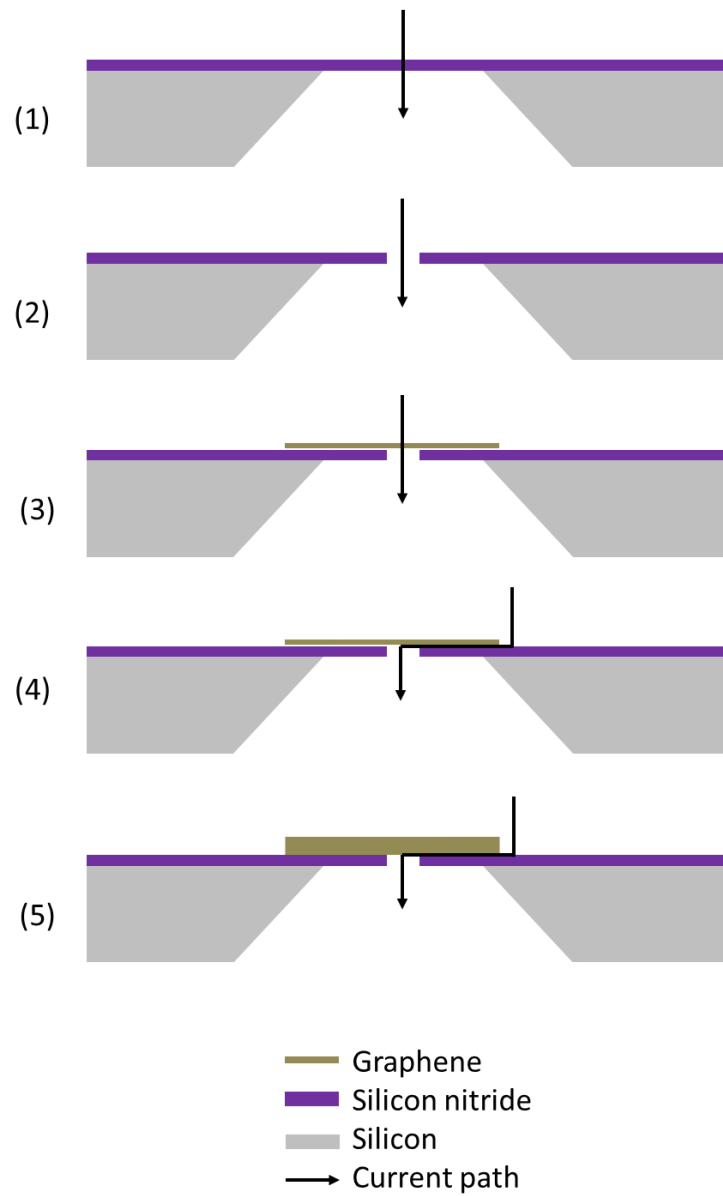


Figure 5.9: Illustration of control devices and leakage pathways measured, corresponding to the five types of devices listed above.

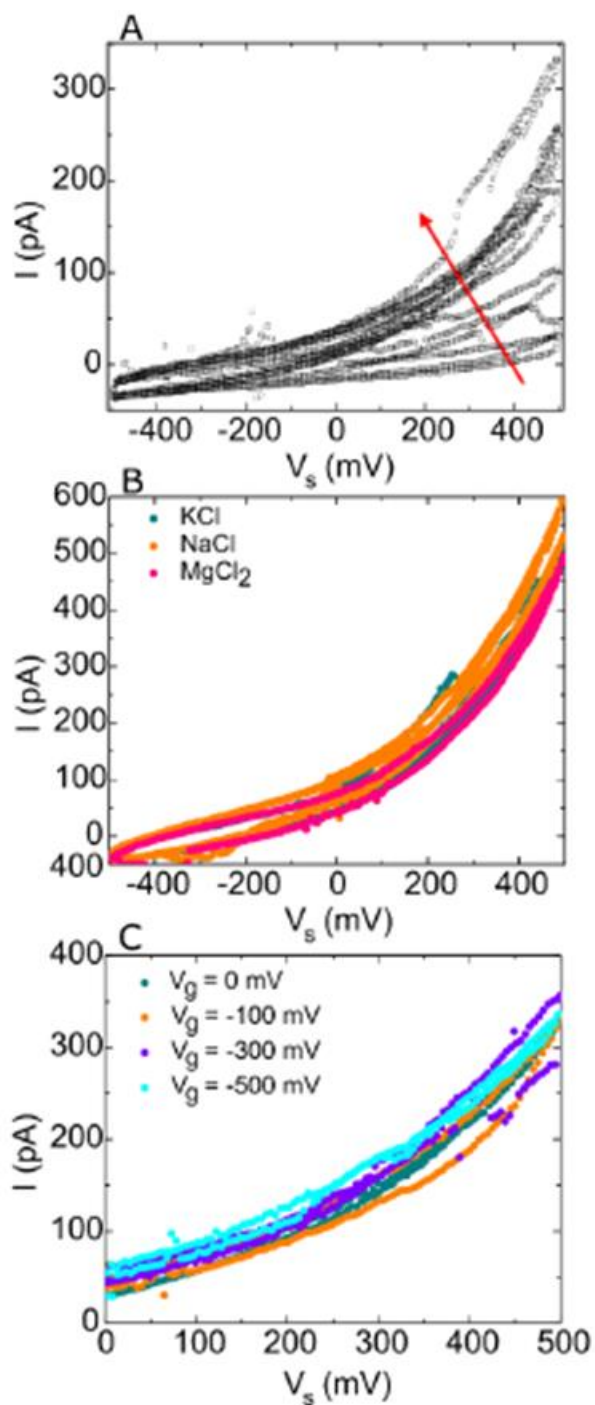


Figure 5.10: I-V behavior from a singular abnormal control device. One type (5) control device exhibited (A) unstable pore conductance in 0.1 M KCl (arrow indicates increasing time) and (B) non-selective I-V behavior in electrolyte solutions at 0.1M Cl^- concentration. (C) Gating behavior in 0.1M KCl under gate voltages ranging from 0 mV to -500 mV.

5.3: Graphene nanopore conductance: activated I-V characteristics, inter-cation selectivity and gate response

Ionic conductance was first measured in the two-terminal configuration across each device, with the gate terminal floating. For the exfoliated graphene device (EXF1), linear I-V characteristics were observed for KCl; however, non-linear (activated) I-V characteristics were seen using NaCl and LiCl as the electrolyte (figure 5.11a). Similar activated and highly selective behavior was observed in the CVD graphene sample with nine approximately 35 nm pores, device CVD-6 (figure 5.11c). Although more pronounced, the activated I-V behavior seen in this device is analogous to that displayed by NaCl and LiCl in device EXF-1.

To account for the differences in bulk conductivity, we plot the normalized conductance for each cation-chloride solution

$$g_i = \frac{G_i}{\sigma_i/\sigma_{KCl}} \quad (5.1)$$

where G_i is the measured nanopore conductance in solution i , σ_i is the bulk conductivity of solution i and σ_{KCl} is the bulk conductivity of KCl at a comparable Cl^- concentration (table 5.2). The normalized conductance reveals the pore(s) to be highly cation selective, with significant preference for K^+ over other cations measured (figure 5.12). For $V_s = 0$ mV, the normalized conductance of KCl was approximately four times greater than NaCl, six times greater than LiCl, and approximately 100 times greater than the divalent ions measured. The absence of conductivity in $CaCl_2$ and $MgCl_2$ suggests that cations are the dominant charge carriers.

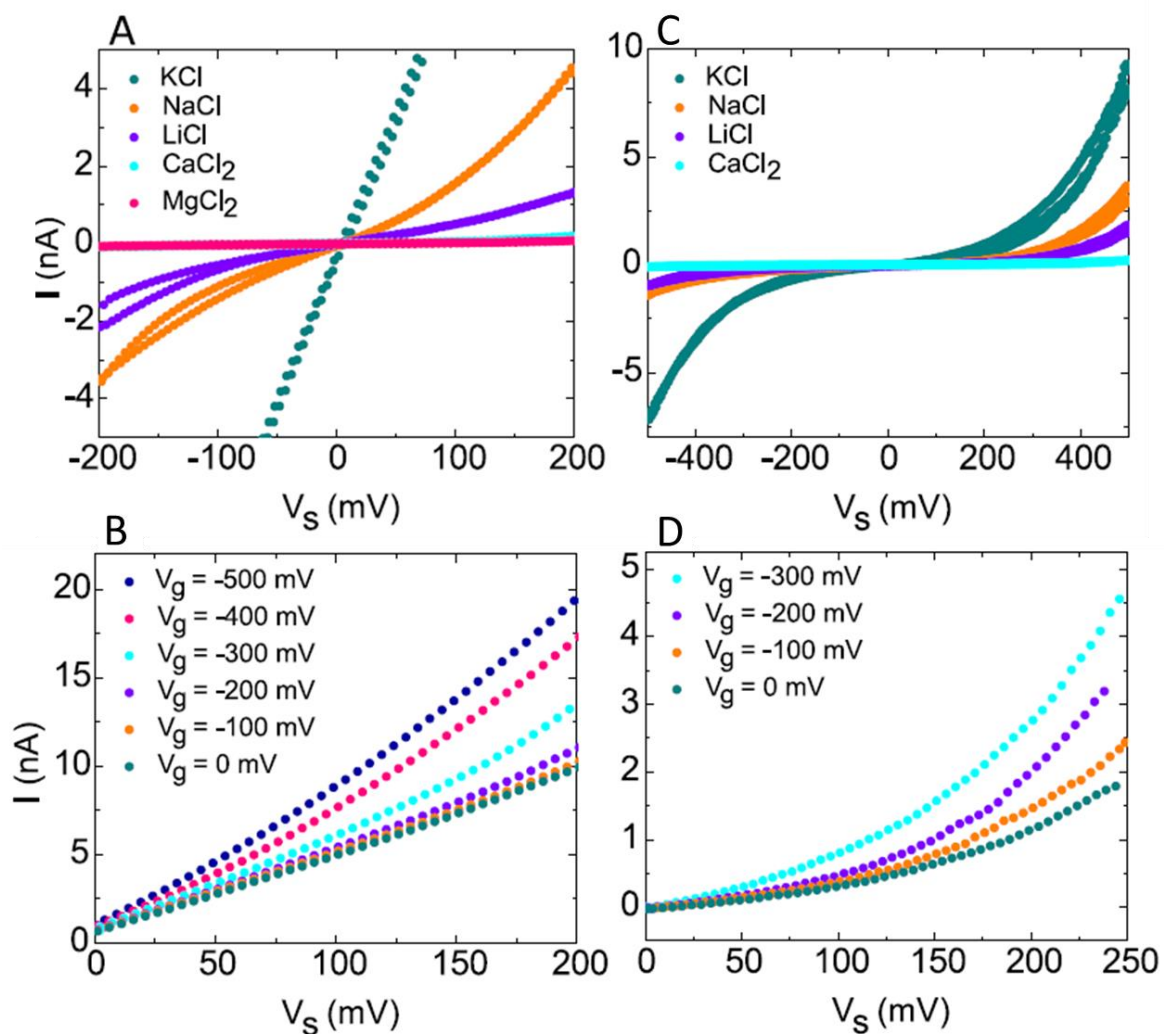


Figure 5.11: I-V curves for (A) device EXF-1 and (B) device CVD-6. Gating behavior for (C) device EXF-1 and (D) device CVD-6. All solutions are at 0.1M Cl^- concentration.

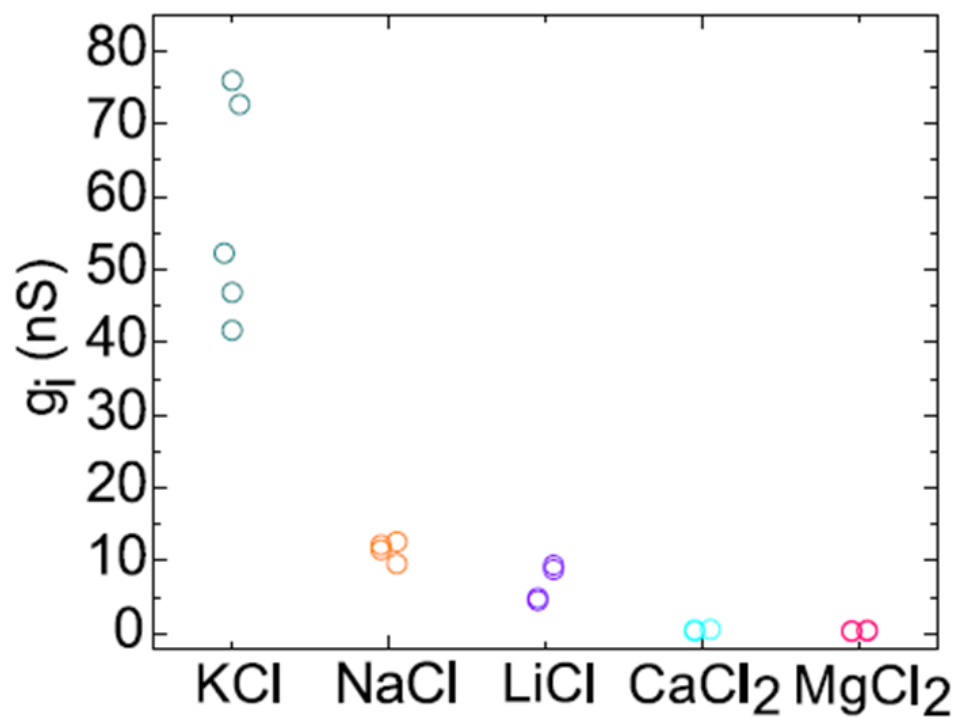


Figure 5.12: Normalized conductance across porous graphene device EXF-1. Conductance taken at $V_s = 0$ mV. All solutions are at 0.1 M Cl^- concentration.

Next, a gate voltage was applied to the graphene to modulate the ionic current. Figure 5.11B, D demonstrate the ionic current response to changes in the gate voltage. As a more negative gate voltage is applied, the ionic current increased. As positive gate voltage is applied, there was no significant change in the ionic conductivity. This unipolar behavior is similar to a p-type FET device, again suggesting that cations are the majority charge carriers; consistent with 2 terminal measurements (Fan, et al., 2008; Nam, et al., 2009; Karnik, et al., 2005). Gating behavior was observed in device EXF-1 for KCl solutions ranging from 1 mM to 1 M concentration.

To characterize the cation selectivity of a device, we define the selectivity ratio as $S_i = g_i/g_{KCl}$. This definition gives a selectivity ratio of 1 for a pore that does not distinguish between cation i and K^+ . Of the 14 porous graphene devices measured, the reported nonlinear I-V behavior accompanied by high selectivity, which we defined as $S_i < 0.5$, was observed in eight devices (figure 5.13, table 5.1). Devices with a pore greater than 100 nm in diameter (CVD-12, CVD-13) displayed linear I-V characteristics and did not show cation selective behavior.

Pores remained fairly stable over the course of experiments (figure 5.14A–C). A measured device could be stored for several weeks in deionized water and after reintroducing electrolyte, still produced behavior similar to the original I-V curves. However, after gated measurements select devices did exhibit a long recovery time, taking several hours to days for the device to return to its initial conductance state. Additionally, applying too large of a gate voltage caused an irreversible increase in the transmembrane conductance. While the selectivity of most pores remained stable, the degree of selectivity

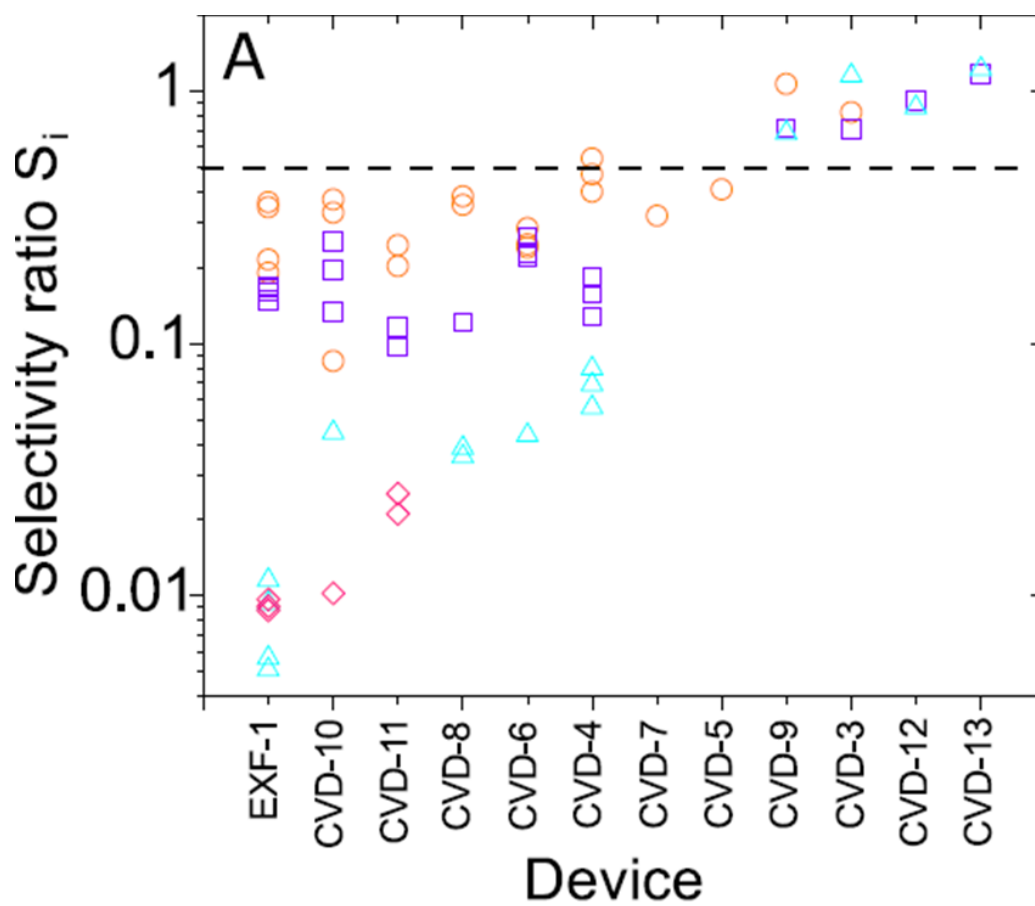


Figure 5.13: Selectivity ratio S_{Na} (orange), S_{Li} (purple), S_{Ca} (Cyan) and S_{Mg} (pink) for the 14 porous graphene devices measured in this study, ordered according to selectivity. The dotted line indicates a selectivity ratio of 0.5. Device CVD-1 and CVD-2 did not have appreciable conductance, thus a selectivity ratio was not measured. See table 4.1 for details on specific devices.

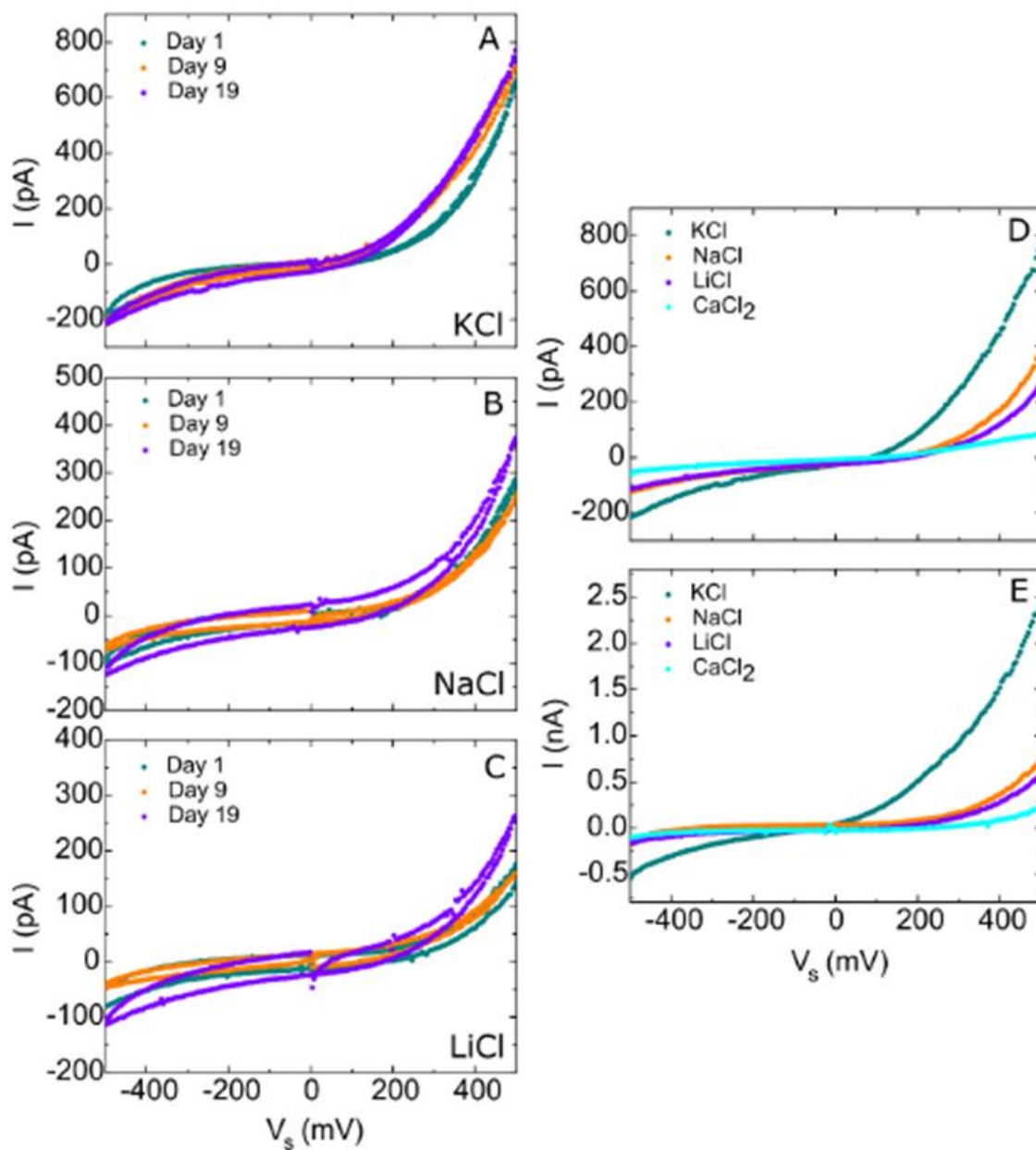


Figure 5.14: (A–C) Pore conductance for device CVD-10 in 0.1M KCl, 0.1M NaCl and 0.1M LiCl solutions, measured periodically over 19 days. (D–E) depict the pore conductance (V_g =float) for device CVD-10 in 0.1 M Cl⁻ concentration on (D) Day 19 and (E) after extended exposure to V_g = -500 mV in 0.1M NaCl on Day 67. Selective behavior remained while overall conductance and degree of selectivity increased.

in device EXF-1 and CVD-10 did vary, correlating with changes in the pore conductance over time. (figure 5.14D, E).

For the subset of devices containing HIM drilled pores, we measured the conductance of various ions for individual pores with an imaged diameter ranging from 23 nm – 250 nm. The conductance for devices with multiple pores were normalized to a single pore by dividing the total conductance by the number of pores in the device. We observe a linear increase in conductance and corresponding decrease in selectivity vs. pore diameter, which is in qualitative agreement with equation 4.7 for the case of $d \gg l$ (figure 5.15). However, experimentally measured conductance values are significantly lower than what is predicted by equation 4.7, using the measured bulk conductivity (table 5.2). For the largest imaged pore ($d = 245$ nm), the measured conductance is approximately 10 times less than what would be predicted by equation 4.7.

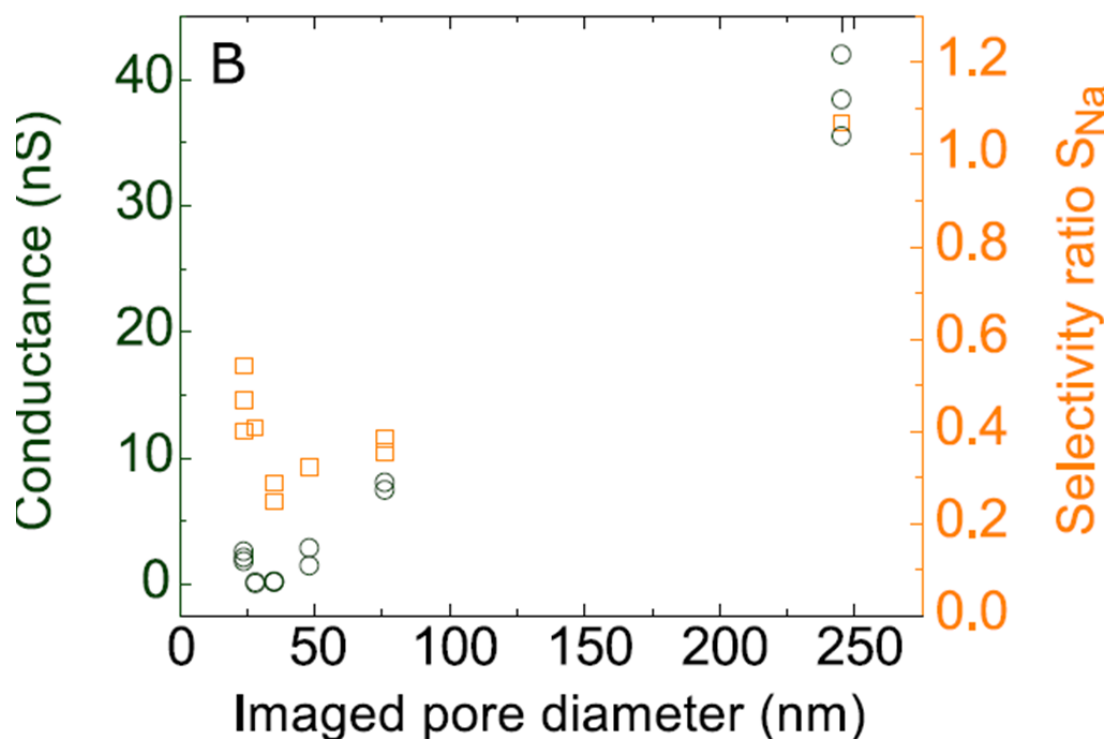


Figure 5.15: Conductance (open circles) in 0.1 M KCl and corresponding sodium selectivity ratio (S_{Na}) for devices with HIM drilled pores.

5.4: Cation-anion selectivity

The absence of conductivity using CaCl_2 and MgCl_2 solutions along with the unipolar gate response suggests that the dominant charge carriers are cations. To further confirm that cations are indeed the majority charge carriers, two experiments were conducted: (i) conductance measurements with asymmetric ion concentrations and (ii) conductance measurements with asymmetric ion conditions.

For the first experiment, with asymmetric ion concentrations, I-V curves were measured with several different concentration gradients across the pore (figure 5.16). KCl solutions were used because K^+ and Cl^- have similar bulk mobilities, removing the effects of a liquid junction potential. When there is no bias voltage applied, both K^+ and Cl^- ions will diffuse from the higher concentration to the lower concentration reservoir. A net current is produced only if one ion diffuses faster than the other. In figure 5.16, at $V_s = 0$, the zero-bias current becomes more negative as the concentration gradient increases. The direction of the current offset is consistent with a net flow of cations from high to low concentration. This is an indication that the pore is cation selective. A more quantitative measure of the ion selectivity is to use the reversal potential, the applied bias voltage at which the net current is zero.

The Goldman-Hodgkin-Katz (GHK) voltage equation relates the reversal potential to the ion concentration and the permeability of the membrane to a given ion species. It is derived from the Nernst-Planck equation, which describes the flux across the membrane as determined by the concentration gradient and the applied electric field. If one assumes that the ions act independently and that the potential drop across the membrane is linear, then

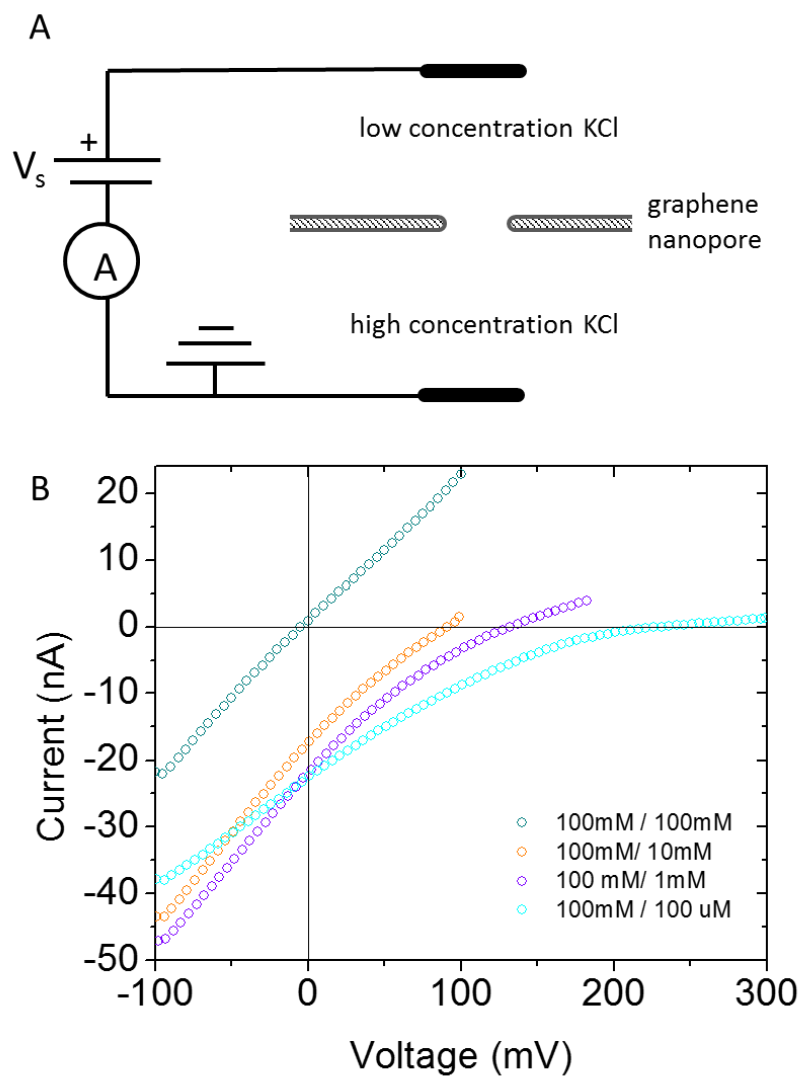


Figure 5.16: (A) Schematic of reversal potential measurements. A concentration gradient and electric potential are simultaneously imposed across the nanopore and I-V behavior is measured. (B) The resulting I-V curves for several concentration gradients, indicated in the legend.

one will arrive at the GHK equation from Nernst-Planck (Hille, 2001). The GHK voltage equation for a solution with only KCl is written as

$$V_{rev} = \frac{k_B T}{e} \ln \left(\frac{P_K c_{high} + P_{Cl} c_{low}}{P_K c_{low} + P_{Cl} c_{high}} \right) \quad (5.2)$$

Where c_{high} and c_{low} are the solution concentrations on either side of the membrane, and P_K and P_{Cl} are the relative permeabilities of each ion. The relative permeability of an ion depends on its diffusion coefficient and partition coefficient. In this context, the selectivity ratio, S_{GHK} can be defined as the ratio of permittivities, P_K/P_{Cl} , thus the GHK equation can be rewritten as

$$V_{rev} = \frac{k_B T}{e} \ln \left(\frac{S_{GHK} + \frac{c_{low}}{c_{high}}}{S_{GHK} \frac{c_{low}}{c_{high}} + 1} \right) \quad (5.3)$$

Plotting the reversal potential against $\frac{c_{low}}{c_{high}}$, and carrying out a least squares fit to solve for S_{GHK} , this device shows over a two order of magnitude preference for K^+ over Cl^- . The potential across the membrane was adjusted for the electrodes' redox potential using the Nernst equation. Highly cation selective behavior in graphene nanopores has also been observed in recent studies done by (Rollings, et al., 2016) and (Walker, et al., 2017).

In the second experiment, I-V curves were measured with one reservoir containing 50 mM $CaCl_2$ solution while the opposing reservoir contained 100 mM of KCl. Concentrations were chosen to maintain a constant Cl^- concentration. In this configuration, we observed highly rectified behavior (figure 5.17B, C). Since the Cl^- concentration on either side of the membrane is the same, the rectified behavior demonstrates that the pores are indeed selective to cations, eliminating the distinct possibility that the current may be

carried by anions but modulated by cations. The strong rectification is a result of Ca^{2+} having a much lower permeance across the membrane than K^+ , consistent with the observations in section 5.3. Both experiment (i) and (ii) confirm the conclusion that cations are the majority charge carriers.

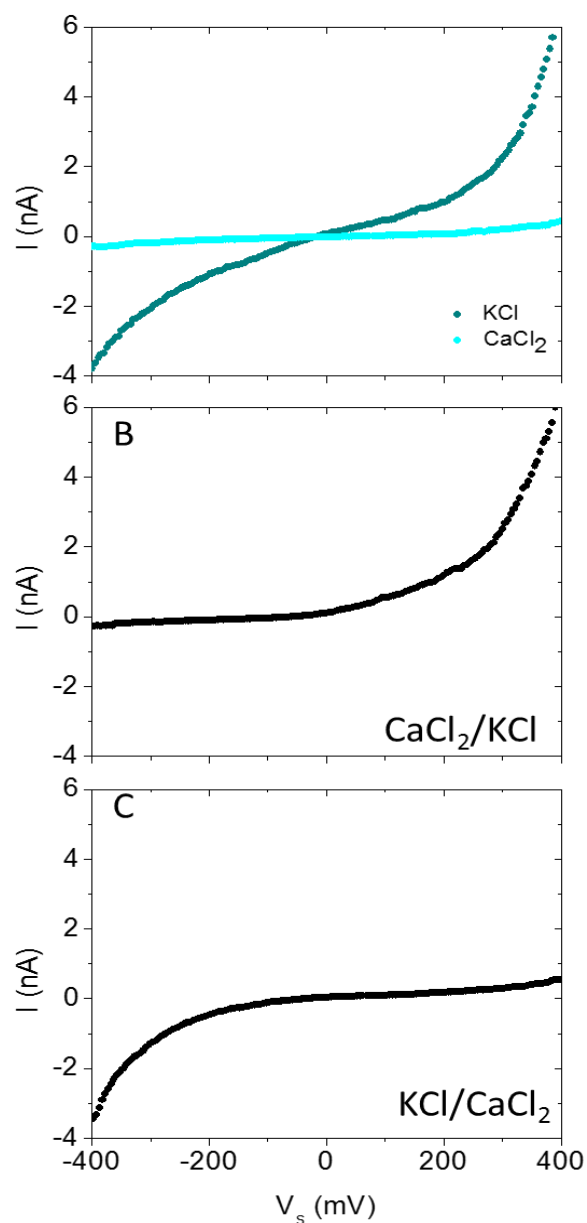


Figure 5.17: (A) Symmetric ion conditions for both KCl and CaCl₂ at 0.1 M Cl⁻ concentration. (B–C) Asymmetric ion conditions in 0.1 M Cl⁻ concentration, with (B) KCl on the source side of the membrane and (C) CaCl₂ on the source side of the membrane.

5.5: Concentration and pH dependence

To better understand the observed selective behavior and gate response, we measured the conductance across ion selective device CVD-10 in electrolyte solutions with concentrations ranging from 1M to 10^{-7} M. Non-linear I-V behavior remained at all concentrations measured (figure 5.18A). For the three different electrolytes measured, bulk behavior dominates at high concentrations, while at low concentrations the behavior deviates from bulk and plateaus to a surface charge governed regime (Venkatesan, et al., 2012; Shan, et al., 2013) (figure 5.18B). The plateaus occur at a similar conductance which would indicate that the surface charge on the graphene is constant across the different electrolyte solutions. In the bulk regime however, the conductance increases with concentration and maintains ion selectivity greater than expected given bulk ion mobility (figure 5.18B).

In addition to concentration dependence, pH dependence was also explored. I-V curves were measured in symmetric conditions of 0.1M KCl solutions with varying pH. If the graphene surface was negatively charged with deprotonable oxygen-containing species (-OH groups), then the surface charge would be negative at neutral pH values and neutralized in acidic solutions, causing the conductance at lower pH values to be greater than at higher pH values (Rollings, et al., 2016). The conductance shown in figure 5.19 looks to demonstrate this effect, where the conductance is observed to increase with increasing pH (figure 5.19). The large negative surface charge would attract a high concentration of cations near the surface compared to anions, contributing to a large cation-selective current. This is consistent with the results presented in section 5.4.

Additionally, both the pH and concentration dependence observed in our graphene nanopore devices were different from that observed by (Feng, et al., 2016) in MoS₂ nanopores, thus eliminating ionic Coulomb blockade as the explanation of activated I-V characteristics.

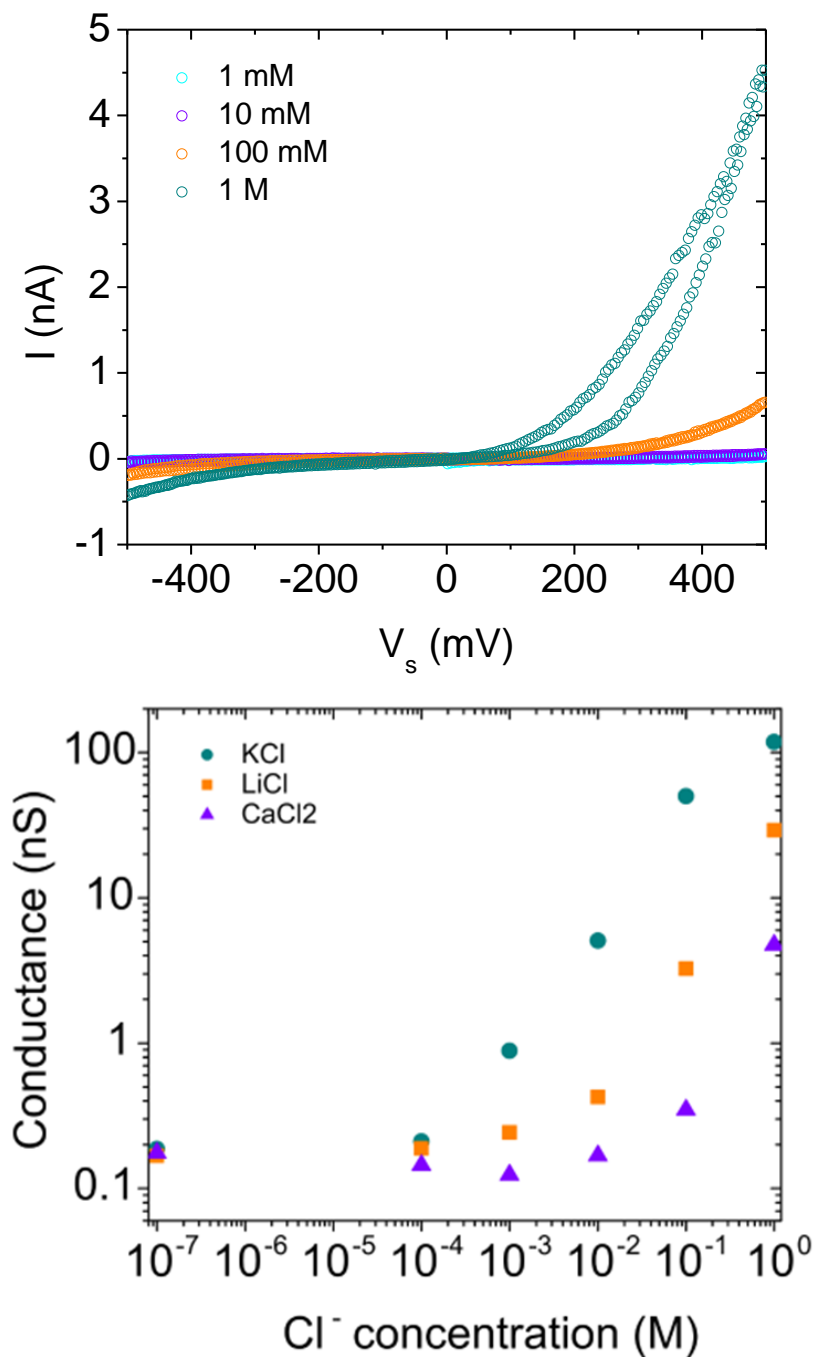


Figure 5.18 (A) Pore conductance across device CVD-10 in KCl solutions of varying concentration. Measured on Day 19. Non-linear, activated I-V behavior remains across varying concentrations, however ‘activation voltage’ is lower as the concentration increases. (B) Measured pore conductance at $V_s = 0$ mV as a function of electrolyte concentration for device CVD-10. Measured on Day 85. Deionized water was measured to give the data points at 10^{-7} M.

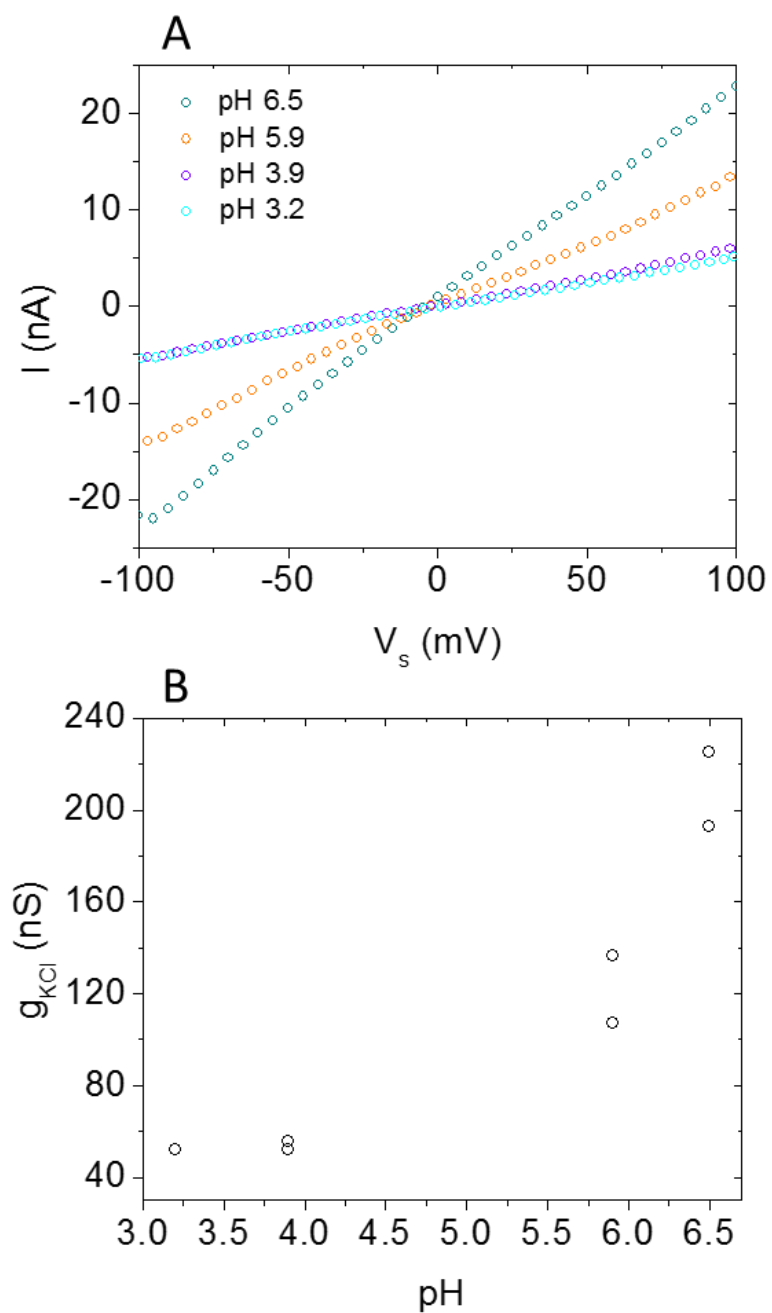


Figure 5.19: (A) I-V curves measured across graphene nanopore in 0.1M KCl solutions with varying pH. (B) Conductance plotted against pH conditions. The conductance is observed to monotonically increase with increasing pH, different than the pH dependence witnessed in MoS₂ nanopores displaying ionic Coulomb blockade (Feng, et al., 2016).

5.6: Understanding the mechanism for selectivity and gate response

The observed selectivity and activated I-V behavior in figure 5.11 scale with the trend in hydration energy among the measured cations: $K^+ > Na^+ > Li^+ > Ca^+ > Mg^+$ (Hille, 2001), where cations with the largest measured conductance have the lowest hydration energy. This suggests that dehydration may play a role in the observed ion selective behavior. Additionally, the ability to detect a direct electrostatic gating response is dependent on the Debye screening length (~ 1 nm and ~ 0.3 nm in 0.1 M and 1M KCl, respectively). Selective, gate responsive devices were observed to have a gate response in KCl solutions up to 1 M concentration. These results suggest a steric exclusion mechanism, similar to that outlined in section 4.2, where activated and selective behavior can result from a pore on the same order of size as the translocating ion. However, from extensive STEM imaging, it is clear our pores are much larger than what would be required for steric exclusion to occur. The experiments carried out in sections 5.4 and 5.5 confirm cation over anion selectivity, suggesting negative surface charge plays a role in the governing transport mechanism. However, charge alone cannot account for inter-cation selectivity between monovalent ions.

The low conductance in the measured devices suggests an additional barrier to transport. It is well known that airborne hydrocarbons quickly adsorb onto a graphene surface when exposed to ambient conditions (Li, et al., 2013). This drastically alters the surface energy of the graphene film and consequently the hydrophobicity (Kozbial, et al., 2014). This has been observed in DNA translocation experiments using graphene nanopores, where it is common to apply a post-perforation treatment, directly before

experimentation, to increase wettability of the graphene surface and to prevent clogging of the pore (Venkatesan, et al., 2012; Merchant, et al., 2010; Schneider, et al., 2013; Shan, et al., 2013). This treatment often takes the form of oxygen plasma or UV/Ozone exposure. While UVO treatment can etch and remove adsorbed hydrocarbons, it can also etch the graphene itself, potentially introducing new pores or enlarging existing pores before hydrocarbons are completely removed (Liu, et al., 2008; Koenig, et al., 2012).

To confirm that hydrocarbon surface adsorbates play a role in governing the observed behavior, we measured the conductance and selectivity through single pores in h-BN, which has a high oxidation resistance and can withstand UVO treatment without being etched (Chen, et al., 2004; Zhou, et al., 2013). Two h-BN devices were fabricated in the same way as exfoliated graphene devices and a single pore was introduced into each device via HIM drilling. Upon initial measurements of the device, the pore conductance was well below what would be predicted by equation 4.7 given the imaged pore size. After incremental exposure to UVO treatment, the conductance increased gradually and then plateaued (figure 5.20). The ion selectivity was measured for the h-BN device shown in figure 5.20B at time $t = 4$ minutes and $t = 13$ minutes. The corresponding I-V curves are shown in figure 5.20C and D, respectively.

Analogous to the graphene devices, selective, non-linear I-V behavior was observed in the h-BN devices when the pore conductance was low. After hydrocarbon adsorbates were removed via UVO treatment, the devices displayed linear I-V behavior, more consistent with the imaged pore size (figure 5.20B, D). Utilizing h-BN instead of

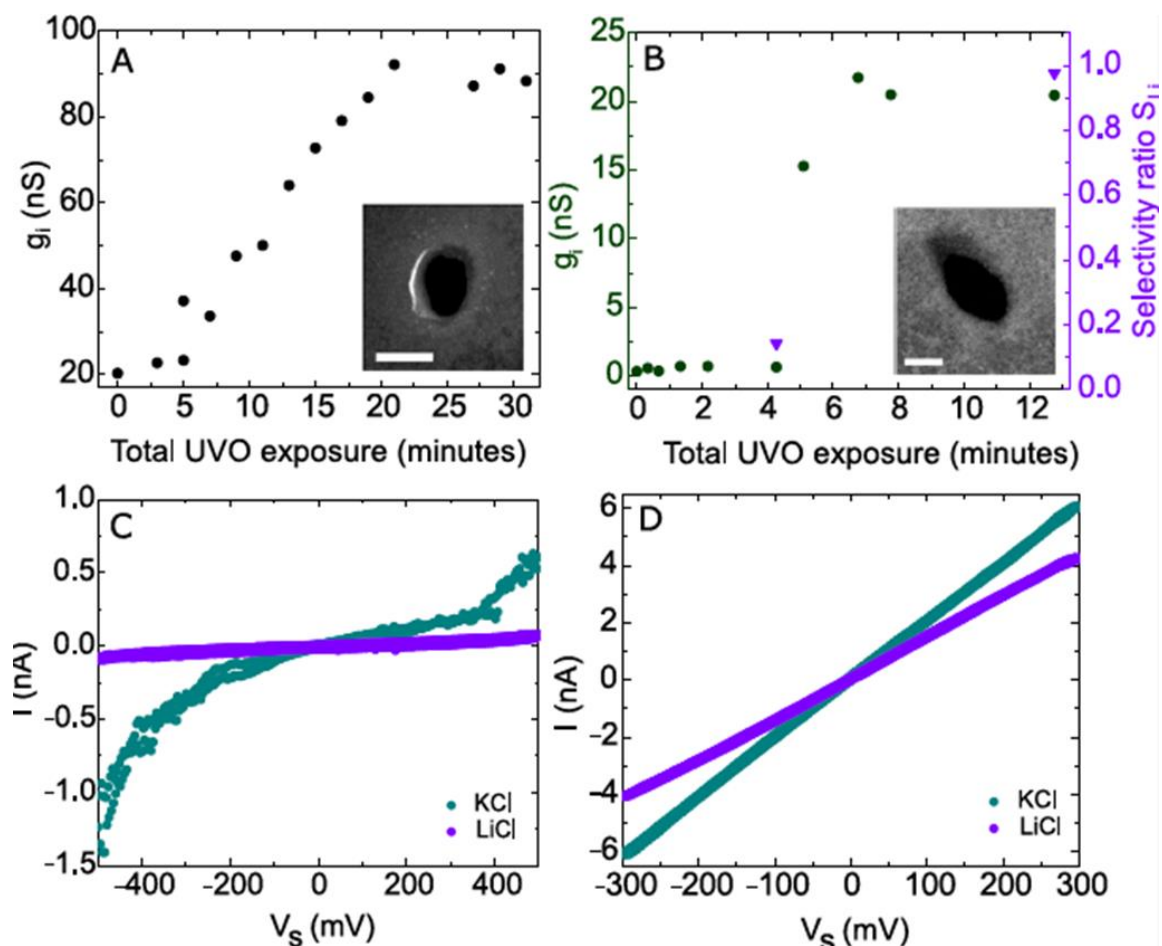


Figure 5.20: Changes in conductance (solid circles) in response to UVO treatment for (A) device HBN-1, with an approximately 80 nm diameter pore, and (B) device HBN-2, with an approximately 30 nm diameter pore. Insets depict MAADF STEM images of respective pores prior to UVO treatment. Scale bars (A) 100 nm, (B) 20 nm. I-V curves for device HBN-2 at (C) $t = 4$ minutes and (D) $t = 13$ minutes. Selectivity ratios (solid triangles) in (B) are calculated from I-V curves in (C) and (D). Conductance is measured in 0.1M Cl⁻ solutions.

graphene ensures that we are not introducing new pores and only removing surface adsorbates with the UVO treatment.

While hydrocarbon adsorbates play a role in the governing mechanism, the above experiment is indistinct about whether hydrocarbon adsorbates create a physical barrier within the pore or that their presence on the surface modifies the surface energy such that it is unfavorable for the pore to wet. To address this, the pore conductance of a graphene device was measured in a 0.1 M aqueous LiCl solution as well as a 0.1 M ethanol based LiCl solution. While the concentration of the solute is the same for both solutions, the solvents differ in their surface energies, $\gamma_{water-air} = 72.86 \frac{mJ}{m^2}$, $\gamma_{ethanol-air} = 22.39 \frac{mJ}{m^2}$ (Adamson & Gast, 1997; Pallas & Harrison, 1990), and bulk conductivities, measured to be 10.66 mS/cm and 1.543 mS/cm for 0.1 M LiCl in water and 0.1 M LiCl in ethanol, respectively.

Figure 5.21 shows the I-V behavior for aqueous and ethanol based LiCl solutions across a graphene device. We observe a large, linear conductance for the ethanol based solution, while the conductance in the aqueous solution is minimal. If the pores were fully wet but physically occluded by hydrocarbon adsorbates, then one would expect the pore conductance of the water and ethanol solutions to scale according to their bulk conductivities. However, this is not the case, suggesting that the pores are not physically occluded, but that it is more difficult for the aqueous solution to enter the pore than for the ethanol based solution. Additionally, we observe that the conductance for the ethanol based solution is fairly consistent with the imaged pore size, following equation 4.7.

These results corroborate that the graphene devices in this study have an increased hydrophobicity due to adsorbed hydrocarbons and therefore a de-wetted state within the pore is favorable. This suggests hydrophobic gating as the likely governing mechanism for the observed behavior. Hydrophobic gating can explain how a pore much larger than the translocating ions can still exhibit inter-cation selectivity. Additionally, the activated I-V behavior as well as the gate response are likely a consequence of electro-wetting, where the surface energy, and therefore the wettability of the pore, are modified by the applied voltage.

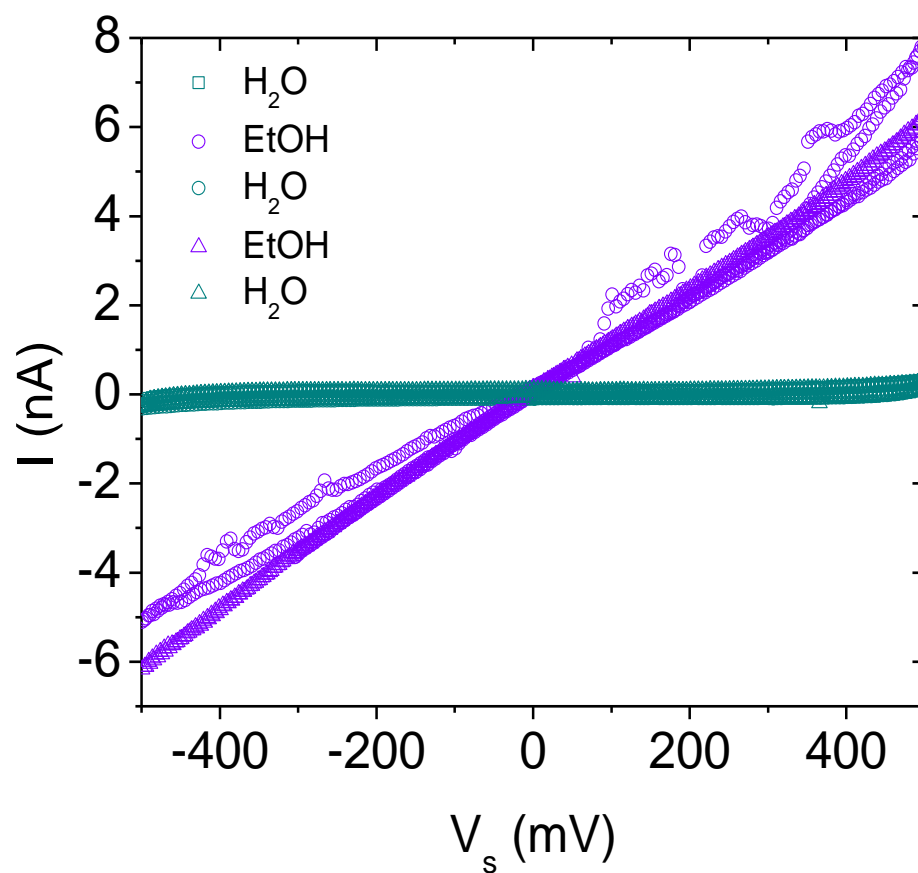


Figure 5.21: I-V curves in aqueous and ethanol based 0.1M LiCl solutions across graphene device containing nine approximately 25 nm pores drilled using the HIM. Measurements were carried out in the order shown in the legend, alternating between the two solutions.

5.7: Conclusions

Nanopores introduced into graphene membranes were shown to demonstrate unparalleled levels of selectivity within a solid state device and conductance through the pores was modulated by an applied gate voltage. Experimental results suggest that hydrophobic gating is a likely governing mechanism for the observed behavior. The next step in this investigation is to explore the details of the mechanism, such as the stability of a vapor gap or air bubble residing in such a low aspect ratio geometry. Nevertheless, this novel demonstration of K^+/Na^+ selectivity and gate responsive behavior within a solid state device is an exciting advancement in separation and sensing technologies, by providing a solid state analog to voltage-gated biological ion channels.

CHAPTER SIX: Towards light responsive MoS₂ nanopores

Since graphene's first isolation, other two dimensional materials have begun to emerge; all with unique mechanical, chemical and optoelectronic properties. One could imagine utilizing this diverse array of two dimensional materials to engineer a tool box of stimuli responsive nanopores, analogous to the plethora of biological ion channels each with unique capabilities. Mechanically responsive pores have been investigated computationally, demonstrating that a pore in MoS₂ can be opened from a closed state when under tensile strain (Li, et al., 2016). Optically gated nanopores have also been investigated. The application of low-power visible light to silicon nitride nanopores was shown to control the charge on the surface of the pore, influencing the ionic conductance and translocation dynamics of DNA and proteins (Fiori, et al., 2013).

MoS₂ is known to have superior optoelectronic properties, making the material a promising candidate to be utilized in the optical control of nanopores (Lopez-Sanchez, et al., 2013). The study outlined in this chapter was carried out to investigate the effect of light on a MoS₂ nanopore operating in an ionic solution.

6.1: Experimental design and preliminary results

MoS₂ was synthesized via CVD using the growth recipe described in (Lloyd, et al., 2016). A powder source of MoS₂ was placed in the central heating zone of the tube furnace (Lindberg Blue) and a SiO₂ substrate was placed in a cooler region downstream. The system was brought down to 10 mTorr and 60 sccm of Ar was allowed to flow as a carrier gas, along with 0.1 sccm of O₂ and 1 sccm of H₂ gas. The furnace was heated to 900°C and held for 15 minutes, after which it was left to cool to room temperature under the flow of

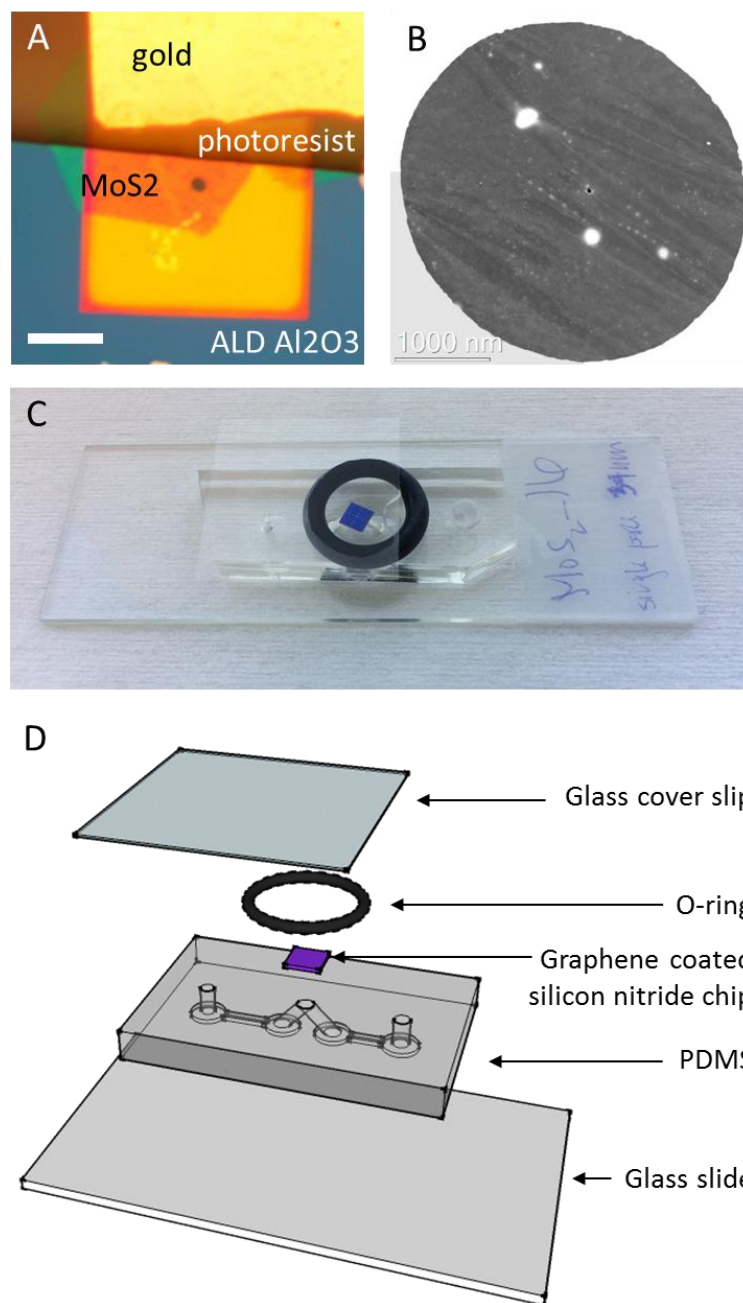


Figure 6.1: (A) Bilayer MoS₂ flake transferred to silicon nitride substrate. The gate electrode is patterned in the same manner as for exfoliated graphene devices fabricated in chapter 5. Scale bar, 30 μm. (B) STEM image of 50 nm HIM drilled pore. (C) Optical image and (D) exploded view of microfluidic cell. The basic device is the same as that described in chapter 5. An additional O-ring and glass cover slip are added to contain the top reservoir of solution and eliminate the water meniscus which can interfere with laser path. (underlying glass slide measures 1" x 3").

gases. In this process, the solid MoS₂ is heated to sublimation and then carried to the cooler region downstream to condense on the SiO₂ substrate. Individual MoS₂ flakes were transferred onto the silicon nitride support chips via the pick-and-place transfer method described in chapter 5, a single approximately 50 nm pore was drilled using the HIM, and the device was mounted into a PDMS microfluidic cell (figure 6.1). The silicon nitride support chips and microfluidic cell used in chapter 5 were also utilized in this study. Additionally, a rubber O-ring and glass coverslip were mounted over the top side of the silicon nitride chip so that the top reservoir of solution did not have a meniscus.

Ag/AgCl electrodes were placed in either reservoir of solution and a bias voltage was applied across the device. The pore conductance was measured in a 0.1 M KCl solution using the electrical setup described in chapter 5, sweeping the bias voltage to +/- 500 mV. Next, the pore current was measured as a function of laser exposure. A schematic of the optical measurement set up is shown in figure 6.2A. A blue diode laser (405 nm) was focused onto the nanopore device with an objective lens (50x). The device was fixed onto a 3-axis micromanipulator stage so that the pore could be aligned with the beam of the laser and a manual shutter was used to control the laser exposure time. Using a patch clamp amplifier (Axopatch 200B), the pore conductance was measured under a fixed voltage bias while the pore was exposed to the laser at ~ 1 μ W of power.

While under laser exposure, the current was observed to increase (Figure 6.2B). After laser exposure, the pore did not instantly return to the previous conductance level. Additional laser exposure continued to increase the current. Intermittently, I-V curves were taken as a measure of the pore conductance (figure 6.2C). These were taken immediately

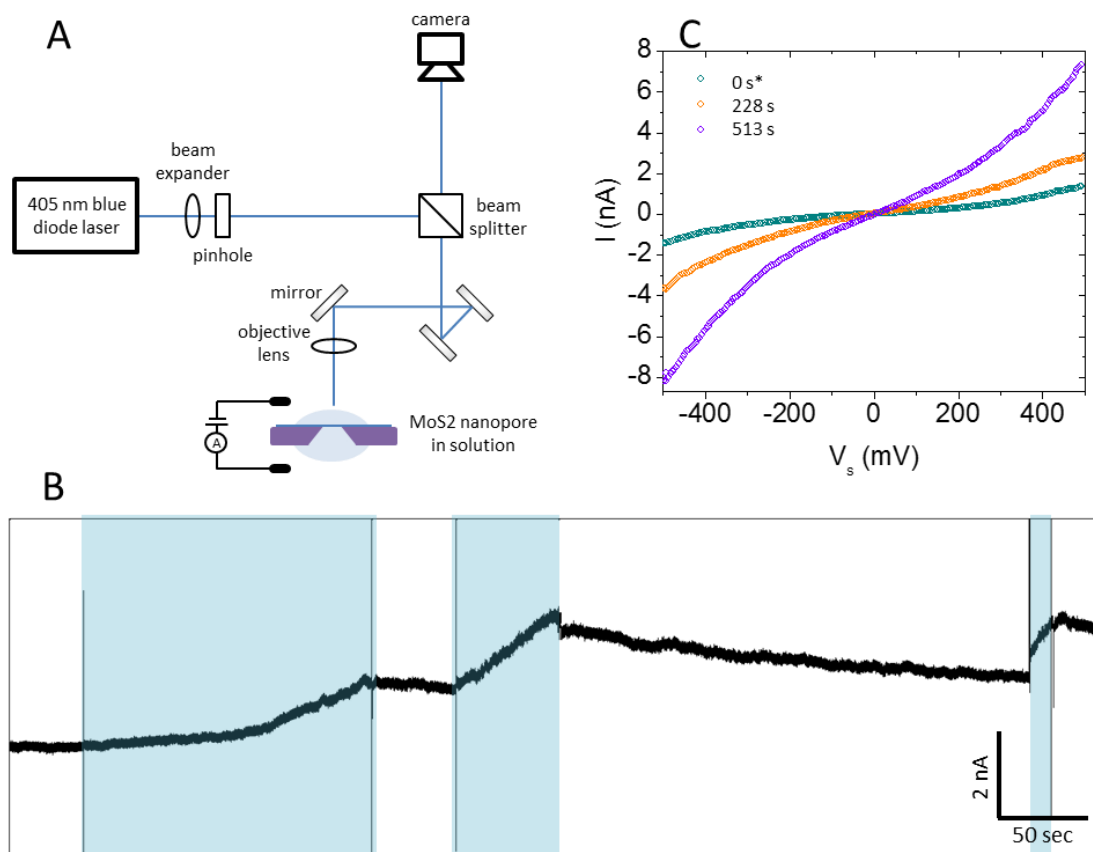


Figure 6.2: (A) Schematic of optical set up. (B) Changes in ionic current over time in response to $\sim 1 \mu\text{W}$ laser exposure in 1 M KCl solution with a fixed bias voltage of 200 mV. Blue regions indicate when laser was on. When pore is exposed to laser illumination the current increases. When the laser is turned off the pore does not instantaneously return to its previous conductance state. (C) I-V curves for the MoS₂ device in 0.1M KCl solution after varying amounts of $\sim 1 \mu\text{W}$ laser exposure. *indicates that device had laser exposure prior to $t = 0$ seconds, however powers were well below $1 \mu\text{W}$.

after laser exposure as well as several hours later, to confirm that the pore conductance was stable at the increased level. Work by (Danda, et al., 2017) reports similar behavior for WS_2 pores exposed to light, which they attribute to physical expansion of the nanopore. It is likely that a similar process is occurring within our MoS_2 nanopores.

Pristine MoS_2 devices without a nanopore, as well as MoS_2 devices perforated via a voltage pulse method (Feng, et al., 2015; T., et al., 2015) were also investigated. These devices also demonstrated an increase in conductance in response to laser exposure. However, in all the devices measured, a range of behaviors were observed, making it difficult to draw concrete conclusions. While it looks to be that MoS_2 pores investigated do respond to laser exposure, at this time we cannot rule out other thermal and chemical effects (Feng, et al., 2015; Chimerel, et al., 2008; Angevine, et al., 2016; Lukowski, et al., 2013).

Several challenges were encountered when investigating MoS_2 nanopores. The quality of the MoS_2 varied between growths, thus often defect density varied from one device to the next. Without extensive STEM imaging on all the devices, this made it difficult to correlate the conductance with a known pore size, as defects may have also been contributing the current. Similarly, for pores created via the voltage-pulse method, it was difficult to determine the number of pores created and their size. The large suspended area (5 μm diameter) makes it likely for multiple pores to have been created. Lastly, non-linear pore conductance and the observation of bubbles likely formed via hydrogen evolution additionally complicate the relationship between pore size and conductance.

6.2: Conclusions

While there is still much to be explored regarding MoS₂ nanopores and their responsiveness to light, this chapter laid the groundwork for those future experiments. A fabrication method for creating MoS₂ nanopores was developed and laser illumination was integrated into the existing experimental set up for measuring nanopore conductance. Preliminary results suggest that pores expand in response to laser exposure, however future studies are still necessary.

CHAPTER SEVEN: Conclusions and future outlook

7.1: Summary

This thesis explored nanoporous two dimensional materials for intelligent control of ionic and molecular transport, analogous to the functionality of a biological ion channel. Chapters 1–4 provided an overview of the field of solid state and two dimensional nanopores, and introduced the basic concepts and theory relevant to the experimental results presented in chapters 5–6.

In chapter 5, we fabricated and characterized cation-selective graphene nanopore devices. These devices displayed considerable K^+/Na^+ selectivity and were responsive to gate voltages up to 500 mV. Cation-anion selectivity, concentration dependence, and pH dependence were also measured. Experiments carried out on h-BN and using ethanol-based solutions suggest that surface charge and hydrophobic gating play a role in governing the observed behavior. These experiments have demonstrated control of ionic transport at an unprecedented level, closely mimicking the capabilities of protein ion channels. Chapter 6 introduced the initial work investigating MoS_2 nanopores and their responsiveness to optical stimuli.

7.2: Future outlook

The studies presented in this thesis have brought to light new and interesting questions regarding nanoporous two dimensional membranes. Our demonstration of a highly cation-selective, solid-state nanopore can motivate the future optimization of solid-state devices, but also inspire further understanding of the mechanisms by which both biological and solid-state devices are governed. Further investigation into the surface

energy and hydrophobicity of two dimensional materials would seem vital for the development of two dimensional nanoporous membrane technologies, given that these materials are all surface. Especially in the case of confined geometries, such as nanopores. There are still many unanswered questions regarding the wettability, capillary effects, and transport through nanoscale pores in two dimensional materials.

In addition to further understanding transport phenomena at the nanoscale, the variety of two dimensional materials provides an interesting set of tools to explore different means by which to control transport. As was pointed out in chapter 6, there is potential for two dimensional nanopores to respond to a variety of environmental stimuli. Work is already being done in this regard, however the field is by no means saturated. The development of a toolbox of two dimensional pores responding to electrical, optical, chemical or mechanical stimulus would allow for configuring lab-on-a-chip technologies with the precise control and sensing of translocating species.

The work presented in the thesis only begins to explore what is possible regarding the control and sensing capabilities of two dimensional nanopores. There are many directions still to pursue within the field, from in depth studies of nanoscale transport mechanisms, to scaling the technology for industrial applications.

BIBLIOGRAPHY

- Adamson, A. W., & Gast, A. P. (1997). *Physical chemistry of surfaces* (6th ed.). Wiley.
- Angevine, C. E., Seashols-Williams, S. J., & Reiner, J. E. (2016). Infrared Laser Heating Applied to Nanopore Sensing for DNA Duplex Analysis. *Analytical Chemistry*, 88(5), 2645–2651.
- Aria, A. I., Kidambi, P. R., Weatherup, R. S., Xiao, L., Williams, J. A., & Hofmann, S. (2016). Time Evolution of the Wettability of Supported Graphene under Ambient Air Exposure. *The Journal of Physical Chemistry C*, 120, 2215–2224.
- Aryal, P., Sansom, M., & Tucker, S. J. (2015). Hydrophobic Gating in Ion Channels. *Journal of Molecular Biology*, 427, 121–130.
- Ashraf, A., Wu, Y., Wang, M. C., Yong, K., Sun, T., Jing, Y., & Haasch, R. T. (2016). Doping Induced tunable wettability and adhesion of graphene. *Nano Letters*, 16, 4708–4712.
- Banerjee, S., Shim, J., Rivera, J., Jin, X., Estrada, D., Solovyeva, V., . . . Bashir, R. (2013). Electrochemistry at the edge of a single graphene layer in a nanopore. *ACS Nano*, 7, 834–843.
- Banks, C., Davies, T. J., Wildgoose, G. G., & Compton, R. G. (2005). Electrocatalysis at Graphite and Carbon Nanotube Modified Electrodes: Edge-Plane Sites and Tube Ends are the Reactive Sites. *Chemical Communications*, 829–841.
- Beckstein, O., & Sansom, M. P. (2004). The influence of geometry, surface charcter, and flexibility on the permation of ions and water through biological pores. *Physical Biology*, 1, 42–52.
- Beckstein, O., & Sansom, M. S. (2003). Liquid–vapor oscillations of water in hydrophobic nanopores. *Proceedings of the National Academy of Sciences of the United States of America*, 100, 7063–7068.
- Beckstein, O., Biggin, P. C., & Sansom, M. S. (2001). A Hydrophobic Gating Mechanism for Nanopores. *Journal of Physical Chemistry B*, 105, 12902–12905.
- Beckstein, O., Tai, K., & Sansom, M. S. (2004). Not Ions Alone: Barriers to Ion Permeation in Nanopores and Channels. *Journal of the Americal Chemical Society*, 126(45), 14694–14695.
- Bertolazzi, S., Brivio, J., & Kis, A. (2011). Stretching and Breaking of Ultrathin MoS₂. *ACS Nano*, 5(12), 9703–9709.

- Bhadra, P., Sengupta, S., Ratchagar, N. P., Achar, B., Chadha, A., & Bhattacharya, E. (2016). Selective transportation of charged ZnO nanoparticles and microorganism dialysis through silicon nanoporous membranes. *Journal of Membrane Science*, *503*, 16–24.
- Blake, P., Hill, E. W., Castro Neto, A. H., Novoselov, K. S., Jiang, D., Yang, R., . . . Geim, A. K. (2007). Making Graphene Visible. *Applied Physics Letters*, *91*, 063124.
- Boldrin, L., F., S., Chowdhury, R., & Adhikari, S. (2011). Effective mechanical properties of hexagonal boron nitride nanosheets. *Nanotechnology*, *22*(50), 505702. doi: 10.1088/0957-4484/22/50/505702.
- Bonaccorso, F., Sun, Z., Hasan, T., & Ferrari, A. C. (2010). Graphene photonics and optoelectronics. *Nature Photonics*, *4*, 611–622.
- Bouleghlimat, E., Davies, P. R., Davies, R. J., Howarth, R., Kulhavy, J., & Morgan, D. J. (2013). The effect of acid treatment on the surface chemistry and topography of graphite. *Carbon*, *361*, 124–133.
- Bunch, J. S., Verbridge, S. S., Alden, J. S., van der Zande, A. M., Parpia, J. M., Craighead, H. G., & McEuan, P. L. (2008). Impermeable atomic membranes from graphene sheets. *Nano Letters*, *8*, 2458–2452.
- Cassabois, G., Valvin, P., & Gil, B. (2015). Hexagonal boron nitride is an indirect band gap semiconductor. *Nature Photonics*, *10*, 262–266.
- Castro Neto, A. H., Guinea, F., Peres, N. M., & Novoselov, K. S. (2009). The electronic properties of graphene. *Reviews of Modern Physics*, *81*, 109.
- Celebi, K., Buchhein, J., Wyss, R. M., Droudian, A., Gasser, P., Shorubalko, I., . . . Park, H. G. (2014). Ultimate Permeation Across Atomically Thin Porous Graphene. *Science*, *344*, 289–292.
- Chen, Y., Zou, J., Campbell, S. J., & Le Caer, G. (2004). Boron nitride nanotubes: pronounced resistance to oxidation. *Applied Physics Letters*, *84*, 2430–2432.
- Cheng, C., Jiang, G., Garvey, C. J., Wang, Y., Simon, G. P., Liu, J. Z., & Li, D. (2016). Ion transport in complex layered graphene-based membranes with tunable interlayer spacing. *Scientific Advances*. doi:11.1126/sciadv.1501272
- Chhowalla, M., Shin, H. S., Eda, G., Li, L.-J., Loh, K. P., & Zhang, H. (2013). The chemistry of two-dimensional layered transition metal dichalcogenide nanosheets. *Nature Chemistry*, *5*, 263–275.

- Chimerel, C., Movileanu, L., Pezeshki, S., Winterhalter, M., & Kleinekathofer, U. (2008). Transport at the nanoscale: temperature dependence of ion conductance. *European Biophysics Journal*, 38(121).
- Chung, H. H., Chan, C. K., Khire, T. S., Marsh, G. A., Clark Jr., A., Waugh, R. E., & McGrath, J. L. (2014). Highly permeable silicon membranes for shear free chemotaxis and rapid cell labeling. *Lab on a Chip*, 14, 2456–2468.
- Clarke, J., Wu, H.-C., Jayasinghe, L., Patel, A., Reid, S., & Bayley, H. (2009). Continuous base identification for single-molecule nanopore DNA sequencing. *Nature Nanotechnology*, 4, 265–270.
- Cohen-Tanugi, D., & Grossman, J. C. (2012). Water desalination across nanoporous graphene. *Nano Letters*, 12(7), 3602–3608.
- Coleman, V., Knut, R., Karis, O., Grennberg, H., Jansson, U., Quinlan, R., . . . Eriksson, O. (2008). Defect formation in graphene nanosheets by acid treatment: an x-ray absorption spectroscopy and density functional theory study. *Journal of Physics D: Applied Physics*, 41, 062001.
- Conley, H. J., Wang, B., Ziegler, J. I., Haglund, R. F., Pantelides, S. T., & Bolotin, K. I. (2013). Bandgap Engineering of Strained Monolayer and Bilayer MoS₂. *Nano Letters*, 13(8), 3626–3630. doi:10.1021/nl4014748
- Daiguji, H. (2010). Ion transport in nanofluidic channels. *Chemical Society Reviews*, 39, 901–911.
- Danda, G., Das, P. M., Chou, Y.-C., Mlack, J. T., Parkin, W. M., Naylor, C. H., . . . Drndic, M. (2017). Monolayer WS₂ Nanopores for DNA Translocation with Light-Adjustable Sizes. *ACS Nano*. doi:10.1021/acsnano.6b08028
- Davenport, M., Healy, K., Pevarnik, M., Teslich, N., Cabrini, S., Morrison, A. P., . . . Letant, S. E. (2012). The Role of Pore Geometry in Single Nanoparticle Detection. *ACS Nano*, 6(9), 8366–8380.
- Dean, C., Young, A. F., Meric, I., Lee, C., Wang, L., Sorgenfrei, S., . . . Hone, J. (2010). Boron nitride substrates for high-quality graphene electronics. *Nature Nanotechnology*, 5, 722–726.
- Debenedetti, P. G. (1996). *Metastable Liquids: Concepts and Principles*. Princeton: Princeton University Press.
- DeBois, R. W., & Bean, C. P. (1970). Counting and sizing submicron particles by the resistive pulse technique. *Review of Scientific Instruments*, 41(7), 909–916.

- Dekker, C. (2007). Solid-state nanopores. *Nature Nanotechnology*, 2(4), 209–215.
- Dhont, J. K. (1996). *An Introduction to Dynamics of Colloids*. Elsevier. doi:ISBN 0-08-053507-0
- Drahushuk, L. W., & Strano, M. S. (2012). Mechanisms of gas permeation through single layer graphene membranes. *Langmuir*, 28, 16671–16678.
- Dzubiella, J., Allen, R. J., & Hansen, J. P. (2004). Electric field-controlled water permeation coupled to ion transport through a nanopore. *Journal of Chemical Physics*, 120, 5001–5004.
- Emmrich, D., Beyer, A., Nadzeyka, A., Bauerdick, S., Meyer, J. C., Kotakoski, J., & Golzhauser, A. (2016). Nanopore fabrication and characterization by helium ion microscopy. *Applied Physics Letters*, 108, 163103.
- Expanding our 2D vision. (2016). *Nature Reviews. Materials*, 1(11). <http://www.nature.com/articles/natrevmats201689>
- Fan, R., Huh, S., Yan, R., Arnold, J., & Yang, P. (2008). Gated proton transport in aligned mesoporous silica films. *Nature*, 7, 303–307.
- Fan, R., Yue, M., Karnik, R., Majumdar, A., & Yang, P. (2005). Polarity switching and transient response in single nanotube nanofluidic transistors. *Physical Review Letters*, 95, 086607.
- Farimani, A. B., Min, K., & Aluru, N. R. (2014). DNA Base Detection Using a Single-Layer MoS₂. *ACS Nano*, 8, 7914–7922.
- Feng, J., Liu, K., Bulushev, R. D., Khlybov, S., Dumcenco, D., Kis, A., & Radenovic, A. (2015). Identification of single nucleotides in MoS₂ nanopores. *Nature Nanotechnology*, 10, 1070–1076.
- Feng, J., Liu, K., Graf, M., Dumcenco, D., Kis, A., Di Ventra, M., & Radenovic, A. (2016). Observation of ionic Coulomb blockade in nanopores. *Nature Materials*, 15, 850–855.
- Feng, J., Liu, K., Graf, M., Lihter, M., Bulushev, R. D., Dumcenco, D., . . . Feng, J. (2015). Electrochemical Reaction in Single Layer MoS₂: Nanopores Opened Atom by Atom. *Nano Letters*, 15(5), 3431–3438.
- Ferrari, A. C., Meyer, J. C., Scardaci, V., Casiraghi, C., Lazzeri, M., Mauri, F., . . . Geim, A. K. (2006). Raman Spectrum of Graphene and Graphene Layers. *Physical Review Letters*, 97, 187401.

- Fiori, N. D., Squires, A., Bar, D., Gilboa, T., Moustakas, T. D., & Meller, A. (2013). Optoelectronic control of surface charge and translocation dynamics in solid-state nanopores. *Nature Nanotechnology*, 8, 946–950.
- Fluinski, A., Kosinska, I., & A, S. (2005). Transport properties of nanopores in electrolyte solutions: the diffusional model and surface currents. *New Journal of Physics*, 7(132), 010132.
- Frank, I. W., Tanenbaum, D. M., van der Zande, A. M., & McEuen, P. L. (2007). Mechanical properties of suspended graphene sheets. *Journal of Vacuum Science and Technology*, 25, 2558–2561.
- Ganatra, R., & Zhang, Q. (2014). Few-Layer MoS₂: A Promising Layered Semiconductor. *ACS Nano*, 8(5), 4074–4099.
- Garaj, S., Hubbard, W., Reina, A., Kong, J., Branton, D., & Golovenchenko, J. (2010). Graphene as a subnanometre trans-electrode membrane. *Nature*, 467, 190–193.
- Garaj, S., Liu, S. L., Golovchenko, J. A., & Branton, D. (2012). Molecule-hugging Graphene Nanopores. *Proceedings of the National Academy of Sciences of the United States of America*, 110(30), 12192–12196.
- Geim, A. K., & Grigorieva, I. V. (2013). Van der Waals heterostructures. *Nature*, 499, 419–425.
- Geim, A. K., & Novoselov. (2007). The rise of graphene. *Nature Materials*, 6, 183–191.
- Gombosi, T. I. (1994). *Gaskinetic theory*. Cambridge University Press.
- Guan, W., Fan, R., & Reed, M. A. (2011). Field-effect reconfigurable nanofluidic ionic diodes. *Nature Communications*, 2, 506. doi:10.1038/ncomms1514
- Guan, W., Li, S. X., & Reed, M. A. (2014). Voltage gated ion and molecule transport in engineered nanochannels: theory, fabrication and applications. *Nanotechnology*, 25, 122001.
- Hall, J. E. (1975). Access resistance of a small circular pore. *The Journal of General Physiology*, 66, 531–532.
- He, K., Poole, C., Mak, K. F., & Shan, J. (2013). Experimental Demonstration of Continuous Electronic Structure Tuning via Strain in Atomically Thin MoS₂. *Nano Letters*, 13(6), 2931–2936. doi: 10.1021/nl4013166
- Hedberg, J. (n.d.). *Free Science Images*. Retrieved from James Hedberg Personal Website: www.jameshedberg.com/scienceGraphics.php

- Heerema, S. J., & Dekker, C. (2016). Graphene nanodevices for DNA sequencing. *Nature Nanotechnology*, *11*, 127–136.
- Hille, B. (2001). *Ion Channels of Excitable Membranes* (3rd ed.). Sutherland, MA: Sinauer.
- Hong, S., Constans, C., Martins, M. V., Seow, Y. C., Carrio, J. A., & Garaj, S. (2017). Scalable Graphene-based Membranes for Ionic Sieving with Ultrahigh Charge Selectivity. *Nano Letters*, *17*(2), 728–732. doi:10.1021/acs.nanolett.6b03837
- Hu, G., Mao, M., & Ghosal, S. (2012). Ion transport through a graphene nanopore. *Nanotechnology*, *23*(39).
- Hu, N., Ai, Y., & Qian, S. Q. (2012). Field effect control of electrokinetic transport in micro/nanofluidics. *Sensors and Actuators B: Chemical*, *161*(1), 1150–1167.
- Hu, S., Lozada-Hidalgo, M., F.Wang, F. C., Mishchenko, A., Schedin, F., Nair, R. R., . . . Geim, A. K. (2014). Proton Transport through one-atom-thick crystals. *Nature*, *516*, 227–230.
- Hummer, G., Rasaiah, J. C., & Noworyta, J. P. (2001). Water conduction through the hydrophobic channel of a carbon nanotube. *Nature*, *414*, 188–190.
- Hunter, R. J. (1989). *Foundations of colloid Science*. Oxford: Clarendon Press.
- Innes, L., Gutierrez, D., Mann, W., Buchsbaum, S. F., & Siwy, Z. S. (2015). Presence of electrolyte promotes wetting and hydrophobic gating in nanopores with residual surface charges. *Analyst*, *140*, 4804–4812.
- Ito, T., Sun, L., & Crooks, R. M. (2003). Electrochemical Etching of Individual Multiwall Carbon Nanotubes. *Electrochemical and Solid-State Letters*, *6*(1), C4–C7.
- Jain, T., Rasera, B. C., Guerrero, R. J., Boutilier, M. S., O'Hern, S. C., Idrobo, J.-C., & Karnik, R. (2015). Heterogeneous sub-continuum ionic transport in statistically isolated graphene nanopores. *Nature Nanotechnology*, *10*, 1053–1057.
- James, T., Kalinin, Y. V., Chan, C.-C., Randhawa, J. S., Gaevski, M., & Gracias, D. H. (2012). Voltage-gated ion transport through semiconducting conical nanopores formed by metal nanoparticle-assisted plasma etching. *Nano Letters*, *12*, 3437–3442.
- Jiang, D., Cooper, R., & Dai, S. (2009). Porous graphene as the ultimate membrane for gas separation. *Nano Letters*, *9*, 4019–4024.
- Jiang, J.-W. (2015). Graphene versus MoS₂: A Short Review. *Frontiers in Physics*, *10*. doi: 10.1007/s11467-015-0459-z

- Johnson, D. G., Khire, T. S., Lyubarskaya, Y. L., Smith, K. J., DesOrmeaux, J.-P. S., Taylor, J. G., . . . McGrath, J. L. (2015). Ultrathin Silicon Membranes for Wearable Dialysis. *Advances in Chronic Kidney Disease*, 20(6), 508–515.
- Jones, P. R., Hao, X., Cruz-Chu, E. R., Rykaczewski, K., Nandy, K., Schutzius, T. M., . . . Patankar, N. A. (2015). Sustaining dry surfaces under water. *Scientific Reports*, 5, 12311. doi:10.1038/srep12311
- Joshi, P., Smolyanitsky, A., Petrossian, L., Goryll, M., Saraniti, M., & Thornton, T. J. (2010). Field effect modulation of ionic conductance of cylindrical silicon-on-insulator nanopore array. *Journal of Applied Physics*, 107, 054701. doi:10.1063/1.3298468
- Karlsson, D., Zacchi, G., & Axelsson, A. (2002). Electronic Speckle Pattern Interferometry: A Tool for Determining Diffusion and Partition Coefficients for Proteins in Gels. *Biotechnology Progress*, 18(6), 1423–1430.
- Karnik, R., Castelino, K., & Majumdar, A. (2006). Field-effect control of protein transport in a nanofluidic transistor circuit. *Applied Physics Letters*, 88, 123114.
- Karnik, R., Duan, C., Castelino, K., Daiguji, H., & Majumdar, A. (2007). Rectification of ionic current in a nanofluidic diode. *Nano Letters*, 7(3), 547–551.
- Karnik, R., Fan, R., Yue, M., Li, D., Yang, P., & Majumdar, A. (2005). Electrostatic control of ions and molecules in nanofluidic transistors. *Nano Letters*, 5(5), 943–948.
- Kim, S., Feinberg, B., Kant, R., Chui, B., Goldman, K., Park, J., . . . Shuvo, R. (2016). Diffusive Silicon Nanopore Membranes for Hemodialysis Applications. *PLoS One*. doi:10.1371/journal.pone.0159526
- Koenig, S. P. (2013). *Graphene Membranes: Mechanics, Adhesion, and Gas Separations*. Doctoral dissertation, University of Colorado Boulder.
- Koenig, S. P., Boddeti, N. G., Dunn, M. L., & Bunch, J. S. (2011). Ultrastrong Adhesion of Graphene Membranes. *Nature Nanotechnology*, 6, 543–546.
- Koenig, S. P., Wang, L., Pellegrino, J., & Bunch, J. S. (2012). Selective molecular sieving through porous graphene. *Nature Nanotechnology*, 7, 728–732.
- Kosinska, I. D. (2006). How the asymmetry of internal potential influences the shape of I-V characteristic of nanochannels. *The Journal of Chemical Physics*, 124, 244707.
- Kostarelos, K. (2016). Translating graphene and 2D materials into medicine. *Nature Reviews. Materials*, 1(11). doi:10.1038/natrevmats.2016.84

- Kowalczyk, S. W., Grosberg, A. Y., Rabin, Y., & Dekker, C. (2011). Modeling the conductance and DNA blockade of solid-state nanopores. *Nanotechnology*, *22*, 315101.
- Kozbial, A., Li, Z., Conway, C., McGinley, R., Dhingra, S., Vahdat, V., . . . Li, L. (2014). Study on the surface energy of graphene by contact angle measurements. *Langmuir*, *30*, 8598–8606.
- Kuan, A. T., Lu, B., Xie, P. S., & Golovchenko, J. A. (2015). Electric pulse fabrication of graphene nanopores in electrolyte solution. *Applied Physics Letters*, *106*, 203109. doi:10.1063/1.4921620
- Kuiper, S., van Rijn, C. J., Nijdam, W., & Elwenspoek, M. C. (1998). Development and applications of very high flux microfiltration membranes. *Journal of Membrane Science*, *150*, 1–8.
- Kuyucak, S., Andersen, O. S., & Chung, S.-H. (2001). Models of permeation in ion channels. *Reports on Progress in Physics*, *64*, 1427–1472.
- Kwok, H., Briggs, K., & Tabard-Cossa, V. (2014). Nanopore fabrication by controlled dielectric breakdown. *PLoS One*. doi:10.1371/journal.pone.0092880
- Lee, C., Wei, X., Kysar, J. W., & Hone, J. (2008). Measurement of the elastic properties and intrinsic strength of monolayer graphene. *Science*, *321*, 385–388.
- Lee, S.-H., Lee, H., Jin, T., Park, S., Yoon, B. J., Sung, G. Y., . . . Kim, S. J. (2015). Sub-10 nm transparent all-around-gated ambipolar ionic field effect transistor. *Nanoscale*, *7*, 936–946.
- Leung, K., Luzar, A., & Bratko, D. (2003). Dynamics of Capillary Drying in Water. *Physical Review Letters*, *90*, 065502.
- Li, J., Stein, D., McMullan, C., Branton, D., Aziz, M. J., & Golovchenko, J. A. (2001). Ion-beam sculpting at nanometre length scales. *Nature*, *412*, 166–169.
- Li, W., Tan, C., Lowe, M. A., Abruna, H. D., & Ralph, D. C. (2011). Electrochemistry of Individual Monolayer Graphene Sheets. *ACS Nano*, *5*(3), 2264–2270.
- Li, W., Yang, Y., Weber, J. K., Zhang, G., & Zhou, R. (2016). Tunable, Strain-Controlled Nanoporous MoS₂ Filter for Water Desalination. *ACS Nano*, *10*(2), 1829–1835.
- Li, Z., Wang, Y., Kozbial, A., Shenoy, G., Zhou, F., McGinley, R., . . . Liu, H. (2013). Effect of airborne contaminants on the wettability of supported graphene and graphite. *Nature Materials*, *12*, 925–931.

- Lipp, A., Schwetz, K. A., & Honold, K. (1989). Hexagonal boron nitride: fabrication, properties and application. *Journal of European Ceramics Society*, 5, 3–9.
- Liu, K., Feng, J., Kis, A., & Radenovic, A. (2014). Atomically Thin Molybdenum Disulfide Nanopores with High Sensitivity for DNA Translocation. *ACS Nano*, 8, 2504–2511.
- Liu, L., Ryu, S., Tomasik, M. R., Stolyarova, E., Jung, N., Hybertsen, M. S., . . . Flynn, G. W. (2008). Graphene oxidation: thickness-dependant etching and strong chemical doping. *Nano Letters*, 8, 1965–1970.
- Lloyd, D., Liu, X., Christopher, J. W., Cantley, L., Wadehra, A. K., Goldberg, B. B., . . . Bunch, J. S. (2016). Band Gap Engineering with Ultralarge Biaxial Strains in Suspended Monolayer MoS₂. *Nano Letters*, 16(9), 5836–5841. doi:10.1021/acs.nanolett.6b02615
- Lopez-Sanchez, O., Lembke, D., Kayci, M., Radenovic, A., & Kis, A. (2013). Ultrasensitive photodetectors based on monolayer MoS₂. *Nature Nanotechnology*, 8(7), 497–501.
- Lozanda-Hidalgo, M., Hu, S., Marshall, O., Mishchenko, A., Grigorenko, A. N., Dryfe, R. A., . . . Geim, A. K. (2016). Sieving hydrogen isotopes through two-dimensional crystals. *Science*, 351, 68–70.
- Lukowski, M. A., Daniel, A. S., Meng, F., Forticaux, A., Li, L., & Jin, S. (2013). Enhanced Hydrogen Evolution Catalysis from Chemically Exfoliated Metallic MoS₂ Nanosheets. *Journal of the American Chemical Society*, 135(28), 10274–10277.
- Luzar, A. (2004). Activation Barrier Scaling for the Spontaneous Evaporation of Confined Water. *Journal of Physical Chemistry B*, 108, 19859–19866.
- MacKinnon, R. (2004). Potassium channels and the atomic basis of selective ion conduction (Nobel Lecture). *Angewandte Chemie International Edition*, 43, 4265–4277.
- Mahajan, R., & Koros, W. J. (2002). Mixed matrix membrane materials with glassy polymers, Part 1. *Polymer Engineering & Science*, 42(7), 1432–1441.
- Marban, E. (2002) Cardiac channelopathies. *Nature*, 415, 213–218.
- Merchant, C. A., Healy, K., Wanunu, M., Ray, V., Peterman, N., Bartel, J., . . . Drndic, M. (2010). DNA Translocation through Graphene Nanopores. *Nano Letters*, 10, 2915–2921.

- Miles, B. N., Ivanov, A. P., Wilson, K. A., Dogan, F., Japrun, D., & Edel, J. B. (2013). Single molecule sensing with solid-state nanopores: novel materials, methods, and applications. *Chemical Society Reviews*, *42*, 15–28. doi:10.1039/C2cs35286a
- Nagel, G., Szellas, T., Huhn, W., Kateriya, S., Aseishyili, N., Ollig, D., . . . Bamberg, E. (2003). Channelrhodopsin-2, a directly light-gated cation-selective membrane channel. *Proceedings of the National Academy of Sciences of the United States of America*, *100*(24), 13940–13945.
- Nair, R. R., Wu, H. A., Grigorieva, I. V., & Geim, A. K. (2012). Unimpeded permeation of water through helium-leak-tight graphene-based membranes. *Science*, *335*, 442–444.
- Nam, S.-W., Rooks, M. J., Kim, K.-B., & Rossnagel, S. M. (2009). Ionic Field Effect Transistors with Sub-10 nm Multiple Nanopores. *Nano Letters*, *9*(5), 2044–2048.
- Nosov, K. S., Geim, A. K., Morozov, S. V., Jiang, D., Katsnelson, M. I., Grigorieva, I. V., . . . Firsov, A. A. (2005). Two-dimensional gas of massless Dirac fermions in graphene. *Nature*, *438*, 197–200.
- Nosov, K. S., Jiang, D., F., S., Booth, T. J., Khotkevich, V. V., Morozov, S. V., & Geim, A. K. (2005). Two-dimensional Atomic Crystals. *Proceedings of the National Academy of Sciences of the United States of America*, *102*(30), 10451–10453.
- Nosov, K. S., Mishchenko, A., Carvalho, A., & Castro Neto, A. H. (2016). 2D Materials and Van der Waal Heterostructures. *Science*, *353*(6298), aac9439.
- O'Hern, S. C., Boutilier, M. S., Idrobo, J.-C., Song, Y., Kong, J., Laoui, T., . . . Karnik, R. (2014). Selective Ionic Transport through Tunable Subnanometer Pores in Single-Layer Graphene Membranes. *Nano Letters*, *14*, 1234–1241.
- O'Hern, S. C., Jiang, D., Bose, S., Idrobo, J.-C., Song, Y., Laoui, T., . . . Karnik, R. (2015). Nanofiltration across Defect-sealed Nanoporous Monolayer Graphene. *Nano Letters*, *15*(5), 3254–3260.
- Ondarcuhu, T., Thomas, V., Nunez, M., Dujardin, E., Rahman, A., Black, C. T., & Checco, Antonio. Wettability of partially suspended graphene. *Scientific Reports*, *6*, 24237.
- Ostrowski, J. H., & Eaves, J. D. (2014). The Tuneable Hydrophobic Effect on Electrically Doped Graphene. *Journal of Physical Chemistry B*, *118*(2), 530–536.
- Ouyang, T., Chen, Y., Xie, Y., Yang, K., & Bao, Z. (2010). Thermal transport in hexagonal boron. *Nanotechnology*, *21*(24).

- Paik, K.-H. P., Liu, Y., Tabard-Cossa, V., Waugh, M. J., Huber, D. E., Provine, J., . . . Davis, R. W. (2012). Control of DNA Capture by Nanofluidic Transistors. *ACS Nano*, 6(8), 6767–6775.
- Pallas, N. R., & Harrison, Y. (1990). *Colloids and Surfaces*, 43, 169–194.
- Pandey, P., & Chuanhan, R. S. (2001). Membranes for gas separation. *Progress in Polymer Science*, 26(6), 853–893.
- Park, J. Y., Yaish, Y., Brink, M., Rosenblatt, S., & McEuen, P. L. (2002). Electrical cutting and nicking of carbon nanotubes using an atomic force microscope. *Applied Physics Letters*, 80, 4446–4448.
- Park, S. (2016). The puzzle of graphene commercialization. *Nature Reviews. Materials*, 1(11). doi:10.1038/natrevmats.2016.85
- Powell, M. R., Cleary, L., Davenport, M., Shea, K. J., & Siwy, Z. S. (2011). Electric-field-induced wetting and dewetting in single hydrophobic nanopores. *Nature Nanotechnology*, 6, 798–802.
- Puddy, R. K., Scard, P., Tyndall, D., Connolly, M. R., Smith, C. G., Jones, G. A., . . . Buitelaar, M. R. (2011). Atomic force microscope nanolithography of graphene: cuts, pseudocuts, and tip current measurements. *Applied Physics Letters*, 98, 133120.
- Radenovic, A., Trepagnier, E., Csencsits, R., Downing, K. H., & Liphardt, J. (2008). Fabrication of 10 nm diameter hydrocarbon nanopores. *Applied Physics Letters*, 93, 183101.
- Rollings, R. C., Kuan, A. T., & Golovchenko, J. A. (2016). Ion selectivity of graphene nanopores. *Nature Communications*, 7, 11408. doi:10.1038/ncomms11408
- Schneider, G. F., Kowalczyk, S. W., Calado, V. E., Pandraud, G., Zandbergen, H. W., Vandersypen, L. M., & Dekker, C. (2010). DNA Translocation through Graphene Nanopores. *Nano Letters*, 10, 3163–3167.
- Schneider, G. F., Xu, Q., Hage, S., Luik, S., Spoor, J. N., Malladi, S., . . . Dekker, C. (2013). Tailoring the hydrophobicity of graphene for its use as nanopores for DNA translocations. *Nature Communications*, 4. doi:10.1038/ncomms3619
- Shan, Y., Tiwari, P., Krishnakumar, P., Vlassioux, I., Li, W. Z., Wang, X. W., & Darici, Y. (2013). Surface modification of graphene nanopores for protein translocation. *Nanotechnology*, 24(49), 495102.

- Shaw, D. J. (1980). *Introduction to Colloid and Surface Chemistry* (3rd ed.). Butterworth & Co.
- Shi, Y., Hamsen, C., Jia, X., Kim, K. K., & Reina, A. (2010). Synthesis of Few-Layer Hexagonal Boron Nitride Thin Film by Chemical Vapor Deposition. *Nano Letters*, *10*, 4134–4139.
- Sint, K., Wang, B., & Kral, P. (2008). Selective Ion Passage through Functionalized Graphene Nanopores. *Journal of the American Chemical Society*, *130*(49), 16448–16449.
- Siwy, Z. S. (2006). Ion-Current Rectification in Nanopores and Nanotubes with Broken Symmetry. *Advanced Functional Materials*, *16*, 735–746.
- Siwy, Z. S., & Howorka, S. (2010). Engineered voltage-responsive nanopores. *Chemical Society Reviews*, *39*, 1115–1132.
- Siwy, Z. S., Powell, M. R., Petrov, A., Kalman, E., Trautmann, C., & Eisenberg, R. S. (2006). Calcium-Induced Voltage Gating in Single Conical Nanopores. *Nano Letters*, *6*(8), 1729–1734.
- Smeets, R. M., Keyser, U. F., Krapf, D., Wu, M.-Y., Dekker, N. H., & Dekker, C. (2006). Salt Dependence of Ion Transport and DNA Translocation through Solid-State Nanopores. *Nano Letters*, *6*(1), 89–95.
- Smeets, R. M., Keyser, U. F., Wu, M. Y., Dekker, N. H., & C., D. (2006). Nanobubbles in solid-state nanopores. *Physical Review Letters*, *97*, 088101.
- Smirnov, S. N., Vlasiouk, I. V., & Larvik, N. V. (2011). Voltage-Gated Hydrophobic Nanopores. *ACS Nano*, *5*(9), 7453–7461.
- Smirnov, S., Vlasiouk, I., Takmakov, P., & Rios, F. (2010). Water Confinement in Hydrophobic Nanopores. Pressure-Induced Wetting and Drying. *ACS Nano*, *4*(9), 5069–5075.
- Song, C., & Correy, B. (2009). Intrinsic ion selectivity of narrow hydrophobic pores. *Journal of Physical Chemistry B*, *113*, 7642–7649.
- Song, L., Ci, L., Lu, H., Sorokin, P. B., Jin, C., Ni, J., . . . Ajayan, P. M. (2010). Large scale growth and characterization of atomic hexagonal boron nitride layers. *Nano Letters*, *10*, 3209–3215.
- Storm, A. J., Chen, J. H., Ling, X. S., Zandbergen, H. W., & Dekker, C. (2003). Fabrication of solid-state nanopores with single-nanometre precision. *Nature Materials*, *2*, 537–540.

- Streimer, C. C., Gaborski, T. R., McGrath, J. L., & Fauchet, P. M. (2007). Charge- and size-based separation of macromolecules using ultrathin silicon membranes. *Nature*, *445*, 749–753.
- Subbaiah, Y. P., Saji, K. J., & Tiwari, A. (2016). Atomically Thin MoS₂: A Versatile Nongraphene 2D Material. *Advanced Functional Materials*, *13*, 2046–2069.
- Suk, M. E., & Aluru, N. R. (2010). Water transport through ultrathin graphene. *Journal of Physical Chemistry Letters*, *10*(1), 1590–1594.
- Suk, M. E., & Aluru, N. R. (2014). Ion transport in sub-5nm graphene nanopores. *Journal of Chemical Physics*, *140*(8).
- Sun, C., Boutilier, M. S., Au, H., Poesio, P., Bai, B., Karnik, & Hadjiconstantinou, N. G. (2014). Mechanisms of molecular permeation through nanoporous. *Langmuir*, *30*(2), 675–682.
- Surwade, S. P., Smirnov, S. N., Vlassiuk, I. V., Unocic, R. R., Veith, G. M., Dai, S., & Mahurin, S. M. (2015). Water desalination using nanoporous single-layer graphene. *Nature Nanotechnology*, *10*, 459–464.
- Tamime, A. Y. (2013). *Membrane Processing: Dairy and Beverage Applications*. Chichester: Wiley.
- Tong, H. D., Jansen, H. V., Gadgil, V. J., Bostan, C. G., Berenschot, E., van Rijn, C. J., & Elwenspoek, M. (2004). Silicon nitride nanosieve membrane. *Nano Letters*, *4*, 283–287.
- Traversi, F., Raillon, C., Benameur, S. M., Liu, K., Khlybov, S., Tosun, M., . . . Radenovic, A. (2013). Detecting the translocation of DNA through a nanopore using graphene nanoribbons. *Nature Nanotechnology*, *8*, 939–945.
- Trick, J. L., Song, C., Wallace, E. J., & Sansom, M. S. (2017). Voltage gating of a biomimetic nanopore: electrowetting of a hydrophobic barrier. *ACS Nano*, Accepted for Publication.
- Trick, J. L., Wallace, E. J., Bayley, H., & Sansom, M. S. (2014). Designing a hydrophobic barrier within biomimetic nanopores. *ACS Nano*, *8*(11), 11268–11279.
- Tsutsui, M., Hongo, S., He, Y., Taniguchi, M., Gemma, N., & Kawai, T. (2012). Single-Nanoparticle Detection Using a Low-Aspect-Ratio Pore. *ACS Nano*, *6*(4), 3499–3505.

- Valota, A. T., Kinloch, I. A., Novoselov, K. S., Casiraghi, C., Eckmann, A., Hill, E. W., & Dryfe, R. A. (2011). Electrochemical Behavior of Monolayer and Bilayer Graphene. *ACS Nano*, 5(11), 8809–8815.
- Vanzo, D., Bratko, D., & Luzar, A. (2014). Dynamic Control of Nanopore Wetting in Water and Saline Solutions under an Electric Field. *Journal of Physically Chemistry B*, 8(119), 8890–8899.
- Venkatesan, B. M., & Bashir, R. (2011). Nanopore sensors for nucleic acid analysis. *Nature Nanotechnology*, 6, 615–624.
- Venkatesan, B. M., Estrada, D., Banerjee, S., Jin, X., Dorgan, V. E., Bae, M.-H., . . . Bashir, R. (2012). Stacked graphene-Al₂O₃ nanopore sensors for sensitive detection of DNA and DNA-protein complexes. *ACS Nano*, 6, 441–450.
- Vlassioun, I., Apel, P. Y., Dmitriev, S. N., Healy, K., & Siwy, Z. S. (2009). Versatile ultrathin nanoporous silicon nitride membranes. *Proceedings of the National Academy of Sciences of the United States of America*, 106(50), 21039–21044.
- Vlassioun, I., Smirnov, S., & Siwy, Z. (2008). Ionic selectivity of single nanochannels. *Nano Letters*, 8(7), 1978–1985.
- Vodyanoy, I. Bezrukov, S. M. (1992). Sizing of an ion pore by access resistance measurements. *Biophysical Journal*, 62(1), 10–11.
- Walker, M. I., Ubych, K., Saraswat, V., Chalklen, E. A., Braeuinger-Weimer, P., Caneva, S., . . . Keyser, U. F. (2017). Extrinsic Cation Selectivity of 2D Membranes. *ACS Nano*, Accepted for Publication. doi:10.1021/acsnano.6b06034
- Wang, L., Drahushuk, L. W., Cantley, L., Koenig, S. P., Liu, X., Pellegrino, J., . . . Bunch, J. S. (2015). Molecular valves for controlling gas phase transport made from discrete angstrom-sized pores in graphene. *Nature Nanotechnology*, 10, 785–790.
- Wang, L., Travis, J. J., Cavanagh, A. S., Liu, X., Koenig, S. P., Huang, P. Y., . . . Bunch, J. S. (2012). Ultrathin Oxide Films by Atomic Layer Deposition on Graphene. *Nano Letters*, 12, 3706–3710.
- Wang, Q. H., Kalantar-Zadeh, K., Kis, A., Coleman, J. N., & Strano, M. S. (2012). Electronics and optoelectronics of two-dimensional transition metal dichalcogenides. *Nature Nanotechnology*, 7, 699–712.
- Xiao, K., Wen, L., & Jiang, L. (2016). Biomimetic Solid-State Nanochannels: From Fundamental Research to Practical Applications. *Small*, 12(21), 2810–2831.

- Xiao, K., Zhou, Y., Kong, X.-Y., Xie, G., Li, P., Zhang, Z., . . . Jiang, L. (2016). Electrostatic-Charge- and Electric-Field-Induced Smart Gating for Water Transportation. *ACS Nano*, *10*(10), 9703–9079. doi: 10.1021/acsnano.6b05682
- Yamada, Y., Murota, K., Fujita, R., Kim, J., Watanabe, A., Nakamura, M., . . . Zettl, A. (2014). Vacancy defects introduced on graphene by oxygen gas. *Journal of the American Chemical Society*, *136*(6), 2232–2235.
- Yanagi, I., Akahori, R., Hatano, T., & Takeda, K.-i. (2014). Fabricating nanopores with diameters of sub-1nm to 3 nm using multilevel voltage injection. *Scientific Reports*, *4*. doi:10.1038/srep05000
- Yang, J., Ferranti, D. C., Stern, L. A., Sanford, C. A., Huang, J., Ren, Z., . . . Hall, A. R. (2011). Rapid and precise scanning helium ion microscope milling of solid-state nanopores for biomolecule detection. *Nanotechnology*, *22*(28).
- Ying-Hua, Q., Kun, L., Wei-Yu, C., Wei, S., Qi-Yan, T., & Yun-Fei, C. (2015). Ion and water transport in charge-modified graphene nanopores. *Chinese Physics B*, *24*(10), 108201.
- Yuan, W., Zhou, Y., Li, Y., Li, C., Peng, H., Zhang, J., . . . Shi, G. (2013). The edge- and basal-plane-specific electrochemistry of a single-layer graphene sheet. *Scientific Reports*, *3*. doi:10.1038/srep02248
- Zhang, Y., Tan, Y.-W., Stormer, H. L., & Kim, P. (2010). Experimental observation of the quantum Hall effect and Berry's phase in graphene. *Nature*, *438*, 201–204.
- Zhou, Z., Hu, Y., Wang, H., Xu, Z., Wang, W., Bai, X., . . . Lu, X. (2013). DNA translocation through hydrophilic nanopore in hexagonal boron nitride. *Scientific Reports*, *3*. doi:10.1038/srep03287

CURRICULUM VITAE

Lauren Elizabeth Young Cantley
Department of Mechanical Engineering, Boston University
110 Cummington Mall, Boston, MA 02215. *Email:* lcantley@bu.edu

EDUCATION

Boston University, College of Engineering

Ph.D., Mechanical Engineering

Advisor: Dr. J. Scott Bunch

Dissertation: Biomimetic Nanopores from Atomically Thin Membranes

University of Colorado at Boulder, College of Engineering

M.S., Mechanical Engineering (GPA: 3.6/4.0)

Advisor: Dr. J. Scott Bunch

Focus track: Microsystems

Grinnell College

B.A., Physics (GPA: 3.8/4.0)

Dean's List: Fall 2007, Spring 2008, Fall 2008, Spring 2010, Fall 2010

AWARDS, FELLOWSHIPS & HONORS

National Science Foundation Graduate Research Fellowship, 2012–2015

NIST MSE Fellowship Awardee, 2012

Outstanding Mechanical Engineering Research Potential Fellowship, *University of Colorado at Boulder*, 2011

iMINT Best One-Slide Presentation, March Meeting, 2012

RESEARCH & TEACHING EXPERIENCE

Graduate Research Assistant, Boston University, 2013–2017

Atomic Membrane Laboratory

Advisor: Dr. J. Scott Bunch

Graduate Research Assistant, University of Colorado at Boulder, 2011–2013

Atomic Membrane Laboratory

Advisor: Dr. J. Scott Bunch

Graduate Teaching Assistant, University of Colorado at Boulder, 2011–2013
Statics and Structures (MCEN 2023)
Mechanics of Solids (MCEN 2063)

Undergraduate Research Assistant, Kalvi Institute of NanoScience at TU Delft, 2011
 National Nanotechnology Infrastructure Network iREU program
Advisor: Prof. dr. ir. Lieven Vandersypen

Undergraduate Research Assistant, University of Minnesota, 2010–2011
 Kortshagen Group
Advisor: Dr. Uwe Kortshagen

Undergraduate Research Assistant, University of Colorado at Boulder, 2010
 National Nanotechnology Infrastructure Network REU program
Advisor: Dr. J. Scott Bunch

Undergraduate Research Assistant, Case Western Reserve University, 2009
 Physics REU program
Advisor: Dr. Kathleen Kash

JOURNAL PUBLICATIONS

L. Cantley, J.L. Swett, D. A. Cullen, P. V. Bedworth, S. Heise, S. Stinton, J.S. Bunch. *Solid-state voltage gated K^+/Na^+ selective ion channels from porous graphene*. Under review (2016).

D. Lloyd, X. Liu, J. Christopher, **L. Cantley**, A. Wadehra, B. Kim, A.K. Swan, B.B. Goldberg, J.S. Bunch. *Band Gap Engineering with Ultra-large Biaxial Strains in Suspended Monolayer MoS_2* . *Nano Letters*, **16** (9), 5836–5841 (2016).

L. Wang, L.W. Drahushuk, **L. Cantley**, S.P. Koenig, X. Liu, J. Pellegrino, M.S. Strano, J.S. Bunch. *Molecular valves for controlling gas phase transport made from discrete angstrom-sized pores in graphene*. *Nature Nanotechnology*, **10**, 785–790 (2015).

X. Liu, J. W. Suk, N.G. Boddeti, **L. Cantley**, L. Wang, J. M. Gray, H. J. Hall, V. M. Bright, C. T. Rogers, M.L. Dunn, R. S. Ruoff and J. S. Bunch (2013), *Large Arrays and Properties of 3-Terminal Graphene Nanoelectromechanical Switches*. *Advanced Materials*, **26**, 1571–1576 (2014).

L. Cantley. *Control and Dynamics of Bubbles observed in Graphene Films*; 2011 NNIN REU Research Accomplishments, p98, November 2011,
http://www.nnin.org/nnin_2011reu.html

L. Cantley. *Fabrication of a Three Terminal Nanomechanical Graphene Switch*; 2010 NNIN REU Research Accomplishments, p118, November 2010, http://www.nnin.org/nnin_2010reu.html

CONFERENCE PRESENTATIONS

L. Cantley, S. Bunch. (2015, March). *Ionic transport across atomically-thin graphene membranes*. Presented at American Physical Society March Meeting 2015. San Antonio, TX.

L. Cantley, I. Haghighi, I. Herd, N. Rodriguez, S. Bunch (2015, March). *Ionic transport across porous graphene membranes*. Poster presented at Spring 2015 Meeting of the APS New England Section. Boston, MA.